Arnold Schwarzenegger
Governor

COOL-COLOR ROOFING MATERIAL ATTACHMENT 1: TASK 2.4.1 REPORTS – IDENTIFY AND CHARACTERIZE PIGMENTS WITH HIGH SOLAR REFLECTANCE

PIER FINAL PROJECT REPORT

Prepared For:
California Energy Commission
Public Interest Energy Research Program

Prepared By:
Lawrence Berkeley National Laboratory and Oak Ridge National Laboratory

ERNEST ORLANDO LAWRENCE
BERKELEY NATIONAL LABORATORY

June 2006
CEC-500-2006-067-AT1

Prepared By:
Lawrence Berkeley National Laboratory
Hashem Akbari
City, State
Contract No. 500-01-021
Work Authorization (if applicable)

Oak Ridge National Laboratory
William Miller
Oak Ridge, Tennessee

Prepared For:

California Energy Commission

Public Interest Energy Research (PIER) Program

Chris Scruton
Contract Manager

Ann Peterson
Building End-Use Energy Efficiency Program Team Leader

Nancy Jenkins
PIER Energy Efficiency Research Office Manager

Martha Krebs, Ph. D.
Deputy Director
ENERGY RESEARCH AND DEVELOPMENT DIVISION

B.B. Blevins
Executive Director

Available online at www.sciencedirect.com
SCIENCE DIRECT®
Solar Energy Materials & Solar Cells
ELSEVIER
Solar Energy Materials & Solar Cells 89 (2005) 319–349
www.elsevier.com/locate/solmat

Solar spectral optical properties of pigments—Part I: model for deriving scattering and absorption coefficients from transmittance and reflectance measurements

Ronnen Levinson*, Paul Berdahl, Hashem Akbari

Lawrence Berkeley National Laboratory, 1 Cyclotron Road, Berkeley, CA 94720, USA

Received 15 June 2004; received in revised form 5 November 2004; accepted 12 November 2004
Available online 24 February 2005

Abstract

The suitability of a pigment for inclusion in "cool" colored coatings with high solar reflectance can be determined from its solar spectral backscattering and absorption coefficients. Pigment characterization is performed by dispersing the pigment into a transparent film, then measuring spectral transmittance and reflectance. Measurements of the reflectance of film samples on black and white substrates are also used. A model for extracting the spectral backscattering coefficient S and absorption coefficient K from spectrometer measurements is presented. Interface reflectances complicate the model. The film's diffuse reflectance and transmittance measurements are used to determine S and K as functions of a wavelength-independent model parameter σ that represents the ratio of forward to total scattering. σ is used to estimate the rate at which incident collimated light becomes diffuse, and is determined by fitting the measured film reflectance backed by black. A typical value is $\sigma = 0.8$. Then, the measured film reflectance backed by white is compared with a

*Corresponding author. Tel.: +1 510 486 7494; fax: +1 425 955 1992.
E-mail addresses: RMLevinson@LBL.gov (R. Levinson), PHBerdahl@LBL.gov (P. Berdahl), H_Akbari@LBL.gov (H. Akbari).

0927-0248/$ - see front matter Published by Elsevier B.V.
doi:10.1016/j.solmat.2004.11.012

Nomenclature

English symbols

a	defined as $(S+K)/S$
b	defined as $(a^2-1)^{1/2}$
f	film
g	background
i	intensity of total downflux
i_c	intensity of collimated downflux (incident direction is downward)
i_d	intensity of diffuse downflux
j	intensity of total upflux
j_c	intensity of collimated upflux
j_d	intensity of diffuse upflux
K	absorption coefficient
m	relative refractive index or wavelength index
M	total number of wavelengths
n	refractive index
N	observed near-infrared reflectance
q	fraction of total flux that is diffuse
R	reflectance
$\tilde{R}_c$	observed reflectance of collimated light
R_f	CRI (continuous refractive index) reflectance of film (absent interface reflectances)
$\tilde{R}_f$	observed reflectance of film
$R_{f,\ell}$	CRI reflectance of film with background ℓ
$\tilde{R}_{f,\ell}$	observed reflectance of film with background ℓ = b (black), w (white), or v (void)
R_g	CRI reflectance of background
$\tilde{R}_g$	observed reflectance of background
$R_{g,\ell}$	CRI reflectance of background ℓ
$\tilde{R}_{g,\ell}$	observed reflectance of background ℓ
R^i	reflectance to downflux
R^j	reflectance to upflux
R_u	CRI reflectance of opaque undercoat
$\tilde{R}_u$	observed reflectance of opaque undercoat
$R^\star$	intermediate value used in computation of reflectance of complex backgrounds
S	backscattering coefficient (scattering into opposite hemisphere)
T	internal transmittance
$\tilde{T}$	observed transmittance
T^i	downflux transmittance
T^j	upflux transmittance
$\tilde{T}_c$	observed collimated flux transmittance
z	distance from bottom of film

Greek symbols

α, β, γ	components of multi-layer system
δ	film thickness
Δ	error in intensity gradient or reflectance
ε	global error in predicted reflectance
η	average pathlength parameter
λ	wavelength (in vacuum)
μ	maximum absolute error in predicted reflectance
ρ	density
σ	forward scattering ratio (fraction of scattered light directed into forward hemisphere)
τ	internal film transmittance
τ_c	internal film collimated transmittance
χ	root-mean-square error in predicted reflectance
ω	reflectance at interface of media with different refractive indices
ω^i	reflectance of interface to downflux
ω^j	reflectance of interface to upflux
ω_c^i	reflectance of interface to collimated downflux
ω_c^j	reflectance of interface to collimated upflux

computed value as a self-consistency check. Measurements on several common pigments are used to illustrate the method.
Published by Elsevier B.V.

Keywords: Pigment characterization; Solar spectral optical properties; Kubelka-Munk theory; Refractive-index discontinuity; Cool roofs

1. Introduction

Nonwhite pigments with high near-infrared (NIR) reflectance historically have been used to camouflage military surfaces (by mimicking foliage) and to minimize solar heating of dark exterior architectural surfaces, such as colored vinyl siding and gray battleship hulls [1–3]. In recent years roofing manufacturers have incorporated NIR-reflecting pigments in coatings applied to a variety of nonwhite roofing products, such as metal panels and clay tiles [4–9]. The work we present here develops and validates a model for computation of solar spectral absorption and backscattering coefficients (current article), which is then applied to wide variety of pigments that may be used in architectural coatings (companion article, [10]).

Visible light (400–700 nm) accounts for only 43% of the energy in the air-mass 1.5 global solar irradiance spectrum (300–2500 nm) typical of North-American insolation [11]; the remainder arrives as near-infrared (700–2500 nm, 52%) or ultraviolet (300–400 nm, 5%) radiation (Fig. 1). Hence, replacing NIR-absorbing (“conventional”) roofing with visually similar, NIR–reflecting (“cool”) roofing can significantly reduce building heat gain. A recent study found that increasing the solar

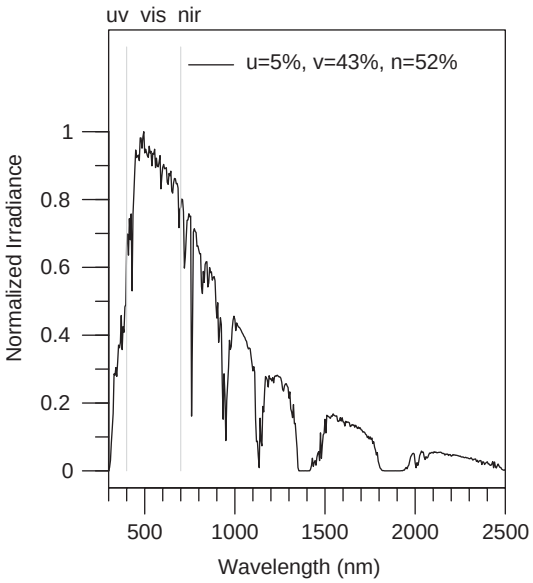

Fig. 1. Air mass 1.5 hemispherical solar spectral irradiance typical of North American insolation (5% ultraviolet, 43% visible, 52% near-infrared) [11].

reflectance of the roof of a prototypical California nonresidential building from 0.20 (conventional medium gray) to 0.55 (soiled white) yields statewide average annual source energy savings per unit roof area of 30 MJ/m^2; peak power demand savings of 2.1 W/m^2; and cost savings (15-year net present value of energy, plus savings achieved by downsizing cooling equipment) of \$6/m^2 [12,13]. A *cool* medium-gray roof with an initial near-infrared reflectance of 0.80 might have a weathered solar reflectance of about 0.42 [12,14]. Since energy, power, and cost savings are approximately proportional to change in weathered solar reflectance [15], using this cool medium-gray roof (weathered solar reflectance 0.42) in place of a standard medium gray roof (weathered solar reflectance 0.20) would yield about 60% of the white-roof savings, or 18 MJ/m^2 source energy, 1.3 W/m^2 peak power, and \$3.5/m^2 energy and equipment cost. Installing such cool colored roofing on nonresidential new construction in California could yield annual statewide savings of 84 TJ source energy, 5.5 MW peak power, and \$17 M energy and equipment cost.

A cool coating must have low visible transmittance to hide its background and low NIR absorptance to minimize NIR heat gain. Cool films may be subclassified as either "NIR-reflecting" or "NIR-transmitting." An NIR-reflecting film is always cool, while an NIR-transmitting film requires an NIR-reflecting background (e.g., a shiny metal or a white coating) to form a colored NIR-reflecting composite [1,16].

A paint is a dispersion of pigment particles (e.g., titania) in a clear binder, such as acrylic. The propagation of light through pigmented coatings is of natural interest to the coating and colorant industries, and has been extensively studied over the past century. The optical properties of a freely suspended film (i.e., reflectance,

transmittance, and absorptance) depend on (a) the real and imaginary refractive indices of the pigment and the binder; (b) the size, shape, and concentration of the pigment particles; and (c) the thickness of the film. These optical properties may be determined either *microscopically* or *macroscopically*.

The microscopic approach applies the principles of electromagnetism to analyze the interaction of light with pigment particles, including interparticle effects (i.e., multiple scattering). Mie theory [17] applies well to spherical pigment particles separated by distances large compared to the light wavelength, but is less useful when particles are closely packed or exhibit either geometric or electromagnetic anisotropy. Knowledge of the detailed scattering cross sections of the pigment particles is useful but not sufficient for the simulation for the reflectance of paint-type coatings [18,19]. Most practical colored coatings contain strongly scattering pigments and/or have strongly scattering substrates, making it essential to include multiple scattering effects from the outset. Furthermore, the pigment particles are often close enough together to make the scattering by neighboring particles electromagnetically interdependent [20].

The macroscopic approach treats the coating as a continuous medium with bulk abilities to absorb and scatter light. One of the simplest and most popular continuum models is the two-flux theory introduced by Schuster in 1905 [21] and popularized by Kubelka and Munk [22–26]. The Kubelka–Munk (K–M) model describes the one-dimensional, bidirectional propagation of diffuse light through a film by parameterizing the rates at which the film absorbs and/or backscatters light. Details of the angular dependence of the radiative transfer are neglected, as are polarization effects. Only two spectral optical measurements (reflectances over two different backgrounds, or one reflectance and one transmittance) are needed to compute the two parameters (spectral absorption and backscattering per unit length) that predict the spectral reflectance and spectral transmittance of a coating of arbitrary thickness and background. The utility of this model is limited by its assumption that light is diffuse throughout the film, which fails when a weakly-scattering film is illuminated by collimated light from a spectrometer or the sun.

More sophisticated models track both diffuse and collimated fluxes. Three-flux models [27] track two diffuse fluxes and one collimated flux, while four-flux models [28,29] track two diffuse and two collimated beams. Compared to the K–M model, three- and four-flux theories require additional spectral measurements and spectral parameters, and yield significantly more complex expressions for film reflectance and transmittance. However, they are more accurate than the K–M two-flux model, particularly when applied to films that are both weakly backscattering and weakly absorbing [30].

Color and pigment references [31–33] and pigment manufacturers [5,6] typically report the spectral reflectance of a well-hiding (i.e., visibly opaque, or ''masstone'') coating, and sometimes also that of a tint (mixture with white). This description of the coating's masstone (and tint, if given) is insufficient to determine solar spectral absorption and backscattering coefficients. First, spectral reflectance is typically reported over only the visible spectrum, though manufacturers marketing cool pigments usually report spectral reflectance over the entire solar spectrum. Second, the coating is often NIR-transmitting, making its NIR reflectance dependent on that

of its background (typically a primed metal panel). Third, knowledge of a film's opaque reflectance yields only the ratio of its absorption and backscattering coefficients. Determination of both coefficients requires measurements of either (a) the reflectances of a non-opaque film over two different backgrounds, or (b) the reflectance and transmittance of a non-opaque film.

References sometimes also report the ratio of the absorption and scattering coefficients [23,34], which is equivalent to reporting opaque reflectance. However, our review of the optics and colorant literature identified only a few published spectra of absorption and backscattering coefficients, such as two for titanium dioxide white [35,20] and one for quinacridone red [36]. Vendors of propriety color-formulation software [37–40] have further unpublished K–M coefficient data for the visible spectrum.

A straightforward and useful way to characterize the optical properties of a pigmented coating is to measure its spectral reflectance and transmittance, then calculate its spectral absorptance as $1-\text{reflectance}-\text{transmittance}$. Pigments with weak or strong NIR absorption can be identified by inspection of the spectral absorptance curve. However, knowledge of the spectral reflectance and transmittance of two differently pigmented films is not sufficient to predict the spectral reflectance and transmittance of a film colored with a mixture of the two pigments. Computation of a mixture's optical properties requires the knowledge of the bulk properties of each component pigment (in vehicle), such as the K–M backscattering and absorption coefficients. The simplest such mixture model approximates the backscattering and absorption coefficients of a mixture as the volume-weighted averages of the backscattering and absorption coefficients of its constituents [41].

We balance accuracy and simplicity by introducing a variant of the K–M two-flux model that, while less detailed than true four-flux models, does consider the extent to which incident collimated light has been scattered by passage through the film. This article sets out the theory needed to compute absorption and backscattering coefficients from spectrometer measurements of film reflectance and transmittance, then applies it to several commonly used single-pigment coatings. Model accuracy is checked by comparing the predicted and measured reflectances of each film over various backgrounds. A companion article [10] considers these characterizations pigment-by-pigment, identifying both cool pigments—i.e., those that can be used to make NIR-reflecting or NIR-transmitting cool coatings—and pigments that should be excluded from cool coatings. Our goal is to provide complete solar spectral absorption and backscattering coefficients describing a large palette of pigments usable for architectural coatings.

2. Theory

We present the theory required to compute K–M coefficients from spectrometer measurements in seven stages. Specifically, we

1. Review the standard K–M two-flux model and identify the errors that stem from its assumption that light in the film is fully diffuse.

2. Summarize the K–M solutions that relate film reflectance and transmittance to absorption and backscattering coefficients.
3. Develop the theory needed to adjust the film reflectance and transmittance measured by a spectrometer to correct for "interface" reflectances that occur when light passes to a medium of differing refractive index.
4. Show how to calculate the reflectance of a composite background, such as a clear substrate with an opaque undercoat.
5. Present a technique for computing the magnitude of interface reflectance to incompletely diffused light, to account for the geometry of light striking the interface.
6. Develop a method for estimating the extent to which collimated light is diffused by passage through a scattering film.
7. Summarize our computational algorithm.

The purpose of our measurements and model of radiant transfer in single-pigment coatings is to obtain backscattering and absorption coefficients S and K that approximately characterize the pigment. High precision is not the goal, but a reliable general characterization of each individual pigment is. We cover the solar spectral region from 300 to 2500 nm at 5-nm intervals. Each wavelength is treated independently of all others except for the use of the forward scattering ratio. Since the K–M model applies to diffuse illumination, whereas we are using collimated radiation, the treatment may be expected to be more accurate in strongly scattering films in which a fully diffuse radiation field quickly develops. However, we have used a formulation in which a non-scattering pigment (e.g., a dye) is assigned a K value approximating Beer's law for diffuse radiation traversing a slab. In summary, we are not expecting precise characterization, but expect to extract consistent, reliable, and practical information for each pigment.

2.1. *Two-flux Kubelka–Munk model vs. four-flux Maheu–Letoulouzan–Gouesbet model*

The one-dimensional propagation of light through a coating is approximated by the two-flux K–M theory, in which downward and upward beams can be absorbed and/or backscattered as they traverse the film. All light in the film is assumed to be diffuse (subscript d), either because the film is diffusely illuminated, or because the film is strongly scattering. The downward diffuse flux $i_d(z)$ and upward diffuse flux $j_d(z)$ within the film are modelled by

$$-\frac{di_d}{dz} = -(K+S)i_d + Sj_d, \tag{1}$$

$$\frac{dj_d}{dz} = -(K+S)j_d + Si_d, \tag{2}$$

where K and S are coefficients of absorption and backscattering, respectively. The fluxes and coefficients are wavelength-specific.

The *Maheu–Letoulouzan–Gouesbet* (M–L–G) four-flux model [28,29] removes the K–M assumption that all light in the film is diffuse by tracking two collimated fluxes (i_c,j_c) and two diffuse fluxes (i_d,j_d). Denoting the intensities of the total downwelling flux and total upwelling flux by $i(z) = i_c(z) + i_d(z)$ and $j(z) = j_c(z) + j_d(z)$, respectively, the M–L–G model may be expressed in the form

$$-\left(\frac{di_c}{dz}\right)_{M-L-G} = -\eta^{-1}[K + (1-\sigma)^{-1}S]i_c, \tag{3}$$

$$\left(\frac{dj_c}{dz}\right)_{M-L-G} = -\eta^{-1}[K + (1-\sigma)^{-1}S]j_c, \tag{4}$$

$$-\left(\frac{di}{dz}\right)_{M-L-G} = -(K+S)(\eta^{-1}i_c + i_d) + S(\eta^{-1}j_c + j_d), \tag{5}$$

$$\left(\frac{dj}{dz}\right)_{M-L-G} = -(K+S)(\eta^{-1}j_c + j_d) + S(\eta^{-1}i_c + i_d). \tag{6}$$

The average pathlength parameter η is the ratio of the diffuse beam pathlength to the collimated beam pathlength, which equals 2 for perfectly diffuse light [22,23]. The forward scattering ratio σ is the ratio of light scattered into the forward hemisphere to total scattering. Here, following M–L–G, we have made the simplifying assumption that σ is the same for both collimated and diffuse light.

Applying the K–M model to total fluxes i and j (rather than to the purely diffuse fluxes i_d and j_d) yields flux gradients

$$-\left(\frac{di}{dz}\right)_{K-M} = -(K+S)i + Sj = -(K+S)(i_c + i_d) + S(j_c + j_d), \tag{7}$$

$$\left(\frac{dj}{dz}\right)_{K-M} = -(K+S)j + Si = -(K+S)(j_c + j_d) + S(i_c + i_d), \tag{8}$$

with errors

$$\Delta\left(-\frac{di}{dz}\right) \equiv \left(-\frac{di}{dz}\right)_{K-M} - \left(-\frac{di}{dz}\right)_{M-L-G} = -(K+S)(1-\eta^{-1})i_c + S(1-\eta^{-1})j_c, \tag{9}$$

$$\Delta\left(\frac{dj}{dz}\right) \equiv \left(\frac{dj}{dz}\right)_{K-M} - \left(\frac{dj}{dz}\right)_{M-L-G} = -(K+S)(1-\eta^{-1})j_c + S(1-\eta^{-1})i_c, \tag{10}$$

that arise because the pathlength of collimated light is shorter than that of diffuse light by a factor of η. Since $1-\eta^{-1} > 0$, applying the K–M model to light that is partially collimated and partially diffuse tends to overestimate both (a) attenuation by absorption and backscattering, and (b) intensification by opposite-beam backscattering.

This study relies mainly on the total-flux K–M model [Eqs. (7) and (8)] because it offers relatively compact solutions for film reflectance and transmittance. However, the M–L–G relations for the collimated fluxes [Eqs. (3) and (4)] are used to

estimate the extent to which initially collimated light is diffused by passage through the film.

2.2. K–M model solutions for film reflectance and transmittance

Consider a film of thickness δ illuminated from above at $z = \delta$. If illumination comes from a medium of refractive index equal to that of the film, and both K and S are independent of z, the reflectance of the film's upper surface to downward illumination is

$$R_f \equiv \left(\frac{j}{i}\right)_{z=\delta} = \frac{1 - R_g(a - b\coth bS\delta)}{a - R_g + b\coth bS\delta}, \tag{11}$$

where

$$a \equiv (S + K)/S, \tag{12}$$

$$b \equiv (a^2 - 1)^{1/2} \tag{13}$$

and $R_g \equiv (j_d/i_d)_{z=0}$ is the reflectance of the film's background at $z = 0$. We refer to R_f as the film's "continuous refractive index" (CRI) reflectance, since it assumes that incident light passes to a medium of the same refractive index. The film's *internal transmittance* is

$$\tau \equiv \frac{i_{z=0}}{i_{z=\delta}} = \frac{b}{a\sinh bS\delta + b\cosh bS\delta}. \tag{14}$$

2.3. Determining backscattering and absorption coefficients from film reflectance and transmittance

A film with CRI reflectance $R_{f,0}$ over a black background ($R_{g,0} = 0$) and CRI reflectance $R_{f,1}$ over a non-black background ($R_{g,1} > 0$) has backscattering and absorption coefficients

$$S = \frac{1}{b\delta}\left(\operatorname{arccoth}\frac{1 - aR_{f,0}}{bR_{f,0}}\right) \tag{15}$$

and

$$K = (a - 1)S, \tag{16}$$

where

$$a = \frac{1}{2}\left[R_{f,1} + \frac{R_{f,0} - R_{f,1} + R_{g,1}}{R_{f,0}R_{g,1}}\right]. \tag{17}$$

The value of $R_{f,0}$ (and hence those of S and K) may also be obtained from CRI film reflectances $R_{f,1}$ and $R_{f,2}$ over dissimilar, nonzero background reflectances $R_{g,1}$

and $R_{g,2}$:

$$R_{f,0} = \frac{R_{f,1}R_{g,2} - R_{f,2}R_{g,1}}{R_{g,2} + R_{g,1}(R_{f,1}R_{g,2} - R_{f,2}R_{g,2} - 1)}. \tag{18}$$

A third approach is to determine $R_{f,0}$ and the K–M coefficients from $R_{f,1}$ and τ:

$$R_{f,0} = \frac{1 + R_{f,1}R_{g,1} - \sqrt{(1 - R_{f,1}R_{g,1})^2 + 4(R_{g,1}\tau)^2}}{2R_{g,1}}. \tag{19}$$

Using $R_{f,1}$ and τ to determine K and S can improve accuracy when $R_{f,1} - R_{f,0} \ll 1$ (i.e., $\tau \ll 1$ and/or $R_{g,1} \ll 1$).

The preceding solutions [Eqs. (11)–(19)] may be found in multiple references [22–26].

If the film is weakly absorbing ($K \to 0$), then $a \to 1$; $b \to 0$; and Eqs. (11), (14) and (15) may be evaluated in the non-absorbing limit:

$$\lim_{K\to 0} R_f = \frac{R_g + (1 - R_g)S\delta}{1 + (1 - R_g)S\delta}, \tag{20}$$

$$\lim_{K\to 0} \tau = \frac{1}{1 + S\delta} \tag{21}$$

and

$$\lim_{K\to 0} S = \frac{R_{f,0}}{(1 - R_{f,0})\delta}. \tag{22}$$

Similarly, if the film is weakly scattering ($S \to 0$), we obtain

$$\lim_{S\to 0} R_f = \tau^2 R_g = \exp(-2K\delta)R_g, \tag{23}$$

$$\lim_{S\to 0} \tau = \exp(-K\delta) \tag{24}$$

and

$$\lim_{S\to 0} K = -\frac{\ln \tau}{\delta}. \tag{25}$$

Note that absorption coefficients smaller than $K_{min} \approx 0.1\,mm^{-1}$ or greater than $K_{max} \approx 200\,mm^{-1}$ are difficult to resolve because reducing K below K_{min} or increasing K above K_{max} yields changes in film transmittance and reflectance too small to be accurately measured. For example, Eq. (25) predicts that at these lower and upper absorption-coefficient bounds, a 25-μm-thick non-scattering film would have internal transmittances of 0.998 and 0.007, respectively. The range of resolvable scattering coefficients has the same lower bound ($S_{min} \approx 0.1\,mm^{-1}$) and a significantly higher upper bound ($S_{max} \approx 4000\,mm^{-1}$). At these lower and upper scattering-coefficient bounds, Eq. (21) predicts that a 25-μm-thick nonabsorbing film would have internal transmittances of 0.998 and 0.010, respectively. Thus, computed

K–M coefficients will tend to be clipped to within the ranges $K_{\min} \leqslant K \leqslant K_{\max}$ and $S_{\min} \leqslant S \leqslant S_{\max}$.

2.4. Correcting spectrometer measurements of film reflectance and transmittance for refractive-index discontinuities

Film reflectance measured by an air-filled spectrometer will differ from CRI film reflectance predicted by the K–M model due to the change in refractive index at the air-film interface $z = \delta$. The Saunderson correction [42] relates the film's "observed" reflectance $\tilde{R}_f$—i.e., the value of reflectance that would be observed by an air-filled spectrometer or a pyranometer—to its CRI reflectance R_f:

$$\tilde{R}_f = \omega^i + \frac{(1-\omega^i)(1-\omega^j)R_f}{1-\omega^j R_f}. \tag{26}$$

ω^i and ω^j denote the reflectances of the interface to the downward flux ("downflux") $i(z)$ and upward flux ("upflux") $j(z)$, respectively. Inverting this relationship yields the CRI film reflectance R_f described by the K–M model:

$$R_f = \frac{\omega^i - \tilde{R}_f}{\omega^i + \omega^j(1-\tilde{R}_f) - 1}. \tag{27}$$

Computing the internal transmittance τ from spectrometer measurements is appreciably more complicated. The reflectance $R^i_{1,2}$ and transmittance $T^i_{1,2}$ of downwelling light by a two-layer system $\{1,2\}$ are

$$R^i_{1,2} = R^i_1 + \frac{T^i_1 T^j_1 R^i_2}{1-R^j_1 R^i_2}, \tag{28}$$

$$T^i_{1,2} = \frac{T^i_1 T^i_2}{1-R^j_1 R^i_2}, \tag{29}$$

where T^i_1 and T^i_2 are the upper and lower layers' transmittances of downwelling light, R^i_1 and R^i_2 are their reflectances to downwelling light, and R^j_1 is the upper layer's reflectance to upwelling light [23, p. 124]. The transmittance of downwelling light by a three-layer system $\{1,2,3\}$ is obtained by applying Eq. (29) first to layer 2 over layer 3, and then to layer 1 over the combined layer $\{2,3\}$:

$$T^i_{1,2,3} = \frac{T^i_1 T^i_{2,3}}{1-R^j_1 R^i_{2,3}} = \frac{T^i_1 T^i_2 T^i_3}{(1-R^j_1 R^i_{2,3})(1-R^j_2 R^i_3)}, \tag{30}$$

where the reflectance of the lower system $\{2,3\}$ is given by Eq. (28):

$$R^i_{2,3} = R^i_2 + \frac{T^i_2 T^j_2 R^i_3}{1-R^j_2 R^i_3}. \tag{31}$$

A free-film system (that is, a film surrounded above and below by air) may be considered to have three layers: α, the air-film interface at $z = \delta$; β, the film occupying $0 < z < \delta$; and γ, the film-air interface at $z = 0$. The film's internal

transmittance is non-directional—i.e.,

$$\tau = T_\beta = T^i_\beta = T^j_\beta. \tag{32}$$

If the film has uniform absorption and backscattering coefficients (i.e., $dK/dz = dS/dz = 0$), its reflectance is also non-directional [23, pp. 123–127]:

$$R_\beta = R^i_\beta = R^j_\beta. \tag{33}$$

It can be shown by comparing the bilayer film reflectances R_f and $R^i_{\alpha,\beta}$ predicted by Eqs. (11) and (28) that

$$R_\beta = R_{f,0}. \tag{34}$$

Since the interfaces are non-absorbing,

$$T^i_\alpha = 1 - R^i_\alpha, \tag{35}$$

$$T^i_\gamma = 1 - R^i_\gamma. \tag{36}$$

Eqs. (30)–(36) can be solved to obtain the film's internal transmittance τ from the film's *observed transmittance* $\tilde{T} = T^i_{\alpha,\beta,\gamma}$, yielding

$$\tau = \frac{-(1-R^i_\alpha)(1-R^i_\gamma) + \sqrt{[(1-R^i_\alpha)(1-R^i_\gamma)]^2 + 4R^j_\alpha R^i_\gamma (1-R_{f,0}R^i_\gamma)(1-R^j_\alpha R_{f,0})\tilde{T}^2}}{2R^j_\alpha R^i_\gamma \tilde{T}}, \tag{37}$$

where $R^i_\alpha = \omega^i_\delta$, $R^j_\alpha = \omega^j_\delta$, and $R^i_\gamma = \omega^i_0$.

A film that lies on a clear substrate with air above the film and below the substrate is equivalent to a free-film system in which the film-substrate interface, γ_a, and the substrate-air interface, γ_b, comprise the third layer γ. We obtain τ by evaluating Eq. (37) with R^i_γ given by Eq. (28):

$$R^i_\gamma = R^i_{\gamma_a,\gamma_b} = R^i_{\gamma_a} + \frac{T^i_{\gamma_a} T^j_{\gamma_a} R^i_{\gamma_b}}{1 - R^j_{\gamma_a} R^i_{\gamma_b}} = R^i_{\gamma_a} + \frac{(1-R^i_{\gamma_a})(1-R^j_{\gamma_a})R^i_{\gamma_b}}{1 - R^j_{\gamma_a} R^i_{\gamma_b}}, \tag{38}$$

where $R^i_{\gamma_a} = \omega_{\text{film}\to\text{substrate}}$, $R^j_{\gamma_a} = \omega_{\text{substrate}\to\text{film}}$, and $R^j_{\gamma_b} = \omega_{\text{substrate}\to\text{air}}$.

Eq. (19) expresses film reflectance over black, $R_{f,0}$, in terms of internal transmittance τ, while Eq. (37) expresses τ in terms of $R_{f,0}$. Simultaneous solution yields

$$R_{f,0} = \frac{A - B\sqrt{C}}{D}, \tag{39}$$

where

$$A = (1-R^i_\alpha)^2(1-R^i_\gamma)^2(1+R_{f,1}R_{g,1})R_{g,1} + 2(R_{g,1} - R^j_\alpha R^i_\gamma R_{f,1})([(1+R_{f,1}R_{g,1})R^i_\gamma - R_{g,1}]R^j_\alpha - R^i_\gamma R_{g,1})\tilde{T}^2,$$

$$B = (1-R^i_\alpha)(1-R^i_\gamma)R_{g,1},$$

$$C = (1 - R_\alpha^i)^2(1 - R_\gamma^i)^2(1 + R_{f,1}R_{g,1})^2 + 4(1 - R_\alpha^j R_{f,1})(1 - R_\gamma^i R_{f,1})(R_\alpha^j - R_{g,1})(R_\gamma^i - R_{g,1})\tilde{T}^2,$$

$$D = 2[(1 - R_\alpha^i)^2(1 - R_\gamma^i)^2 R_{g,1}^2 - (R_\gamma^i R_{g,1} - R_\alpha^j[(1 + R_{f,1}R_{g,1})R_\gamma^i - R_{g,1}])\tilde{T}^2].$$

The internal transmittance is obtained by substituting the result of Eq. (39) into Eq. (37).

2.5. Computing background reflectance

The film's background reflectance R_g naturally depends on what lies below the film. There are four configurations relevant to this study, depending on the presence or absence of (a) a transparent substrate below the film and (b) an opaque undercoat below the film or film-substrate system.

1. *No substrate or undercoat*. R_g equals the reflectance of the film-air interface at the film bottom $z = 0$:

$$R_g = \omega_{film\to air}. \tag{40}$$

2. *Undercoat only*. R_g equals the undercoat's CRI reflectance

$$R_u = \frac{\omega^i - \tilde{R}_u}{\omega^i + \omega^j(1 - \tilde{R}_u) - 1}, \tag{41}$$

where $\omega^i = \omega_{air\to undercoat}$, $\omega^j = \omega_{undercoat\to air}$, and $\tilde{R}_u$ is the undercoat's observed reflectance.

3. *Substrate with undercoat*. We compute R_g in two stages. First, we apply the Saunderson correction [Eq. (26)] to R_u to account for the substrate-undercoat interface:

$$R^\star = \omega^i + \frac{(1 - \omega^i)(1 - \omega^j)R_u}{1 - \omega^j R_u}, \tag{42}$$

where $\omega^i = \omega_{substrate\to undercoat}$ and $\omega^j = \omega_{undercoat\to substrate}$. Next, we apply the Saunderson correction to $R^\star$ to account for the film-substrate interface:

$$R_g = \omega^i + \frac{(1 - \omega^i)(1 - \omega^j)R^\star}{1 - \omega^j R^\star}, \tag{43}$$

where $\omega^i = \omega_{film\to substrate}$ and $\omega^j = \omega_{substrate\to film}$.

4. *Substrate only*. Replacing the undercoat in the previous configuration with a substrate–air interface,

$$R^\star = \omega_{substrate\to air}. \tag{44}$$

We then evaluate Eq. (43) as before to obtain R_g.

2.6. Estimating interface reflectance resulting from change in refractive index

Light striking a smooth boundary separating a medium of refractive index n_0 from a medium of another refractive index n_1 will be partly reflected. The magnitude of this "interface reflectance" ω depends on n_0, n_1, and the angular distribution of the light. If the light is perfectly *collimated* (indicated by subscript c), the normal interface reflectance will be

$$\omega_{c,n_0\to n_1} = \left(\frac{n_1 - n_0}{n_1 + n_0}\right)^2. \tag{45}$$

If the light is perfectly *diffuse* (subscript d), the reflectance depends on whether the light is passing from low index to high index ($n_0 < n_1$), or vice-versa ($n_0 > n_1$). Let

$$f(m) = \frac{1}{2} + \frac{(m-1)(3m+1)}{6(m+1)^2} + \left[\frac{m^2(m^2-1)^2}{(m^2+1)^3}\right] \ln\frac{m-1}{m+1} - \frac{2m^3(m^2+2m-1)}{(m^2+1)(m^4-1)} + \left[\frac{8m^4(m^4+1)}{(m^2+1)(m^4-1)^2}\right] \ln m. \tag{46}$$

Then [27], [23, pp. 11–15]

$$\omega_{d,n_0\to n_1} = \begin{cases} f(n_1/n_0), & n_0 < n_1, \\ 1 - (n_1/n_0)^2[1 - f(n_0/n_1)], & n_0 > n_1. \end{cases} \tag{47}$$

An initially collimated beam (say, that generated by a spectrometer) that has passed through a scattering medium will be partially diffuse. We propose approximating the interface reflectance to light with diffuse fraction q by

$$\omega_{n_0\to n_1}(q) = (1-q) \times \omega_{c,n_0\to n_1} + q \times \omega_{d,n_0\to n_1}. \tag{48}$$

Perfectly collimated light has $q = 0$, while perfectly diffuse light has $q = 1$.

Light downwelling through a film system passes from air ($n = 1$) to a paint resin (e.g., acrylic or polyvinylidene fluoride [PVDF], $n = 1.5$); to a transparent substrate, if present (e.g., polyester, $n = 1.65$); and to either an opaque paint undercoat ($n = 1.5$) or a void—i.e., an air-filled black body cavity ($n = 1$). Upwelling light undergoes an analogous series of interface reflections. Interface reflectances are minor when light is perfectly collimated (e.g., $\omega_{c,\text{air}\leftrightarrow\text{resin}} = 0.04$) and when light is perfectly diffuse but passes to a medium of higher n (e.g., $\omega_{d,\text{air}\to\text{resin}} = 0.09$). However, total internal reflectance of rays that strike the interface at supercritical angles ($\theta > \arcsin[n_0/n_1]$) yields large reflectances when diffuse light passes to a medium of lower n (Table 1). For example, $\omega_{d,\text{resin}\to\text{air}}$ has a theoretical value of about 0.60 when light is perfectly diffuse. It should be noted that there is significant uncertainty in the true magnitude of this partial total internal reflectance. For example, studies of light diffused by opal glasses ($n = 1.5$) have measured glass–air interface reflectances ranging from 0.3 to 0.6 [43,44].

Since a spectrometer illuminates a film with collimated light, the diffuse fraction of downwelling light striking the air–film interface at ($z = \delta$) is $q_\delta^i = 0$. The diffuse

Table 1
Reflection due to change in refractive index at a smooth interface

Collimated Light ($q = 0$) From	To $n = 1$ (air)	$n = 1.5$ (paint resin)	$n = 1.65$ (polyester substrate)
$n = 1$ (air)	0	0.04	0.06
$n = 1.5$ (paint resin)	0.04	0	0.002
$n = 1.65$ (polyester substrate)	0.06	0.002	0
Diffuse Light ($q = 1$) From	To $n = 1$ (air)	$n = 1.5$ (paint resin)	$n = 1.65$ (polyester substrate)
$n = 1$ (air)	0	0.09	0.11
$n = 1.5$ (paint resin)	0.60	0	0.03
$n = 1.65$ (polyester substrate)	0.67	0.19	0

fractions at the other interfaces depend on the nature of the film and its background. For example, consider the following three cases for a film system *without substrate*:

1. *Non-scattering film without undercoat*. If $S = 0$ and the film has no undercoat, the downflux and upflux will be fully collimated at all interfaces.
2. *Scattering film without undercoat*. If $S > 0$, the downwelling light striking the film–air interface at the bottom of the film will be partly diffuse. Since this interface ($n = 1.5$ to $n = 1$) preferentially reflects diffuse light, the upwelling light striking the film–air interface at the top of the film will be almost perfectly diffuse unless the scattering is very weak.
3. *Scattering or non-scattering film with undercoat*. If the film has an opaque, diffusely reflecting undercoat (e.g., black or white paint), upwelling light striking the film–air interface at the top of the film will be perfectly diffuse. There is no refractive-index change at the bottom of the film, and hence no interface reflection to consider.

The above description applies also to a film that has a substrate (e.g., glass) with refractive index equal to that of the film. A similar but somewhat more complex accounting is required when the film has a substrate (e.g., polyester) with refractive index different from that of the film.

The diffuse fraction of light striking the various refractive-index interfaces of a film that does not have an undercoat can be estimated by comparing the intensities of the collimated and total fluxes at these interfaces. The diffuse fraction of downwelling light striking the film–air or film–(substrate + air) interface at the

bottom of the film is

$$q_0^i = 1 - i_c(0)/i(0) \tag{49}$$

and that of upwelling light striking the film–air interface at the top of the film is

$$q_\delta^j = 1 - j_c(\delta)/j(\delta). \tag{50}$$

Since the film's observed transmittance—i.e., the ratio of flux leaving the bottom of the film to the *unit* flux incident on the top of the film—is $\tilde{T} = (1 - \omega_0^i)i(0)$ and its observed reflectance is $\tilde{R}_f = \omega_\delta^i + (1 - \omega_\delta^j)j(\delta)$, the total downflux at the bottom of the film and upflux at the top of the film may be expressed in terms of the film measurements as

$$i(0) = \tilde{T}/(1 - \omega_0^i) \tag{51}$$

and

$$j(\delta) = (\tilde{R}_f - \omega_\delta^i)/(1 - \omega_\delta^j). \tag{52}$$

We take the following approach to determine $i_c(0)$ and $j_c(\delta)$—i.e., the collimated downflux just inside the bottom of the film, and the collimated upflux just inside the top of the film. In the K–M and M–L–G models, the film's CRI reflectance of collimated light is zero, because backscattering is assumed to convert collimated light into oppositely directed diffuse light. The film's *observed* reflectance and transmittance of collimated light, $\tilde{R}_c$ and $\tilde{T}_c$, can be determined by applying Eqs. (28) and (29) to the system's three layers—air-film interface, film, and film-air or film-(substrate + air) interface. This yields

$$i_c(0) = \tilde{T}_c/(1 - \omega_{c,0}^i) = \frac{(1 - \omega_{c,\delta}^i)\tau_c}{1 - \tau_c^2 \omega_{c,\delta}^j \omega_{c,0}^i} \tag{53}$$

and

$$j_c(\delta) = (\tilde{R}_c - \omega_{c,\delta}^i)/(1 - \omega_{c,\delta}^j) = \frac{(1 - \omega_{c,\delta}^i)\omega_{c,0}^i \tau_c^2}{1 - \tau_c^2 \omega_{c,\delta}^j \omega_{c,0}^i}. \tag{54}$$

We estimate the internal transmittance of collimated light, τ_c, from Eq. (3), yielding

$$\tau_c = \exp\{-[K + (1 - \sigma)^{-1} S]\delta/\eta\}, \tag{55}$$

where the average pathlength parameter η is assumed to be 2. The forward scattering ratio σ is a fitted parameter, as described in the next section.

2.7. Algorithms

Spectral K–M coefficients can be computed from either (A) observed spectral reflectance and transmittance over a void background; or (B) observed spectral reflectances over two different backgrounds (e.g., opaque black and opaque white). In Method A, we must determine the internal transmittance and CRI reflectance of a film with a void background, which in turn requires estimation of the forward

scattering ratio σ, spectral diffuse fractions, and spectral interface reflectances. This is much more complex than Method B, in which we need only calculate CRI film reflectances with the assumption that light exiting the film-air interface is fully diffuse. However, there are several advantages to Method A. First, the two optical measurements are made on the same specimen, which ensures that the film properties used to compute the K–M coefficients are based on samples of the same thickness. Second, measuring both reflectance and transmittance yields absorptance, which directly indicates whether a film is hot or cool. Third, since light reflected from a film's background makes two passes through the film, it is more accurate to characterize a film with one reflectance and one transmittance than with two reflectances. This is important when the film is nearly opaque, and/or the two backgrounds have similar reflectance (e.g., in the ultraviolet, where a white background is poorly reflecting). Hence, we use Method A.

Taking as inputs the observed spectral reflectance and transmittance of a film with a void background, we seek (a) spectral values of the K–M coefficients, $K(\lambda)$ and $S(\lambda)$; and (b) a wavelength-independent value of σ that minimizes the global error in the predicted value of a third observed spectral film reflectance, such as that over a black background. Algorithm I describes the process for seeking the spectral coefficients given σ; Algorithm II, which calls Algorithm I, describes the optimization of σ.

I. Determining spectral K– M coefficients given a non-spectral forward scattering ratio. We perform the following at each wavelength of interest. If the film is opaque, we report only its CRI reflectance, since in this case it is not possible to calculate both K and S. Otherwise, we compute initial values of interface reflectances by assuming that the light is everywhere collimated. Let subscripts v, b, and w refer to void, opaque black, and opaque white backgrounds, respectively. We iterate the following six steps until either (a) the fractional changes in K and S fall below some threshold (e.g., 1%), or (b) reaching an iteration limit (say, 5).

1. Use the inverse Saunderson correction [Eq. (27)] to calculate CRI film reflectances $R_{f,v}$ and $R_{f,b}$ from their corresponding observed values.
2. Calculate background reflectances $R_{g,v}$ and $R_{g,b}$ from Eqs. (40)–(44).
3. Calculate $R_{f,0}$ and τ from Eqs. (39) and (37), respectively.
4. If $R_{f,0} > 0$:
   (a) Calculate a from Eq. (17).
   (b) If $a > 1$, calculate b, S, and K from Eqs. (13), (15), and (16), respectively.
   (c) If $a \leqslant 1$, assume that $K = 0$ and evaluate S from Eq. (22).
5. If $R_{f,0} \leqslant 0$, assume that $S = 0$ and evaluate τ and K from Eqs. (24) and (25), respectively.
6. Calculate new values of the interface reflectances ω_δ^j and ω_0^i by applying Eqs. (49)–(55) to the current values of S, K, ω_δ^j and ω_0^i.

When the iterations finish, we calculate the CRI film reflectance over each background (void, black, and white) from K and/or S using Eq. (11), (20), or (23).

We then calculate the corresponding observed reflectances via the Saunderson correction [Eq. (26)].

II. Determining non-spectral forward scattering ratio. We choose the value of σ between 0 and 1 that minimizes the difference between the measured and calculated observed values of the film's reflectance over black. We seek a wavelength-independent value of σ to keep the model simple. Specifically, we minimize the global error $\varepsilon = \chi + \mu$ over M wavelengths, where

$$\chi = \left(\frac{1}{M} \sum_{m=1}^{M} \Delta_m^2 \right)^{1/2}, \tag{56}$$

$$\mu = \max |\Delta_m|, m = 1 \ldots M \tag{57}$$

and

$$\Delta_m = \tilde{R}_{\mathrm{f,calc}}(\lambda_m) - \tilde{R}_{\mathrm{f,meas}}(\lambda_m). \tag{58}$$

Our choice of global error norm ε helps avoid values of σ that yield a small RMS error χ but generate large Δ_m at one or more wavelengths.

3. Experiment

The optical properties of 87 pigmented films—4 white, 21 black or brown, 14 blue or purple, 11 green, 9 red or orange, 14 yellow, and 14 pearlescent—were characterized by computing spectral K–M coefficients and non-spectral forward scattering ratios from spectral measurements of film reflectance and transmittance.

3.1. Sample preparation

Twenty-six PVDF resin paint films were provided by a manufacturer of coil-coating paints. Another 34 acrylic paints were purchased as artist colors, and the remaining 27 coatings were acrylic-base letdowns (dilutions) of cool (primarily metal-oxide) pigment dispersions from pigment manufacturers. The PVDF and acrylic resins in these coatings each have refractive index $n = 1.5$.

Each PVDF film was prepared by (a) using a wirewound rod (a long cylindrical rod covered with a single winding of tightly wrapped wire) to coat an aluminum substrate; (b) baking and quenching the coating; (c) dissolving the aluminum with hydrochloric acid; and then (d) rinsing the film with water. We prepared a substrated film of each acrylic paint by coating a 25-μm thick sheet of clear Mylar-D® polyester ($n = 1.65$; non-scattering; absorptance <0.02 at $400-2100$ nm, <0.07 at $325-400$ nm and 2100–2500 nm; strongly absorbing below 325 nm, approaching 0.9 absorptance at 300 nm) with a wirewound rod, then allowing the paint to dry overnight at room temperature. Film thicknesses (excluding substrate, if any) ranged from 10 to 37 μm.

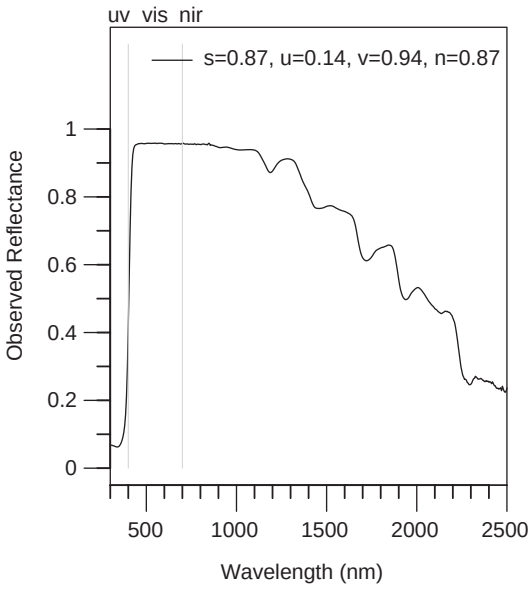

Fig. 2. Observed spectral reflectance of an opaque white background (1.5-mm thick TiO_2-white acrylic paint film).

Three 35-mm × 40-mm samples of each film were placed in glassless slide mounts, and the central thickness of each sample measured with a micrometer (accuracy ±2 μm). The back of the first sample was coated with an opaque layer of black paint (synthetic black iron oxide, 0.9 ± 0.2 mm, non-reflecting); the back of the second sample was coated with an opaque layer of white paint (titanium dioxide, 1.6 ± 0.4 mm; spectral reflectance shown in Fig. 2); and the back of the third sample was not coated. These film backgrounds are denoted "black," "white," and "void," respectively. The final term refers to the state of having no undercoating, in which case light passing through the film enters an air-filled light trap when the film's reflectance is measured in a spectrometer.

3.2. Optical measurements and corrections

A Perkin–Elmer Lambda-900 UV-VIS-NIR spectrometer equipped with a 150-mm Labsphere integrating sphere was used to measure each paint film's reflectance over black, reflectance over white, reflectance over void, and transmittance. The specular components of both reflectance and transmittance were included. Optical measurements were performed at 5-nm intervals over the solar spectrum (300–2500 nm), and were subject to two corrections.

A. Removing thin-film interference. First, thin-film interference induced by the uniform thickness of the polyester substrate creates noticeable ripples in the measured reflectance and transmittance of acrylic paints at wavelengths where

the paint film is highly transmitting. Hence, the measured spectral reflectance and transmittance of films with substrates were smoothed by convolution with a discrete Gaussian filter when the measured spectral transmittance exceeded a threshold. The filter width (±10 wavelengths), spread (half width/3), and transmittance threshold (0.7) were sized to remove as much of the thin-film interference as possible while minimizing distortion of true spectral features.

B. Removing detector-transition discontinuities. The spectrometer has two adjacent light detectors at the bottom of its integrating sphere: a UV–VIS photomultiplier tube for wavelengths below 860 nm, and a lead-sulfide NIR sensor for wavelengths of 860 nm and greater. It is common to observe a blip (i.e., a small but spectrally rapid change) in measured reflectance and/or transmittance near this detector transition. Since some films with blips also exhibited several slightly negative values of absorptance (1-reflectance–transmittance) in the NIR, we concluded that the NIR detector's signal was more likely in error.

We suspect that this discontinuity stems from the design of the integrating sphere. First, the baffle that shields the UV–VIS sensor from beam radiation may imperfectly shield the neighboring NIR sensor. Second, the efficiency of integrating sphere varies with the exact location of the reflected specular spot, which in turn depends on target texture and curvature [45]. Errors are roughly ±1% of the reflected specular component in most of the solar spectrum, and closer to ±2% beyond 2000 nm where the reflectance of the sphere's Spectralon® surface is a little lower. (These estimates are based on the reflectance of a mirror that is tipped slightly to move the specular spot by several millimeters.) Since the phototube detector used for the UV and visible measurements and the lead-sulfide detector covering the infrared beyond 860 nm are not in exactly the same position within the integrating sphere, the integrating sphere efficiency errors can be different, resulting in small discontinuities near 860 nm.

We adjusted the reflectances and transmittances measured by the NIR detector by first extrapolating a "corrected" value at 860 nm from the values at 850 and 855 nm, then adding the difference between the corrected and measured 860-nm values to measured values at all wavelengths greater than 860 nm. This correction eliminated the slightly negative absorptances.

Observations of negative absorbance may also result if the spot at which the film transmittance is measured is thinner than the spot at which film reflectance is measured. Consider a non-absorbing sample with exactly 0.5 transmittance and 0.5 reflectance. If the transmittance measurement is made on a part of the sample that is 5% thinner than the spot at which reflectance is measured, the transmittance measurement may be too large by about 0.025, and sample absorptance (1-reflectance–transmittance) may appear to be negative.

3.3. Computing pigment volume concentration

The pigment volume concentration (PVC) of each dry coating was computed either from the specific gravities of paint, pigment, and binder, or from pigment-load information supplied by the manufacturer.

4. Results

Model performance was gauged by examining (a) spectral characterizations of six representative pigments and (b) the accuracy with which computed K–M coefficients predict film reflectance over black and white backgrounds. The six sample results are presented below. Spectral characterizations of all 87 pigmented films are reported in a companion article [10].

4.1. Detailed spectral analyses of six representative pigments

The measured and computed spectral properties of films colored with each of six pigments—(a) titanium dioxide white, (b) carbon black, (c) iron oxide red, (d) phthalo blue, (e) phthalo green, and (f) mica flakes coated with titanium dioxide—are shown in Fig. 3. Charted for each coating are (I) measured optical properties of a film over void; (II) computed K–M coefficients; (III) computed diffuse fractions and interface reflectances; and (IV) measured and computed values of reflectance over black and white backgrounds.

Chart I shows the film's measured reflectance $\tilde{R}_{f,v}(\lambda)$ and measured transmittance $\tilde{T}(\lambda)$ over void, which are used to compute K–M coefficients; and computed absorptance, $\tilde{A}(\lambda) = 1 - \tilde{R}_{f,v}(\lambda) - \tilde{T}(\lambda)$. Its legend tabulates solar ("s"), UV ("u"), visible ("v"), and NIR ("n") spectrally integrated values computed by weighting each property with the air-mass 1.5 solar spectral irradiance shown in Fig. 1.

Chart II presents backscattering and absorption coefficients $S(\lambda)$ and $K(\lambda)$, along with the non-spectral forward scattering ratio σ that minimizes the error in predicted reflectance over black. In this graph, non-zero K–M coefficients are assigned a minimum value of $0.1\,\mathrm{mm}^{-1}$, which is an estimate of the smallest resolvable non-zero value for K and S (cf. Section 2.3). At wavelengths where only S is shown, K was assumed to be zero, and vice versa. Where the film is opaque, neither S nor K is shown.

Chart III shows a few of the ancillary properties computed in the process of generating K–M coefficients, namely the diffuse fraction q and the interface reflectance ω for fluxes exiting the top and bottom of the void-backed film. These interface reflectances are used to correct the measured values of film reflectance and transmittance during computation of K and S (cf. Section 2.4).

Chart IV compares values of over-black and over-white observed reflectances $\tilde{R}_{f,b}(\lambda)$ and $\tilde{R}_{f,w}(\lambda)$ computed from the K–M coefficients to values measured with the spectrometer. The computed reflectance over black (ROB) is fitted to its corresponding measured value by the choice of the non-spectral forward scattering ratio. However, the computed reflectance over white (ROW) is independent of the measured ROW, since the latter property is not used to calculate K–M coefficients. Hence, the error in ROW serves as a strong check for the accuracy of K and S, while the error in ROB serves as a weaker check. Also shown in this chart are the RMS errors χ_w and χ_b in predictions of ROW and ROB, and the measured over-white and over-black NIR reflectances N_w and N_b.

A. Titanium Dioxide White. Titanium dioxide white (Fig. 3a) scatters strongly in most of the solar spectrum but absorbs strongly in the UV (below 400 nm). In most of the visible and infrared spectra there is little absorption. The inferred scattering coefficient S declines by two orders of magnitude between 400 and 2500 nm, which is typical behavior for scattering pigments. For generic TiO_2 (rutile) we have 200-nm particles of refractive index ≈ 2.7. For well-dispersed particles that are much smaller than the wavelength, we expect Rayleigh behavior in which the scattering cross section decreases as λ^{-4}. Thus we might expect S to decline by more than three orders of magnitude between 400 and 2500 nm. On a log–log plot (not shown), the slope of the scattering curve is increasingly negative at longer wavelengths, reaching about -3 at 2500 nm, so that the Rayleigh limit is not quite reached. The "background" or minimum absorption coefficient here of $0.5\,mm^{-1}$, multiplied by film thickness, is about 0.015. Since, as mentioned earlier, absorptance measurement uncertainties are on the order of 0.01, no definite conclusion can be reached about the actual minimum absorptance. In fact, the underprediction of reflectance over white from 600 to 1400 nm suggests that the film absorptance may be slightly overestimated.

The absorption and backscattering curves are interrupted at four wavelengths in the UV where the 29-μm thick film is opaque.

Chart I shows a small upward shift in reflectance near 860 nm, where the spectrometer switches from its UV–VIS sensor to its NIR sensor. This indicates that the algorithm to remove such discontinuities (cf. Section 3.2) is imperfect. The small peaks in absorptance (Chart I) and absorption coefficient (Chart II) at 1700 nm are a feature of the binder, since they appear in many differently pigmented films, including some without substrates. Most polymers have significant IR absorption due to hydrogen vibrations of C–H structures in the 2000–2400 nm range [46]. Weaker overtones appear in the 1600–1800 nm regions. Thus, some of the NIR absorptance features seen here are due to the polymer binder. However, it is not unusual for TiO_2 pigments to be coated with metal hydroxides, and hydrogen vibrations in H_2O and OH groups may sometimes appear as well.

Chart III indicates that the computed scattering is strong enough to fully diffuse light exiting the bottom of the film ($q_0^i = 1$) at wavelengths <1200 nm, and to fully diffuse the light exiting the top of the film ($q_\delta^i = 1$) at all wavelengths (cf. Section 2.6). The non-spectral FSR $\sigma = 0.69$ is in agreement with the theoretical prediction of about 0.65 obtained by assuming a particle diameter of 200 nm, a relative refractive index of $(2.75 + 0i)/1.5$, a PVC of 5%, and a free-space wavelength of 550 nm [47, Fig. 1].

Fig. 3. (ii/ii) Measurements and model calculations for six coatings: (a) titanium dioxide white, (b) carbon black, (c) iron oxide red, (d) phthalo blue, (e) phthalo green, and (f) mica flakes coated with titanium dioxide. Shown from top to bottom are (I) measured reflectance, transmittance, and absorptance of film with void background; (II) Kubelka–Munk backscattering and absorption coefficients S and K, and non-spectral forward scattering ratio σ; (III) computed diffuse fraction and interface reflectance of fluxes exiting top and bottom of film; and (IV) measured and computed film reflectances over white [w] and black [b] backgrounds, measured NIR reflectance N, and the RMS error χ.

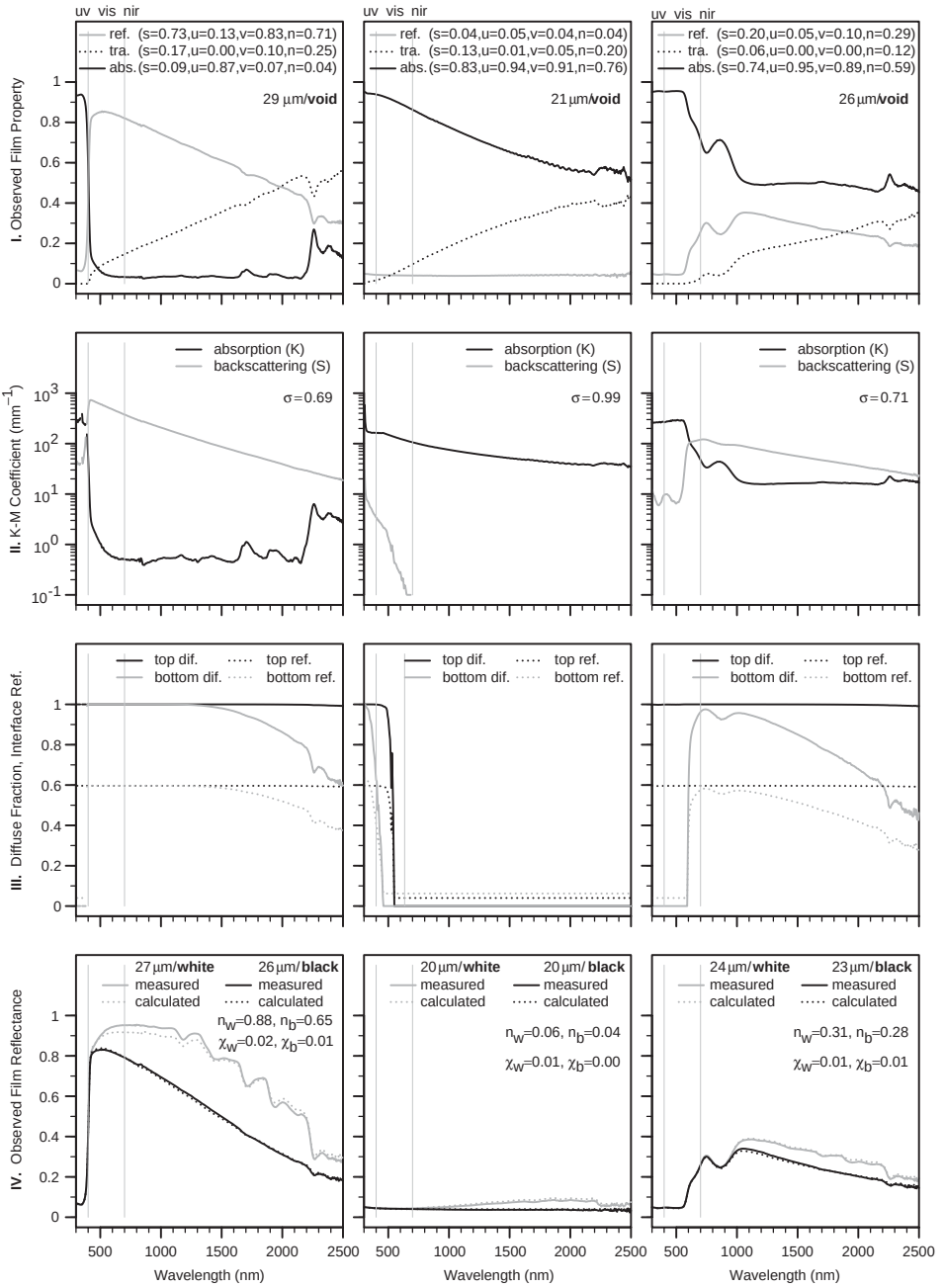

(a)
Inorganic Oxide White
Ishihara Tipaque CR-90 (PW 6)
15% PVC
{titanium dioxide white}

(b)
Carbon Black
Amorphous Carbon Black (PBk 7)
0.4% PVC
{carbon black}

(c)
Red Iron Oxide (i)
Bayer Bayferrox 6622 Iron Oxide (PR 101)
9% PVC
{iron oxide red}

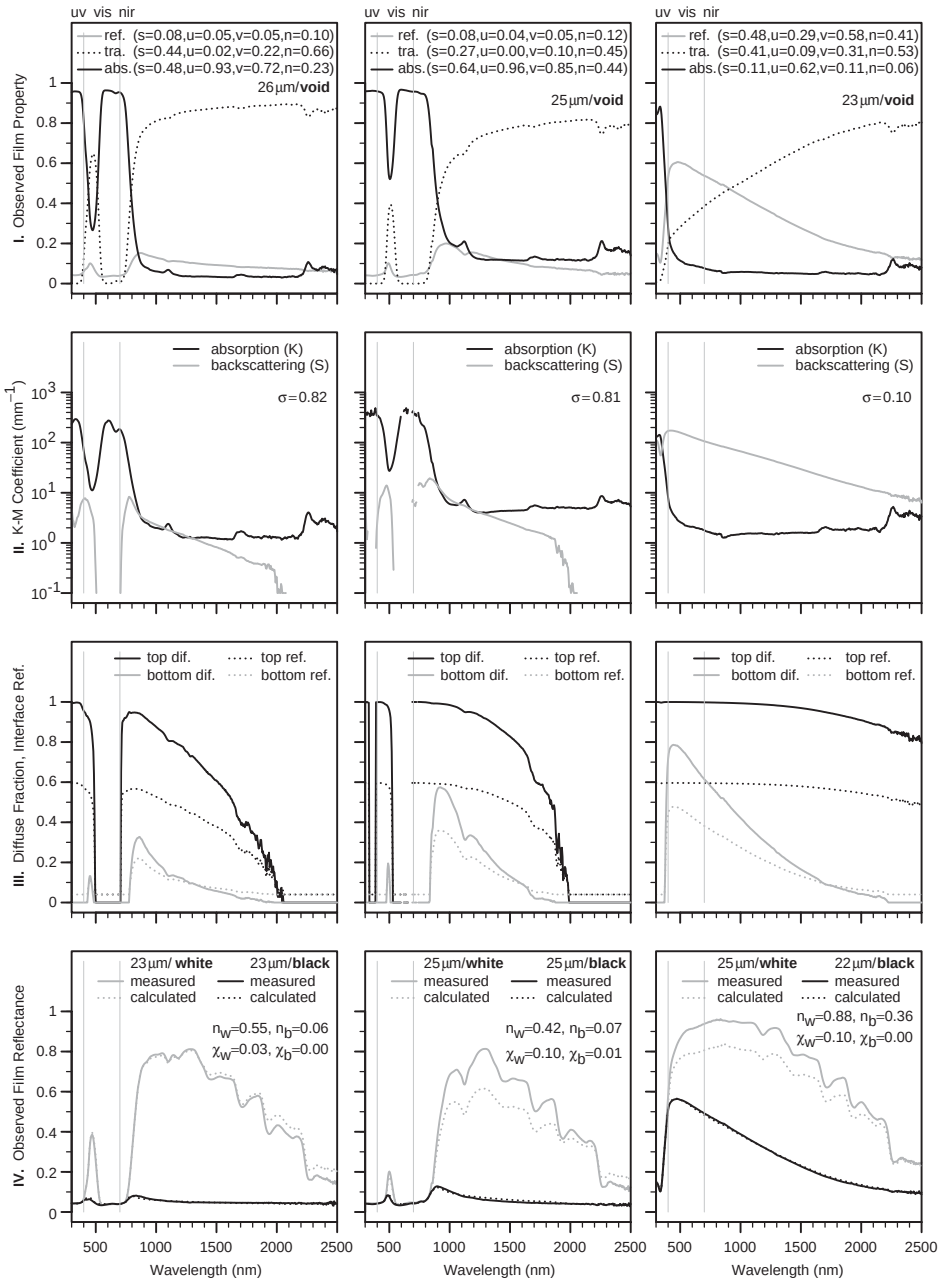

(d)
Phthalo Blue (ii)
Toyo Lionel BF-28201 (PB 15)
5% PVC
{phthalocyanine blue}

(e)
Phthalo Green (ii)
Clariant GT-674-D Endurophthal
Green B (PG 7)
4% PVC
{phthalocyanine green}

(f)
Bright White (Pearlescent)
Engelhard Exterior Mearlin 139X Bright White
11% PVC
{mica + titanium dioxide}

Fig. 3. (ii/ii)

The computed ROB closely matches the measured ROB, but the calculated ROW is about 0.04 low over the range 600–1300 nm (Chart IV). We consider three possible explanations.

1. *Inaccurate K–M coefficients.* Underprediction of film reflectance suggests that the algorithm may have overestimated K and/or underestimated S. At 1000 nm, $K \approx 0.5\,\mathrm{mm}^{-1}$, $S \approx 200\,\mathrm{mm}^{-1}$, the CRI reflectance of the opaque white background is 0.98, and the observed reflectances over black and white are underpredicted by 0.01 and 0.04, respectively. Eq. (11) indicates that reducing K to zero while leaving S unchanged would increase the over-black and over-white reflectances by 0.007 and 0.02, respectively. Alternately, increasing S fivefold to $1000\,\mathrm{mm}^{-1}$ while leaving K unchanged would yield corresponding increases of 0.15 and 0.02. Setting K to zero—which assumes that neither the pigment nor the binder absorb any light whatsoever—would match the over-black reflectances, but leave the ROW underpredicted by 0.02. Setting $S = 1000\,\mathrm{mm}^{-1}$ would yield the same underprediction of ROW, while wildly overpredicting ROB. Of these, the mostly likely explanation is that we have overpredicted K.
2. *Inaccurate film-air interface reflectance.* We may have misestimated the film-air interface reflectance used in the Saunderson correction [Eq. (26)] to the predicted reflectances over black and white. We use the theoretical value $\omega_{\mathrm{film}\to\mathrm{air}} = 0.6$ because light exiting the top of a diffusely undercoated film should be fully diffuse. However, since reflectances as low as 0.3 have been observed for diffuse light passing from $n = 1.5$ to $n = 1$ [44], we consider the effects of changing ω. The CRI ROB and ROW at 1000 nm are 0.84 and 0.95, respectively. When $\omega = 0.60$, the corresponding observed film reflectances are 0.69 and 0.91. Reducing ω to 0.5 increases the observed reflectances by 0.05 and 0.01, respectively; increasing ω to 0.7 decreases them by 0.06 and 0.03. Hence decreasing ω would aggravate the ROB error much more than it would reduce the ROW error, and increasing ω would increase both ROB and ROW errors.
3. *Inaccurate background reflectance.* The reflectance of the sample's opaque white background might be higher than assumed. This is unlikely because the layer of opaque white paint whose reflectance is charted in Fig. 2 is about 1.5-mm thick, and has a spectral transmittance less than 0.01 over virtually the entire solar spectrum. Thus, while making the white undercoating too thin could reduce the reflectance of the sample over white, making the white undercoating too thick should not measurably increase the over-white reflectance.

B. Carbon black. Carbon black (Fig. 3b) is a strongly absorbing pigment with an exponentially-decreasing absorption coefficient that falls half a decade over the solar spectrum (Chart II). It has weak scattering in the UV and visible spectra typical of soot [48], and is essentially non-scattering in the NIR. We note that its measured reflectance over black is approximately 0.04 in the visible and NIR spectra (Chart IV), which is the result expected for a collimated beam passing from air ($n = 1$) to a non-scattering paint ($n = 1.5$). In these spectra, the CRI ROB $R_{\mathrm{f},0}$ computed from Eq. (39) is slightly negative (mean value −0.003); hence, the film is assumed to be

non-scattering, the top and bottom diffuse fractions are set to zero (Chart III), and the absorption coefficient is computed in the non-scattering limit from Eq. (25).

The 21-μm thick film prepared from a diluted carbon black artist paint is quite transparent (Chart I), making it easy to compute K from its transmittance. The forward scattering ratio $\sigma = 0.99$ has little meaning because $S = q = 0$ in the NIR. The near-perfect matches between calculated and measured reflectances over black and white match (Chart IV) likely arise from the film's strong absorption, possibly because absorptive attenuation reduces the influence of scattering on film reflectance.

C. Iron oxide red. Iron oxide red (Fig. 3c) has very strong absorption at wavelengths below 600 nm, and strong scattering at wavelengths longer than 660 nm (Chart II), leading to its dark red appearance over either a white or black background (Chart IV). At wavelengths below 600 nm, the bottom diffuse fraction is forced to zero because the high absorptance ($K > 200\,\mathrm{mm}^{-1}$) generates small values of $i_c(0)$ and $i(c)$, which in turn yield an unphysical (i.e., negative) estimate of diffuse fraction. The matches between predicted and measured reflectances (Chart IV) are quite good, probably because the absorption is never small ($K > 20\,\mathrm{mm}^{-1}$). Other iron oxide red pigments showed less NIR absorption than this pigment [10].

D, E. Phthalocyanine blue and green. Phthalocyanine blue (Fig. 3d) and phthalocyanine green (Fig. 3e) are weakly scattering, dyelike pigments with strong absorption in parts of the visible and NIR. Their strong absorptances in the reddish potions of the visible spectrum (Chart I) give each a dark blue or green appearance over a white background, and almost black appearances over a black background (Chart IV). Both of these PVDF-based free films are about 25-μm thick, have a PVC of about 5%, are fitted with $\sigma \approx 0.8$, and show excellent agreement between measured and calculated reflectances over black. However, the error in ROW is much larger for the green than it is for the blue. At 1280 nm (peak green ROW error), the measured reflectances of green over white and blue over white are each 0.81, but the green film's K and S are each three times larger than those of the blue film. Thus, while the model closely estimates the reflectance of blue over white (error 0.01), its underpredicts the reflectance of green over white by 0.20.

F. Mica flakes coated with titanium dioxide. This pearlescent white film (Fig. 3f) containing mica flakes coated with titanium dioxide is strongly scattering and weakly absorbing in the visible and NIR spectra. Its absorption and backscattering curves are shaped like those of titanium dioxide (Fig. 3a), but K and S are about half an order of magnitude higher and lower, respectively (Chart II). The K–M model is not expected to accurately describe pearlescent films. Since these platelike pigment particles tend to align with the plane of the films, the collimated light that they scatter is unlikely to be uniformly diffuse. This particular pearlescent exhibits one of the poorest fits to ROW, second only to that of the aforementioned phthalo green. The very low $\sigma = 0.1$ may result from specular reflection by the flakes.

4.2. Accuracy of K–M model vs. backscattering and absorption thicknesses

Fig. 4 charts errors in predicted ROW and ROB vs. backscattering thickness $S\delta$ and absorption thickness $K\delta$ using about 38,000 measurements (87 pigments × 441

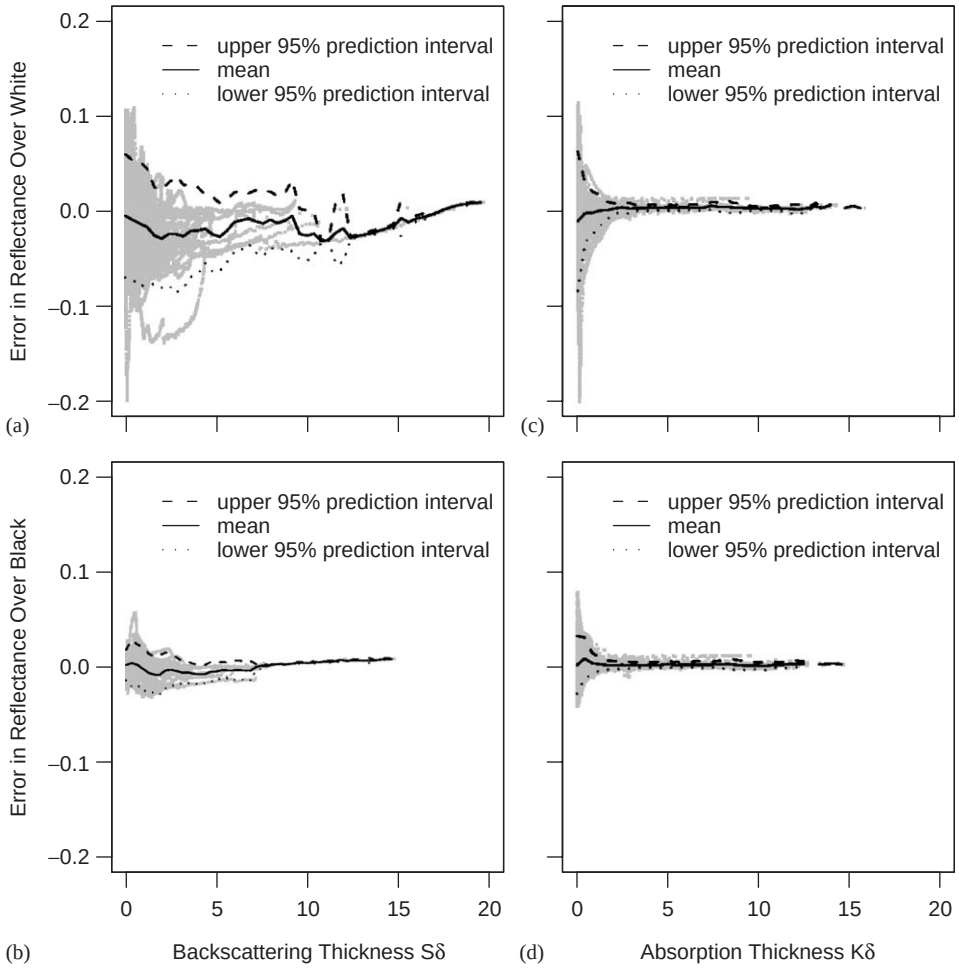

Fig. 4. Errors in reflectances computed from Kubelka–Munk coefficients. Shown are (a, b) computed − measured values of observed film reflectance over (white, black) backgrounds vs. backscattering thickness $S\delta$; and (c, d) the same errors vs. absorption thickness $K\delta$.

wavelengths/pigment). On average (as indicated by the mean error curves in charts [a] and [b]), the model underpredicts both ROW and ROB. As suggested by a prior theoretical error analysis of the K–M model [30], prediction errors are greatest when the film is weakly scattering and/or weakly absorbing. Typical errors ranges (that is, the 95% prediction interval limits) are −0.07 to +0.06 (ROW) and −0.02 to +0.02 (ROB) for weakly scattering films; −0.08 to +0.06 (ROW) and −0.02 to +0.02 (ROB) for weakly absorbing films; −0.04 to +0.01 (ROW) and −0.01 to +0.01 (ROB) for strongly scattering films; and less than ±0.01 (ROW and ROB) for strongly absorbing films.

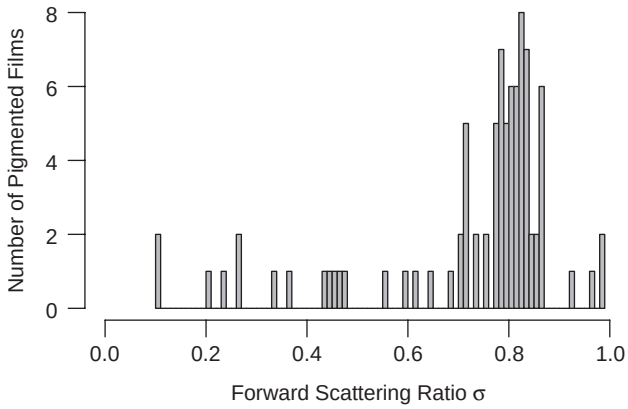

Fig. 5. Frequency distribution of non-spectral forward scattering ratio σ. Most pigmented films characterized were strongly forward scattering.

4.3. Fitted forward scattering ratio

The distribution of forward scattering ratios computed for the 87 coatings shown in Fig. 5 indicates that most of the tested paints are strongly forward scattering ($0.7 \leqslant \sigma \leqslant 0.9$).

5. Conclusions

We have presented a variant of the two-flux K–M model that determines backscattering and absorption coefficients primarily from the reflectance and transmittance of a film over a void background, using the reflectance over black to obtain an estimate of the forward scattering ratio. Detailed spectral analyses of six representative pigments combined with statistical analyses of about 38,000 spectral measurements indicate several strengths and weaknesses of the model.

1. The K–M coefficients appear qualitatively correct, in the sense that the absorption coefficient reproduces the spectral features of the film's absorptance, and the backscattering coefficient exhibits those of the film's reflectance over black.
2. The film reflectances over white and black backgrounds computed from K–M coefficients closely match corresponding measured values for the first four representative pigments—titanium dioxide white, carbon black, iron oxide red, and phthalo blue—with RMS errors in ROW and ROW not exceeding 0.03 and 0.01, respectively. The last two representative pigments—phthalo green and pearlescent bright white—exhibit large errors (RMS 0.10) in predicted ROW.
3. The model on average underpredicts both ROB and ROW, with errors on the order of about ± 0.07 for ROW and ± 0.02 for ROB when a film is weakly

scattering and/or weakly absorbing. The latter feature suggests that the model is likely to underestimate the NIR reflectance of cool (weakly NIR absorbing) films.

Acknowledgements

This work was supported by the California Energy Commission (CEC) through its Public Interest Energy Research Program (PIER), by the Laboratory Directed Research and Development (LDRD) program at Lawrence Berkeley National Laboratory (LBNL), and by the Assistant Secretary for Renewable Energy under Contract No. DE-AC03-76SF00098. The authors wish to thank CEC Commissioner Arthur Rosenfeld and PIER program managers Nancy Jenkins and Chris Scruton for their support and advice. Special thanks go also to Mark Levine, director of the Environmental Energy Technologies Division at LBNL, and Stephen Wiel, head of the Energy Analysis Department at LBNL, for their encouragement and support in the initiation of this project. We also wish to thank the following people for their assistance: Kevin Stone and Melvin Pomerantz, LBNL; Michelle Vondran, John Buchko, and Robert Scichili, BASF Corporation; Richard Abrams, Robert Blonski, Ivan Joyce, Ken Loye, and Ray Wing, Ferro Corporation; Tom Steger and Jeffrey Nixon, Shepherd Color Company; and Robert Anderson, Liquitex Artist Materials.

References

[1] R.F. Brady, L.V. Wake, Principles and formulations for organic coatings with tailored infrared properties, Prog. Org. Coat. 20 (1) (1992) 1–25.
[2] G. Burkhart, T. Detrie, D. Swiler, When black is white, Paint and Coatings Industry Magazine, January 2001.
[3] T.R. Sliwinski, R.A. Pipoly, R.P. Blonski, Infrared reflective color pigment, US Patent 6,174,360 B1, January 16, 2001.
[4] J.D. Nixon, The chemistry behind 'Cool Roofs', eco-structure 1 (1) (2003) 63–65.
[5] Ferro Corporation, Cool Colors™ and Eclipse™ pigments, http://ferro.com.
[6] Shepherd Color Company, Arctic infrared-reflecting pigments, http://shepherdcolor.com.
[7] BASF Industrial Coatings, Ultra-Cool™: the new heat reflective coatings from BASF, http://www.ultra-cool.basf.com.
[8] Custom–Bilt Metals, Ultra-Cool™ coating saves energy and money on Custom-Bilt metals roofing systems, http://www.custombiltmetals.com.
[9] MCA Tile, MCA Tile ENERGY STAR roof products, http://www.mcatile.com.
[10] R. Levinson, P. Berdahl, H. Akbari, Solar spectral optical properties of pigments – Part II: survey of common colorants, Sol. Energy Mater. Sol. Cells 89 (4) (2005) 351–389, this issue; doi:10.1016/j.solmat.2004.11.013.
[11] ASTM, ASTM G 173-03: standard tables for reference solar spectral irradiance at air mass 1.5: direct normal and hemispherical on 37° tilted surface, Technical report, American Society for Testing and Materials, 2003.
[12] R. Levinson, H. Akbari, S. Konopacki, S. Bretz, Inclusion of cool roofs in nonresidential Title 24 prescriptive requirements, Report LBNL-50451, Lawrence Berkeley National Laboratory, Berkeley, CA, 2002.
[13] R. Levinson, H. Akbari, S. Konopacki, S. Bretz, Inclusion of cool roofs in nonresidential Title 24 prescriptive requirements, J. Energy Policy 33 (2005) 151–170.

[14] P. Berdahl, H. Akbari, L.S. Rose, Aging of reflective roofs: soot deposition, Appl. Opt. 41 (12) (2002) 2355–2360.
[15] S. Konopacki, H. Akbari, M. Pomerantz, S. Gabersek, L. Gartland, Cooling energy savings potential of light-colored roofs for residential and commercial buildings in 11 US metropolitan areas, Report LBNL-39433, Lawrence Berkeley National Laboratory, Berkeley, CA, 1997.
[16] Yasuhiro Genjima, Haruhiko Mochizuki, Infrared radiation reflector and infrared radiation transmitting composition, US Patent 6,366,397 B1, April 16, 2002.
[17] M. Born, E. Wolf, Principles of Optics, seventh ed., Cambridge University Press, Cambridge, 1999.
[18] H.C. van de Hulst, Light Scattering by Small Particles, Dover Publications, New York, 1981.
[19] C.F. Bohren, D.R. Huffman, Absorption and Scattering of Light by Small Particles, Wiley, New York.
[20] L.E. McNeil, R.H. French, Multiple scattering from rutile TiO_2 particles, Acta Mater. 48 (2001) 4571–4576.
[21] A. Schuster, Radiation through a foggy atmosphere, Astrophys. J. 21 (1) (1905) 1.
[22] P. Kubelka, New contributions to the optics of intensely light-scattering materials, part I, J. Opt. Soc. Am. 38 (1948) 448–457.
[23] G. Kortum, Reflectance Spectroscopy: Principles, Methods, Applications, Springer, Berlin, 1969.
[24] C.F. Bohren, Multiple scattering of light and some of its observable consequences, Am. J. Phys. 55 (6) (1987) 524–533.
[25] D.B. Judd, Color in Business, Science, and Industry, Wiley, New York, 1952.
[26] R.M. Johnston, Pigment Handbook, vol. III, Color Theory, Wiley, New York, 1988, pp. 229–288, (Chapter D–b).
[27] J.W. Ryde, The scattering of light by turbid media: part I, Proceedings of the Royal Society of London: Series A, vol. 131 (817), May 1931, pp. 451–464.
[28] B. Maheu, J.N. Letoulouzan, G. Gouesbet, Four-flux models to solve the scattering transfer equation in terms of Lorenz–Mie parameters, Appl. Opt. 23 (19) (1984) 3353–3362.
[29] W.E. Vargas, Generalized four-flux radiative transfer model, Appl. Opt. 37 (13) (1998) 2615–2623.
[30] W.E. Vargas, G.A. Niklasson, Applicability conditions of the Kubelka–Munk theory, Appl. Opt. 36 (22) (1997) 5580–5586.
[31] Y.S. Touloukian, D.P. DeWitt, R.S. Hernicz, Thermal Radiative Properties: Coatings, vol. 9, Thermophysical Properties of Matter, IFI/Plenum, New York, 1972.
[32] P.A. Lewis, Pigment Handbook, vol. 1, Wiley, New York, 1988.
[33] R. Mayer, The Artist's Handbook of Materials and Techniques, fifth ed., Viking Penguin, 1991.
[34] R.S. Berns, Billmeyer and Saltzman's Principles of Color Technology, third ed., Wiley, New York, 2000.
[35] W.E. Vargas, G.A. Niklasson, Generalized method for evaluating scattering parameters used in radiative transfer models, J. Opt. Soc. Am. A 14 (9) (1997) 2243–2252.
[36] L.E. McNeil, R.H. French, Light scattering from red pigment particles: multiple scattering in a strongly absorbing system, J. Appl. Phys. 89 (1) (2001) 283–293.
[37] Avantes, Mix2Match color matching software, http://avantes.com.
[38] Color-Tec, Color formulation software, http://color-tec.com.
[39] Datacolor, Paintmaker laboratory software, http://datacolor.com.
[40] GretagMacbeth, ProPalette® plastics/coatings color formulation and quality control software,http://gretagmacbeth.com.
[41] E. Allen, Optical Radiation Measurements, vol. 2, Colorant Formulation and Shading, Academic Press, New York, 1980, pp. 289–336 (Chapter 7).
[42] J.L. Saunderson, Calculation of the color of pigmented plastics, J. Opt. Soc. Am. 32 (12) (1942) 727–736.
[43] J.W. Ryde, B.S. Cooper, The scattering of light by turbid media: part II, Proc. R. Soc. London. Ser. A 131 (817) (1931) 464–475.
[44] D. Spitzer, J.J. Ten Bosch, A simple method for determination of the reflection coefficient at the internal surfaces of turbid slabs, Opt. Commun. 9 (3) (1973) 311–314.

[45] A. Roos, C.G. Ribbing, M. Bergkvist, Anomalies in integrating sphere measurements on structured samples, Appl. Opt. 27 (18) (1988) 3828–3832.
[46] R.T. Conley, Infrared Spectroscopy, second ed., Allyn and Bacon Inc., Boston, 1972.
[47] W.E. Vargas, G.A. Niklasson, Forward-scattering ratios and average pathlength parameter in radiative transfer models, J. Phys: Condens. Matter 9 (1997) 9083–9096.
[48] M.Y. Choi, G.W. Mulholland, A. Hamins, T. Kashiwagi, Comparisons of the soot volume fraction using gravimetric and light extinction techniques, Combust. Flame 102 (1995) 161–169.

Available online at www.sciencedirect.com
SCIENCE DIRECT®
Solar Energy Materials & Solar Cells
ELSEVIER
Solar Energy Materials & Solar Cells 89 (2005) 351–389
www.elsevier.com/locate/solmat

Solar spectral optical properties of pigments—Part II: survey of common colorants

Ronnen Levinson*, Paul Berdahl, Hashem Akbari

Lawrence Berkeley National Laboratory, 1 Cyclotron Road, Berkeley, CA 94720, USA

Received 15 June 2004; received in revised form 5 November 2004; accepted 12 November 2004
Available online 11 March 2005

Abstract

Various pigments are characterized by determination of parameters S (backscattering) and K (absorption) as functions of wavelength in the solar spectral range of 300–2500 nm. Measured values of S for generic titanium dioxide (rutile) white pigment are in rough agreement with values computed from the Mie theory, supplemented by a simple multiple scattering model. Pigments in widespread use are examined, with particular emphasis on those that may be useful for formulating non-white materials that can reflect the near-infrared (NIR) portion of sunlight, such as the complex inorganic color pigments (mixed metal oxides). These materials remain cooler in sunlight than comparable NIR-absorbing colors. NIR-absorptive pigments are to be avoided. High NIR reflectance can be produced by a reflective metal substrate, an NIR-reflective underlayer, and/or by the use of a pigment that scatters strongly in the NIR.
Published by Elsevier B.V.

Keywords: Pigment characterization; Solar spectral optical properties; Kubelka-Munk absorption and backscattering coefficients; Cool roofs; Titanium dioxide

*Corresponding author. Tel.: +1 510 486 7494; fax: +1 425 955 1992.
E-mail addresses: RMLevinson@LBL.gov (R. Levinson), PHBerdahl@LBL.gov (P. Berdahl), H_Akbari@LBL.gov (H. Akbari).

0927-0248/$ - see front matter Published by Elsevier B.V.
doi:10.1016/j.solmat.2004.11.013

1. Introduction

A companion article [1] presented a theoretical framework and experimental procedure that can be used to determine the Kubelka–Munk backscattering and absorption coefficients of a pigmented film. The current article applies this model to each of 87 predominantly single-pigment films, with special attention paid to characterizing the near-infrared (NIR) properties that determine whether a pigment is "hot" or "cool." These pigments include (but are not limited to) inorganic colorants conventionally used for architectural purposes, such as titanium dioxide white and iron oxide black; spectrally selective organics, such as dioxazine purple; and spectrally selective inorganics developed for cool applications, such as selective blacks that are mixed oxides of chromium and iron.

Several pigment handbooks [2–6] provide valuable supplemental information on the properties, synthesis methods, and applications of many of the pigments characterized in this study. Naturally, as far as optical properties are concerned, these references provide data mainly in the visible spectral range (an exception is [5]).

2. Pigment classification

For convenience in presentation, the pigments were grouped by color "family" (e.g., green) and then categorized by chemistry (e.g., chromium oxide green). Some families span two colors (e.g., black/brown) because it is difficult to consistently identify color based on pigment name and color index (convention for identifying colorants [7]). For example, a dark pigment may be marketed as "black," but carry a "pigment brown" color index designation and exhibit red tones more characteristic of brown than of black. The following list shows in parentheses a mnemonic single-letter abbreviation assigned to each color family, and in braces the population of each color family and pigment category. Pigment categories are presented in the order of simpler inorganics, more complex inorganics, and then finally organics. Each member of a color family is assigned an identification code X*nn*, where X is the color family abbreviation and *nn* is a serial number. For example, the 11 members of the green color family ("G") have identification codes G01 through G11. The same pigment may be present in more than one pigmented film. For example, our survey includes four titanium dioxide white films (W01–W04). However, the concentration of pigment, pigment particle size, and/or source of the pigment (manufacturer) may vary from film to film.

1. White (W) {4}
   (a) titanium dioxide white {4}.
2. Black/brown (B) {21}
   (a) carbon black {2},
   (b) other non-selective black {2},
   (c) chromium iron oxide selective black {7},
   (d) other selective black {1},

(e) iron oxide brown {3},
(f) other brown {6}.

3. Blue/purple (U) {14}
   (a) cobalt aluminate blue {4},
   (b) cobalt chromite blue {5},
   (c) iron blue {1},
   (d) ultramarine blue {1},
   (e) phthalocyanine blue {2},
   (f) dioxazine purple {1}.
4. Green (G) {11}
   (a) chromium oxide green {2},
   (b) modified chromium oxide green {1},
   (c) cobalt chromite green {3},
   (d) cobalt titanate green {3},
   (e) phthalocyanine green {2}.
5. Red/orange (R) {9}
   (a) iron oxide red {4},
   (b) cadmium orange {1},
   (c) organic red {4}.
6. Yellow (Y) {14}
   (a) iron oxide yellow {1},
   (b) cadmium yellow {1},
   (c) chrome yellow {1},
   (d) chrome titanate yellow {4},
   (e) nickel titanate yellow {4},
   (f) strontium chromate yellow + titanium dioxide {1},
   (g) Hansa yellow {1},
   (h) diarylide yellow {1}.
7. Pearlescent (P) {14}
   (a) mica + titanium dioxide {9},
   (b) mica + titanium dioxide + iron oxide {5}.

3. Pigment properties by color and category

Table 1 summarizes some relevant bulk properties of the pigmented films in each category, such as NIR reflectances over black and white backgrounds. The measured and computed spectral properties of each pigmented film are shown in Fig. 1. Each film has a column of charts of the type presented in the companion article [1] with the omission of the chart of ancillary parameters (diffuse fractions and interface reflectances). Color images of the films are shown in Fig. 2.

When examining spectral optical properties, it is worth noting that most of the NIR radiation in sunlight arrives at the shorter NIR wavelengths. Of the 52% of solar energy delivered in the NIR spectrum (700–2500 nm), 50% lies within

Table 1
Ranges of NIR reflectance over white (ROW_{nir}), NIR reflectance over black (ROB_{nir}), visible transmittance (T_{vis}), and thickness (δ) measured for pigmented films in each pigment category

Category	ROW_{nir}	ROB_{nir}	T_{vis}	δ (μm)	Film Codes
Titanium dioxide white	0.87–0.88	0.24–0.65	0.10-0.42	17–29	W01-W04
Carbon black	0.05–0.06	0.04–0.04	0.03–0.07	16–19	B01–B02
Other non-selective black	0.04–0.05	0.04–0.05	0.00–0.07	20–24	B03–B04
Chromium iron oxide selective black	0.23–0.48	0.11–0.35	0.00–0.15	19–26	B05–B11
Organic selective black	0.85	0.10	0.01	23	B12
Iron oxide brown	0.47–0.61	0.06–0.27	0.03–0.24	14–26	B13–B15
Other brown	0.50–0.74	0.22–0.40	0.01–0.24	17–28	B16–B21
Cobalt aluminate blue	0.62–0.71	0.09–0.20	0.16–0.28	16–23	U01–U05
Cobalt chromite blue	0.55–0.70	0.10–0.25	0.05–0.28	16–26	U06–U09
Iron blue	0.25	0.05	0.27	12	U10
Ultramarine blue	0.52	0.05	0.20	23	U11
Phthalocyanine blue	0.55–0.63	0.06–0.08	0.21–0.22	14–26	U12–U13
Dioxazine purple	0.82	0.05	0.21	10	U14
Chromium oxide green	0.50–0.57	0.33–0.40	0.00–0.01	12–26	G01–G02
Modified chromium oxide green	0.71	0.22	0.22	23	G03
Cobalt chromite green	0.58–0.64	0.14–0.18	0.17–0.28	13–23	G04–G06
Cobalt titanate green	0.37–0.73	0.21–0.30	0.04–0.22	10–24	G07–G09
Phthalocyanine green	0.42–0.45	0.06–0.07	0.10–0.20	13–25	G10–G11
Iron oxide red	0.31–0.67	0.19–0.38	0.00–0.08	13–26	R01–R04
Cadmium orange	0.87	0.26	0.18	10	R05
Organic red	0.83–0.87	0.06–0.14	0.15–0.32	11–27	R06–R09
Iron oxide yellow	0.70	0.21	0.16	19	Y01
Cadmium yellow	0.87	0.29	0.25	11	Y02
Chrome yellow	0.83	0.34	0.18	24	Y03
Chrome titanate yellow	0.80–0.86	0.26–0.62	0.05–0.23	17–26	Y04–Y07
Nickel titanate yellow	0.77–0.87	0.22–0.64	0.09–0.51	17–27	Y08–Y11
Strontium chromate yellow + titanium dioxide	0.86	0.38	0.21	19	Y12
Hansa yellow	0.87	0.06	0.43	11	Y13
Diarylide yellow	0.87	0.08	0.35	12	Y14
Mica + titanium dioxide	0.88–0.90	0.35–0.54	0.31–0.54	17–37	P01–P09
Mica + titanium dioxide + iron oxide	0.27–0.85	0.25–0.44	0.02–0.42	20–24	P10–P14

700–1000 nm; 30% lies within 1000–1500 nm; and 20% lies within 1500–2500 nm (Fig. 3). We refer to the 700–1000 nm region containing half the NIR solar energy (and a quarter of the total solar energy) as the "short" NIR.

In the discussions below, black and white *backgrounds* are assumed to be opaque, with observed NIR reflectances of 0.04 and 0.87, respectively. Note that in the absence of the air-film interface, the continuous refractive index (CRI) NIR reflectances of the black and white backgrounds are 0.00 and 0.94, respectively.

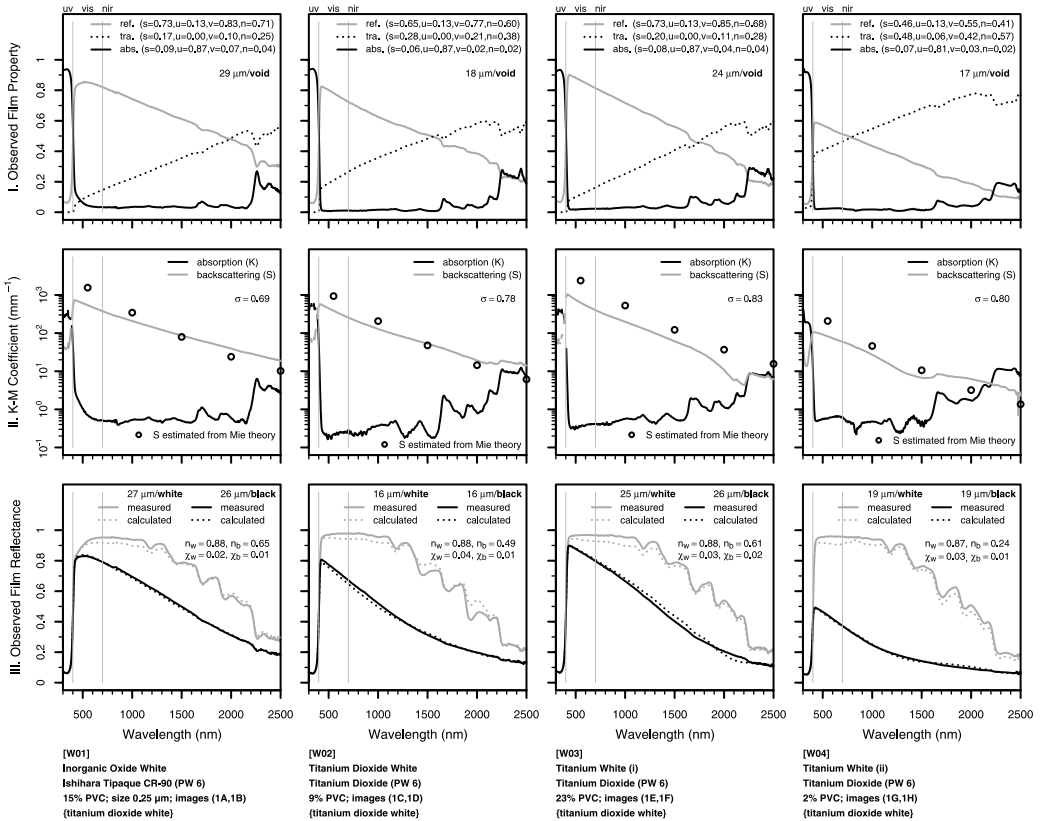

Fig. 1. (i/xxii) Measurements and model calculations for 87 predominately single-pigment films. Shown from top to bottom are (I) measured reflectance, transmittance, and absorptance of film with void background; (II) Kubelka–Munk backscattering and absorption coefficients S and K, and non-spectral forward scattering ratio σ; and (III) measured and computed film reflectances over white [w] and black [b] backgrounds, along with measured NIR reflectance n and RMS error χ. Also listed are pigment identification code; paint name; pigment name; PVC; pigment particle size, if known; and location of images in Fig. 2.

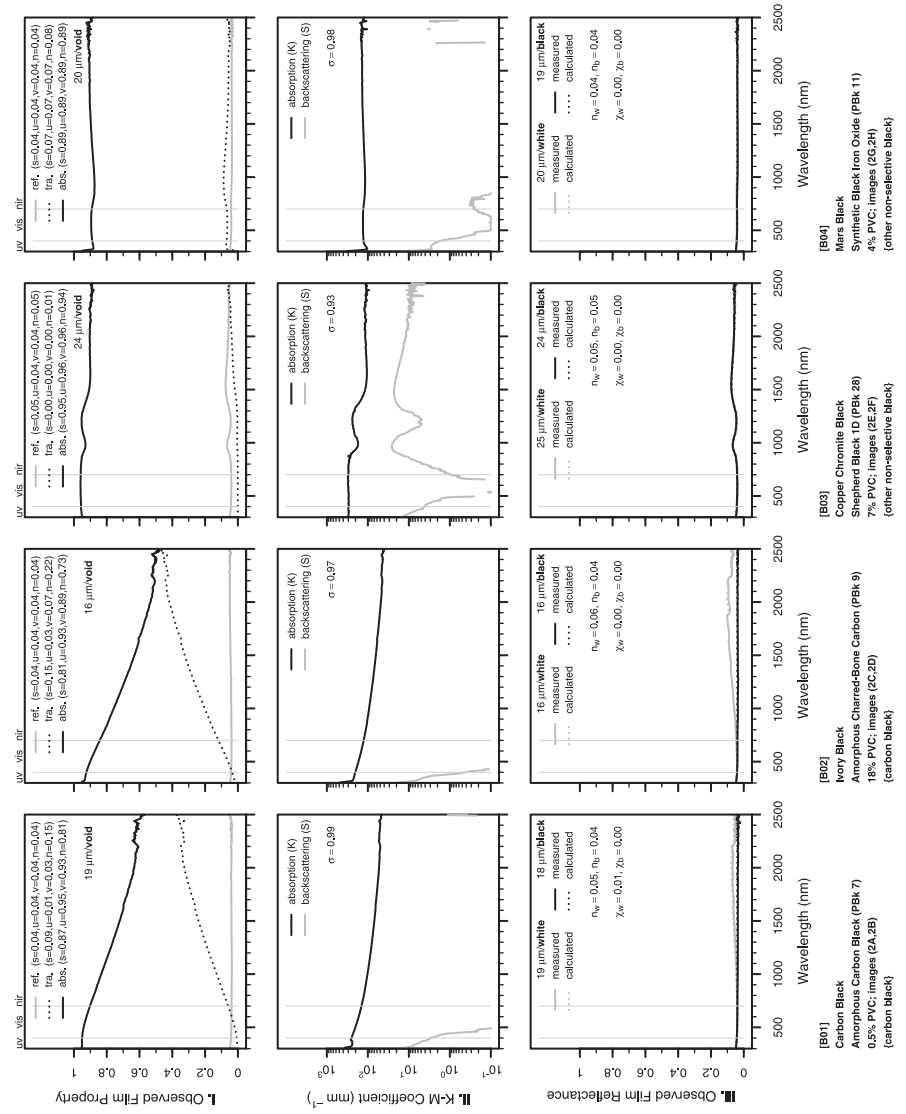
I. Observed Film Property
II. K-M Coefficient (mm⁻¹)
III. Observed Film Reflectance
Wavelength (nm)
[B01] Carbon Black
Amorphous Carbon Black (PBk 7)
0.5% PVC; images (2A,2B)
(carbon black)
[B02] Ivory Black
Amorphous Charred-Bone Carbon (PBk 9)
18% PVC; images (2C,2D)
(carbon black)
[B03] Copper Chromite Black
Shepherd Black 1D (PBk 28)
7% PVC; images (2E,2F)
(other non-selective black)
[B04] Mars Black
Synthetic Black Iron Oxide (PBk 11)
4% PVC; images (2G,2H)
(other non-selective black)

Fig. 1. (ii/xxii)

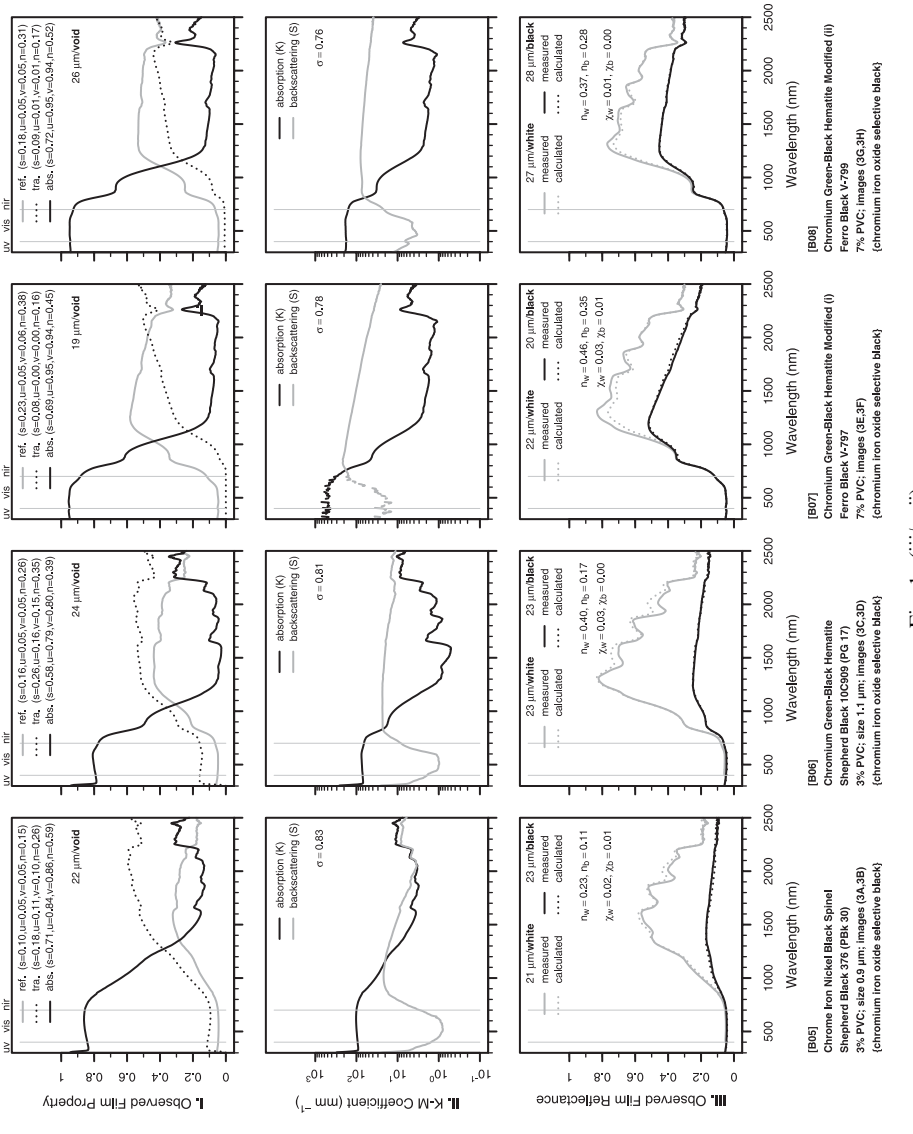

Fig. 1. (iii/xxii)

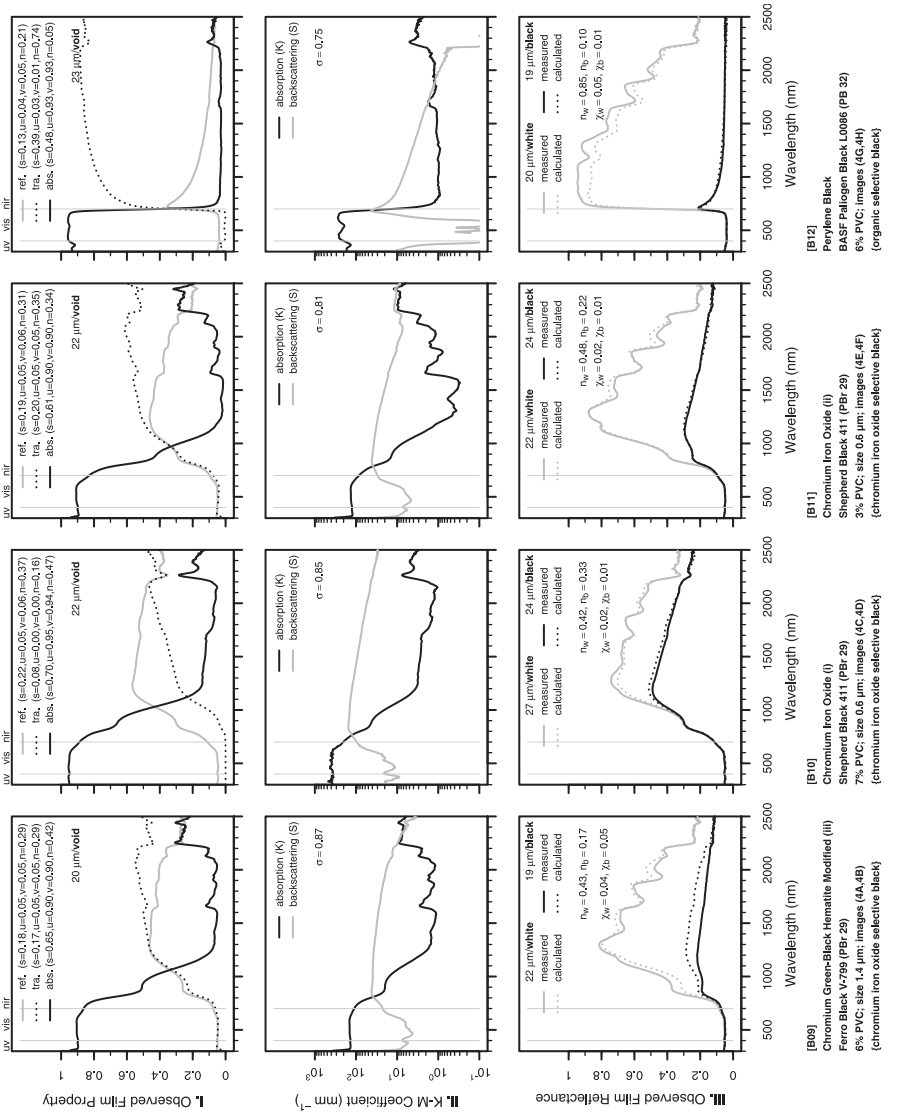
I. Observed Film Property
II. K-M Coefficient (mm⁻¹)
III. Observed Film Reflectance
uv vis nir
ref. (s=0.18,μ=0.05,ν=0.05,π=0.29)
trns. (s=0.17,μ=0.05,ν=0.05,π=0.29)
abs. (s=0.65,μ=0.90,ν=0.90,π=0.42)
20 μm/void
ref. (s=0.22,μ=0.05,ν=0.06,π=0.37)
trns. (s=0.08,μ=0.05,ν=0.00,π=0.16)
abs. (s=0.70,μ=0.95,ν=0.94,π=0.47)
22 μm/void
ref. (s=0.19,μ=0.05,ν=0.06,π=0.31)
trns. (s=0.20,μ=0.05,ν=0.05,π=0.35)
abs. (s=0.61,μ=0.90,ν=0.90,π=0.34)
22 μm/void
ref. (s=0.13,μ=0.04,ν=0.05,π=0.21)
trns. (s=0.39,μ=0.03,ν=0.01,π=0.74)
abs. (s=0.48,μ=0.93,ν=0.93,π=0.05)
23 μm/void
absorption (K)
backscattering (S)
σ = 0.87
σ = 0.85
σ = 0.81
σ = 0.75
22 μm/white
19 μm/black
measured
calculated
nW = 0.43, nb = 0.17
χW = 0.04, χb = 0.05
27 μm/white
24 μm/black
nW = 0.42, nb = 0.33
χW = 0.02, χb = 0.01
22 μm/white
24 μm/black
nW = 0.48, nb = 0.22
χW = 0.02, χb = 0.01
20 μm/white
19 μm/black
nW = 0.85, nb = 0.10
χW = 0.05, χb = 0.01
Wavelength (nm)
[B09]
Chromium Green-Black Hematite Modified (iii)
Ferro Black V-799 (PBr 29)
6% PVC; size 1.4 μm: images (4A,4B)
(chromium iron oxide selective black)
[B10]
Chromium Iron Oxide (i)
Shepherd Black 411 (PBr 29)
7% PVC; size 0.6 μm: images (4C,4D)
(chromium iron oxide selective black)
[B11]
Chromium Iron Oxide (ii)
Shepherd Black 411 (PBr 29)
3% PVC; size 0.6 μm: images (4E,4F)
(chromium iron oxide selective black)
[B12]
Perylene Black
BASF Fallogen Black L0086 (PB 32)
6% PVC: images (4G,4H)
(organic selective black)

Fig. 1. (iv/xxii)

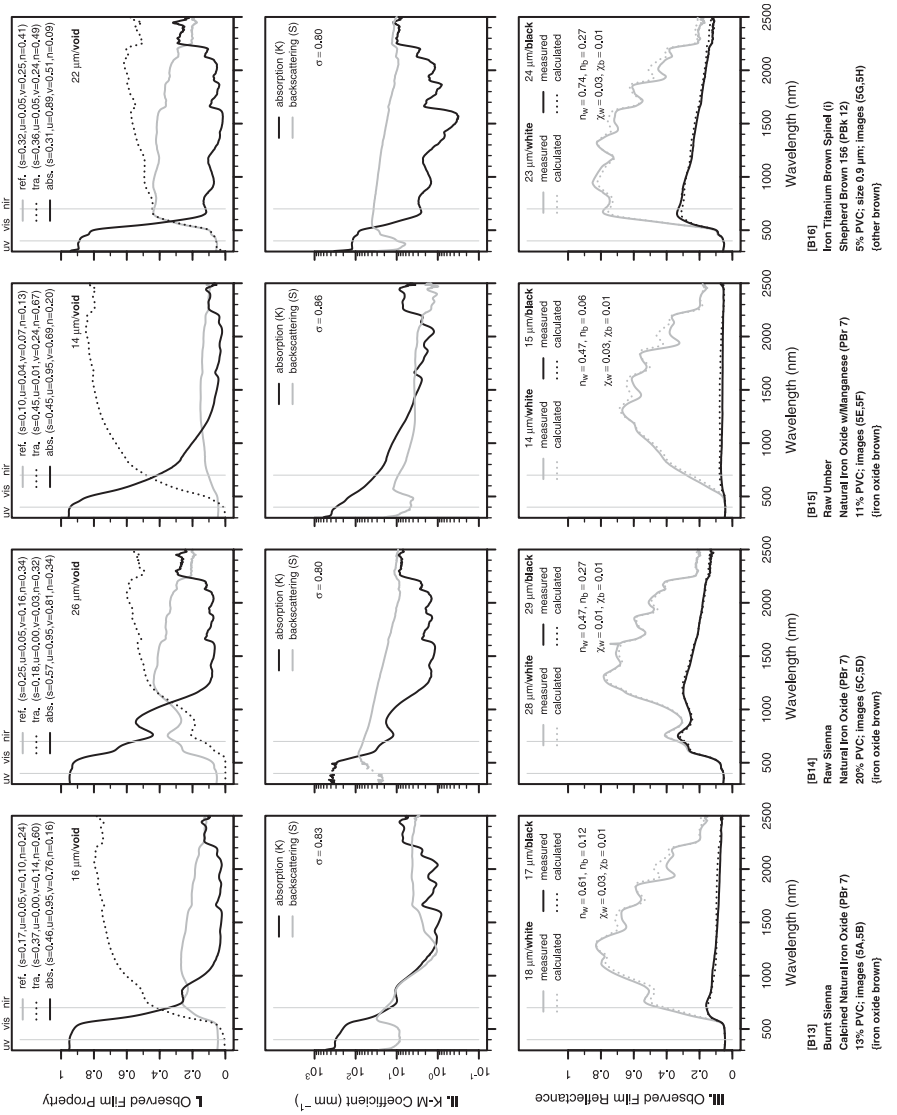
I. Observed Film Property
II. K-M Coefficient (mm⁻¹)
III. Observed Film Reflectance
uv vis nir
ref. (s=0.17,μ=0.05,v=0.10,n=0.24)
tra. (s=0.37,μ=0.00,v=0.14,n=0.60)
abs. (s=0.46,μ=0.95,v=0.76,n=0.16)
16 μm/void
ref. (s=0.25,μ=0.05,v=0.16,n=0.34)
tra. (s=0.18,μ=0.00,v=0.03,n=0.32)
abs. (s=0.57,μ=0.95,v=0.81,n=0.34)
26 μm/void
ref. (s=0.10,μ=0.04,v=0.07,n=0.13)
tra. (s=0.45,μ=0.01,v=0.24,n=0.67)
abs. (s=0.45,μ=0.95,v=0.69,n=0.20)
14 μm/void
ref. (s=0.32,μ=0.05,v=0.25,n=0.41)
tra. (s=0.36,μ=0.05,v=0.24,n=0.49)
abs. (s=0.31,μ=0.89,v=0.51,n=0.09)
22 μm/void
absorption (K)
backscattering (S)
σ = 0.83
σ = 0.80
σ = 0.86
σ = 0.80
18 μm/white
17 μm/black
28 μm/white
29 μm/black
14 μm/white
15 μm/black
23 μm/white
24 μm/black
measured
calculated
nw = 0.61 , nb = 0.12
χw = 0.03, χb = 0.01
nw = 0.47 , nb = 0.27
χw = 0.01, χb = 0.01
nw = 0.47 , nb = 0.06
χw = 0.03, χb = 0.01
nw = 0.74 , nb = 0.27
χw = 0.03, χb = 0.01
Wavelength (nm)
[B13]
Burnt Sienna
Calcined Natural Iron Oxide (PBr 7)
13% PVC; images (5A,5B)
{iron oxide brown}
[B14]
Raw Sienna
Natural Iron Oxide (PBr 7)
20% PVC; images (5C,5D)
{iron oxide brown}
[B15]
Raw Umber
Natural Iron Oxide w/Manganese (PBr 7)
11% PVC; images (5E,5F)
{iron oxide brown}
[B16]
Iron Titanium Brown Spinel (i)
Shepherd Brown 156 (PBk 12)
5% PVC; size 0.9 μm; images (5G,5H)
{other brown}

Fig. 1. (v/xxii)

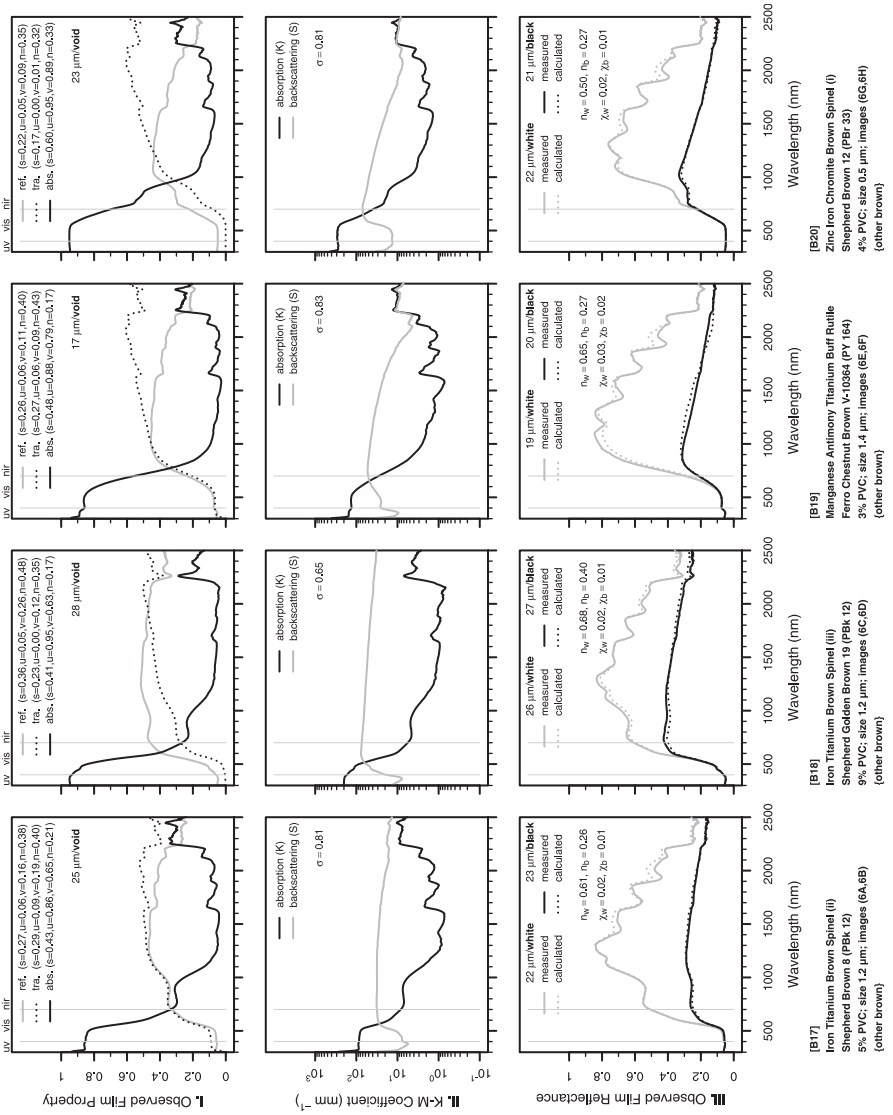
I. Observed Film Property
II. K-M Coefficient (mm⁻¹)
III. Observed Film Reflectance
uv vis nir
ref. (s=0.27,μ=0.06,γ=0.16,η=0.38)
trn. (s=0.29,μ=0.06,γ=0.19,η=0.40)
abs. (s=0.43,μ=0.86,γ=0.65,η=0.21)
25 μm/void
ref. (s=0.36,μ=0.05,γ=0.26,η=0.48)
trn. (s=0.23,μ=0.00,γ=0.12,η=0.35)
abs. (s=0.41,μ=0.95,γ=0.63,η=0.17)
28 μm/void
ref. (s=0.26,μ=0.06,γ=0.11,η=0.40)
trn. (s=0.27,μ=0.06,γ=0.09,η=0.49)
abs. (s=0.48,μ=0.88,γ=0.79,η=0.17)
17 μm/void
ref. (s=0.22,μ=0.05,γ=0.09,η=0.35)
trn. (s=0.17,μ=0.00,γ=0.01,η=0.32)
abs. (s=0.60,μ=0.95,γ=0.89,η=0.33)
23 μm/void
absorption (K)
backscattering (S)
σ = 0.81
σ = 0.85
σ = 0.83
σ = 0.81
22 μm/white
23 μm/black
26 μm/white
27 μm/black
19 μm/white
20 μm/black
22 μm/white
21 μm/black
measured
calculated
nW = 0.61, nb = 0.26
χW = 0.02, χb = 0.01
nW = 0.68, nb = 0.40
χW = 0.02, χb = 0.01
nW = 0.65, nb = 0.27
χW = 0.03, χb = 0.02
nW = 0.50, nb = 0.27
χW = 0.02, χb = 0.01
Wavelength (nm)
[B17]
Iron Titanium Brown Spinel (ii)
Shepherd Brown 8 (PBk 12)
5%; PVC; size 1.2 μm; images (6A,6B)
(other brown)
[B18]
Iron Titanium Brown Spinel (iii)
Shepherd Golden Brown 19 (PBk 12)
9%; PVC; size 1.2 μm; images (6C,6D)
(other brown)
[B19]
Manganese Antimony Titanium Buff Rutile
Ferro Chestnut Brown V-10364 (PY 164)
3%; PVC; size 1.4 μm; images (6E,6F)
(other brown)
[B20]
Zinc Iron Chromite Brown Spinel (i)
Shepherd Brown 12 (PBr 33)
4% PVC; size 0.5 μm; images (6G,6H)
(other brown)

Fig. 1. (vi/xxii)

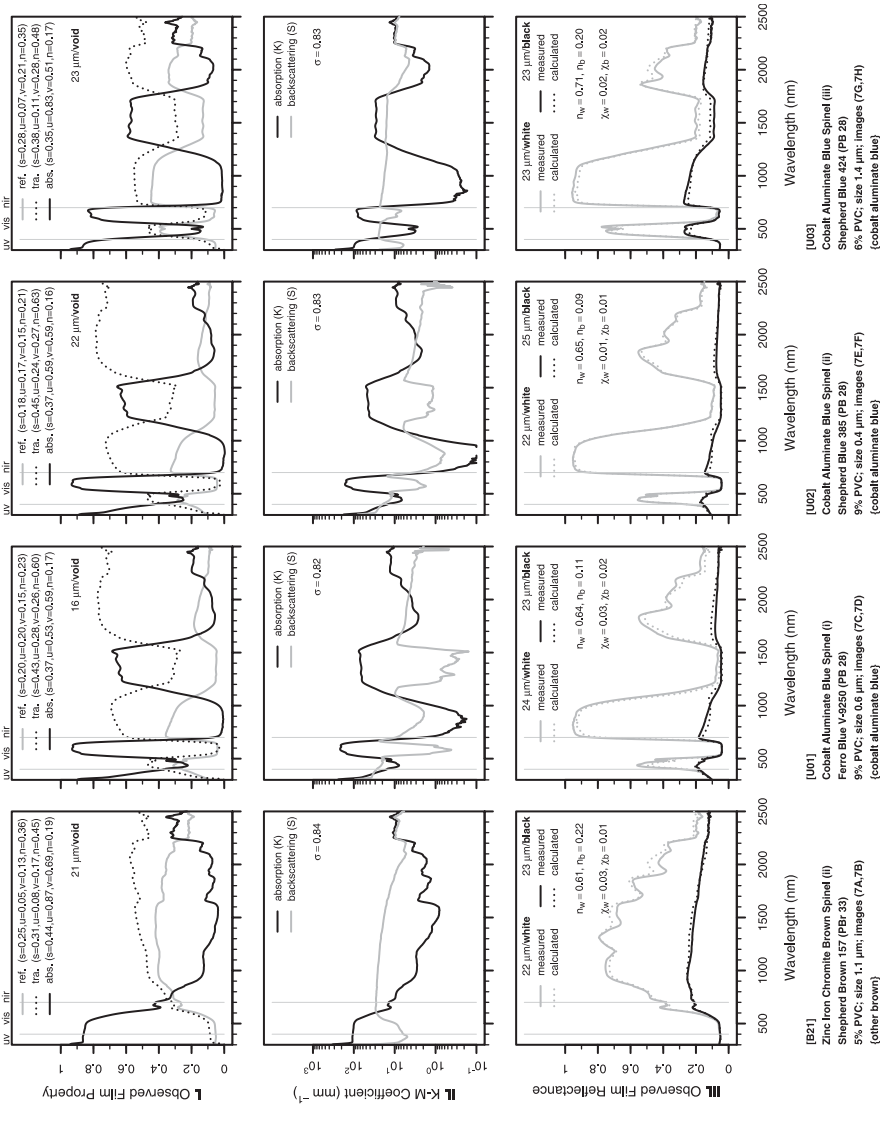

Fig. 1. (vii/xxii)

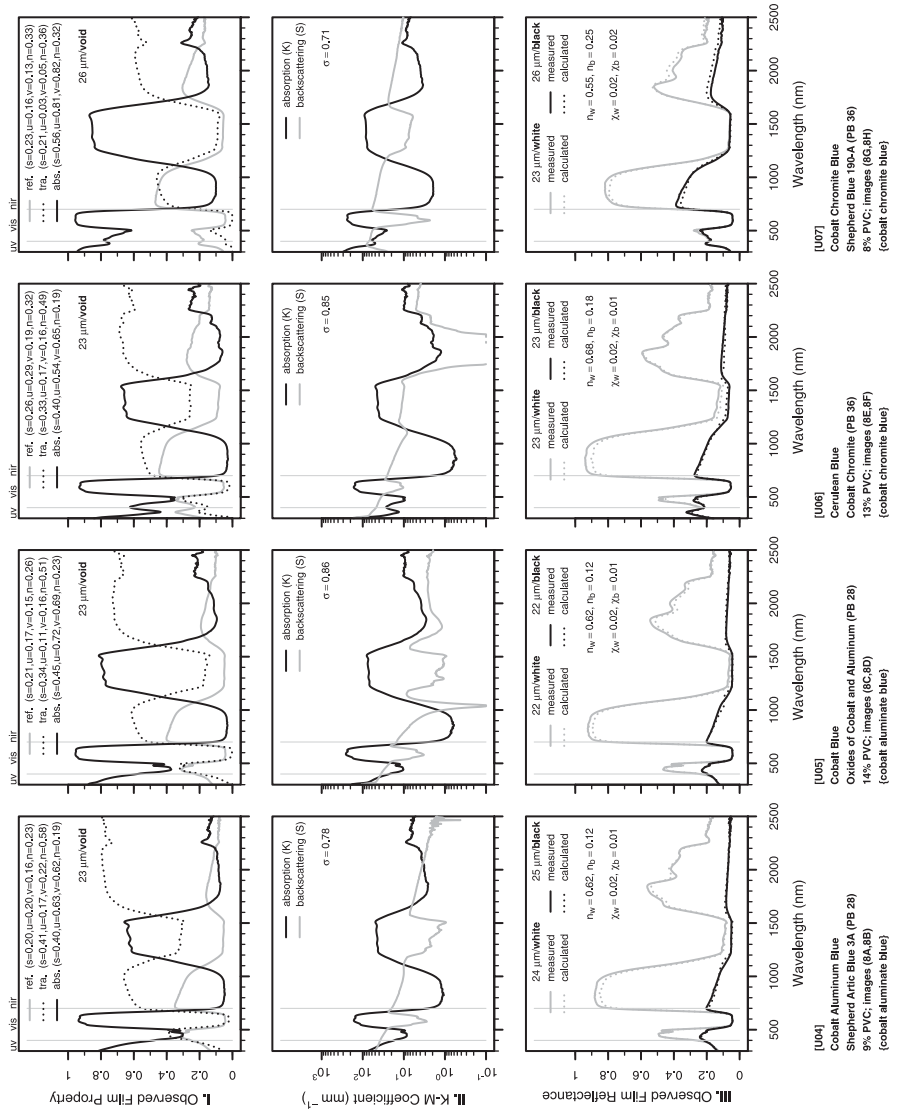

Fig. 1. (viii/xxii)

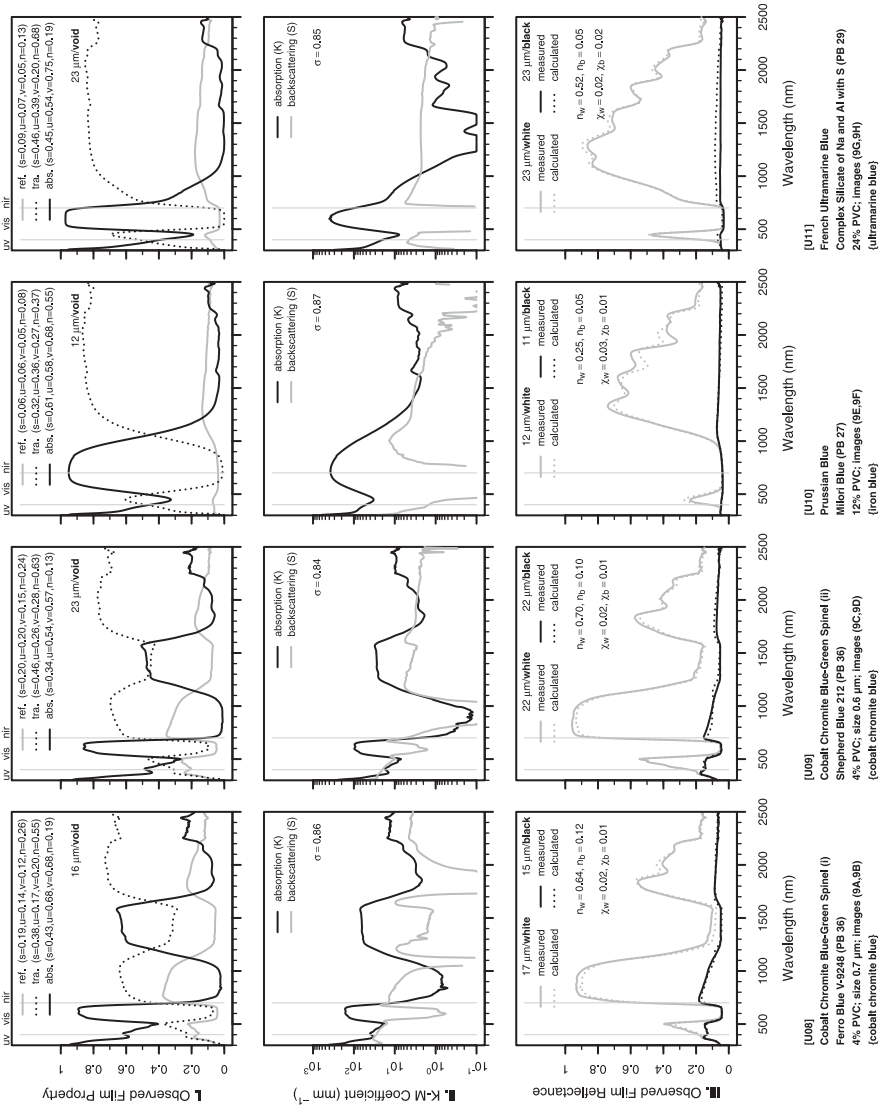
uv vis nir
ref. (s=0.19,μ=0.14,v=0.12,n=0.26)
tra. (s=0.38,μ=0.17,v=0.20,n=0.55)
abs. (s=0.43,μ=0.68,v=0.68,n=0.19)
16 μm/void
ref. (s=0.20,μ=0.20,v=0.15,n=0.24)
tra. (s=0.46,μ=0.26,v=0.28,n=0.63)
abs. (s=0.34,μ=0.54,v=0.57,n=0.13)
23 μm/void
ref. (s=0.06,μ=0.06,v=0.05,n=0.08)
tra. (s=0.22,μ=0.36,v=0.27,n=0.37)
abs. (s=0.61,μ=0.58,v=0.68,n=0.55)
12 μm/void
ref. (s=0.09,μ=0.07,v=0.05,n=0.13)
tra. (s=0.46,μ=0.39,v=0.20,n=0.68)
abs. (s=0.45,μ=0.54,v=0.75,n=0.19)
23 μm/void
I. Observed Film Property
absorption (K)
backscattering (S)
σ = 0.86
σ = 0.84
σ = 0.87
σ = 0.85
II. K-M Coefficient (mm⁻¹)
17 μm/white
15 μm/black
measured
calculated
$n_W = 0.64$, $n_B = 0.12$
$\chi_W = 0.02$, $\chi_B = 0.01$
22 μm/white
22 μm/black
$n_W = 0.70$, $n_B = 0.10$
$\chi_W = 0.02$, $\chi_B = 0.01$
12 μm/white
11 μm/black
$n_W = 0.25$, $n_B = 0.05$
$\chi_W = 0.03$, $\chi_B = 0.01$
23 μm/white
23 μm/black
$n_W = 0.52$, $n_B = 0.05$
$\chi_W = 0.02$, $\chi_B = 0.02$
III. Observed Film Reflectance
Wavelength (nm)
[U08]
Cobalt Chromite Blue-Green Spinel (i)
Ferro Blue V-9248 (PB 36)
4% PVC; size 0.7 μm; images (9A,9B)
{cobalt chromite blue}
[U09]
Cobalt Chromite Blue-Green Spinel (ii)
Shepherd Blue 212 (PB 36)
4% PVC; size 0.6 μm; images (9C,9D)
{cobalt chromite blue}
[U10]
Prussian Blue
Milori Blue (PB 27)
12% PVC; images (9E,9F)
{iron blue}
[U11]
French Ultramarine Blue
Complex Silicate of Na and Al with S (PB 29)
24% PVC; images (9G,9H)
{ultramarine blue}

Fig. 1. (ix/xxii)

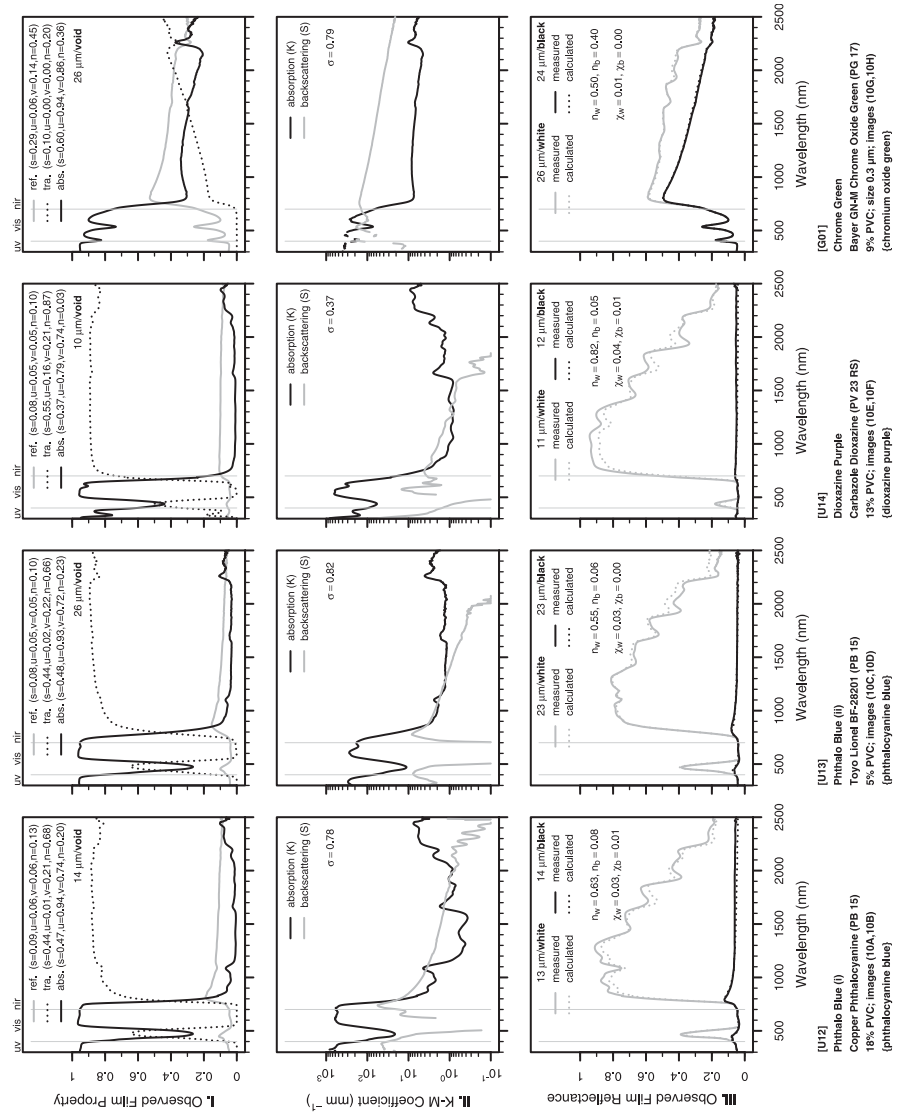
I. Observed Film Property
II. K-M Coefficient (mm⁻¹)
III. Observed Film Reflectance
Wavelength (nm)
uv vis nir
ref. (s=0.09,μ=0.06,γ=0.06,η=0.13)
trn. (s=0.44,μ=0.01,γ=0.27,η=0.66)
abs. (s=0.47,μ=0.94,γ=0.74,η=0.20)
14 μm/void
13 μm/white
14 μm/black
measured
calculated
nW = 0.63, nb = 0.08
χW = 0.03, χb = 0.01
absorption (K)
backscattering (S)
σ = 0.78
[U12]
Phthalo Blue (i)
Copper Phthalocyanine (PB 15)
18% PVC; images (10A,10B)
{phthalocyanine blue}
ref. (s=0.08,μ=0.05,γ=0.05,η=0.10)
trn. (s=0.44,μ=0.02,γ=0.22,η=0.66)
abs. (s=0.48,μ=0.93,γ=0.72,η=0.23)
26 μm/void
23 μm/white
23 μm/black
nW = 0.55, nb = 0.06
χW = 0.03, χb = 0.00
σ = 0.82
[U13]
Phthalo Blue (ii)
Toyo Lionel BF-28201 (PB 15)
5% PVC; images (10C,10D)
{phthalocyanine blue}
ref. (s=0.08,μ=0.05,γ=0.05,η=0.10)
trn. (s=0.55,μ=0.15,γ=0.21,η=0.87)
abs. (s=0.37,μ=0.79,γ=0.74,η=0.03)
10 μm/void
11 μm/white
12 μm/black
nW = 0.82, nb = 0.05
χW = 0.04, χb = 0.01
σ = 0.37
[U14]
Dioxazine Purple
Carbazole Dioxazine (PV 23 RS)
13% PVC; images (10E,10F)
{dioxazine purple}
ref. (s=0.29,μ=0.06,γ=0.14,η=0.45)
trn. (s=0.10,μ=0.00,γ=0.00,η=0.20)
abs. (s=0.60,μ=0.94,γ=0.86,η=0.36)
26 μm/void
26 μm/white
24 μm/black
nW = 0.50, nb = 0.40
χW = 0.01, χb = 0.00
σ = 0.79
[G01]
Chrome Green
Bayer GN-M Chrome Oxide Green (PG 17)
9% PVC; size 0.3 μm; images (10G,10H)
{chromium oxide green}

Fig. 1. (x/xxii)

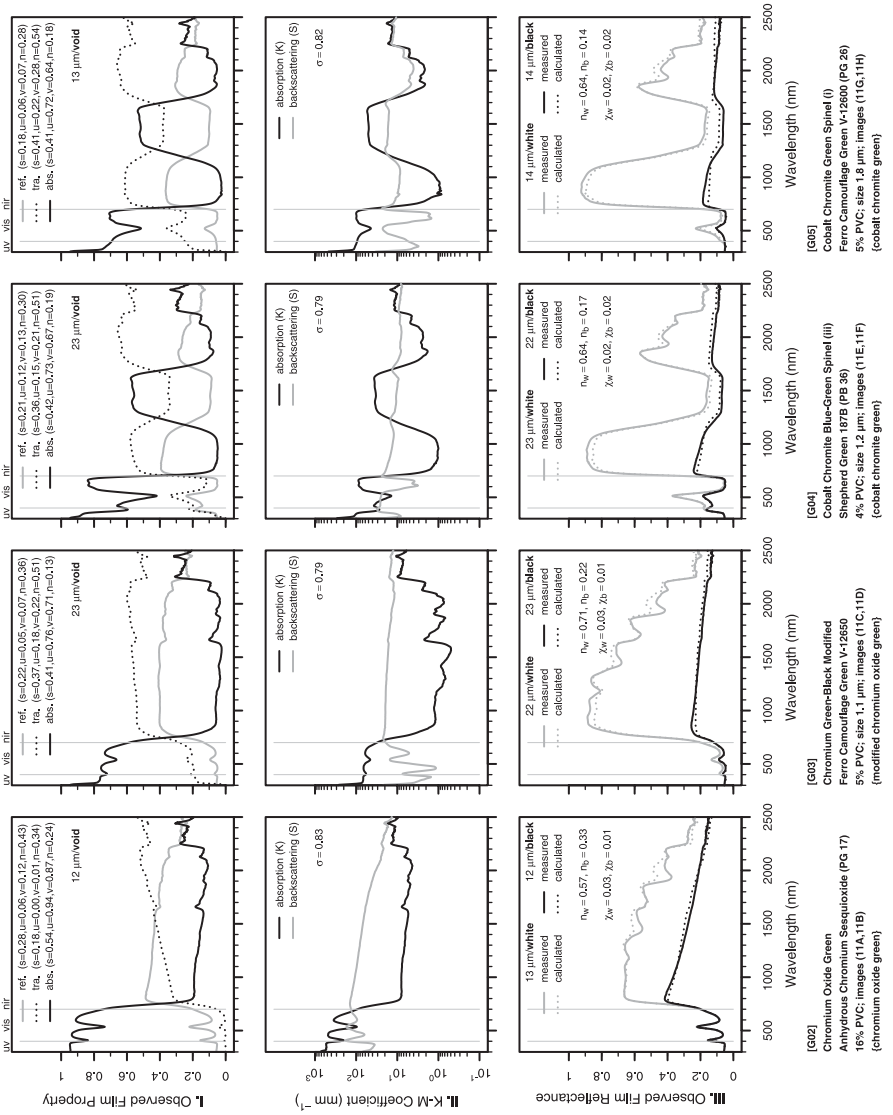
I. Observed Film Property
II. K-M Coefficient (mm⁻¹)
III. Observed Film Reflectance
uv vis nir
ref. (s=0.28,μ=0.06,ν=0.12,π=0.43)
trns. (s=0.18,μ=0.06,ν=0.01,π=0.34)
abs. (s=0.54,μ=0.94,ν=0.87,π=0.24)
12 μm/void
ref. (s=0.22,μ=0.05,ν=0.07,π=0.36)
trns. (s=0.37,μ=0.18,ν=0.22,π=0.51)
abs. (s=0.41,μ=0.76,ν=0.71,π=0.13)
23 μm/void
ref. (s=0.21,μ=0.12,ν=0.13,π=0.30)
trns. (s=0.36,μ=0.15,ν=0.21,π=0.51)
abs. (s=0.42,μ=0.73,ν=0.67,π=0.19)
23 μm/void
ref. (s=0.18,μ=0.06,ν=0.07,π=0.28)
trns. (s=0.41,μ=0.22,ν=0.28,π=0.54)
abs. (s=0.41,μ=0.72,ν=0.64,π=0.18)
13 μm/void
absorption (K)
backscattering (S)
σ = 0.83
σ = 0.79
σ = 0.79
σ = 0.82
13 μm/white
12 μm/black
measured
calculated
n_W = 0.57, n_B = 0.33
χ_W = 0.03, χ_B = 0.01
22 μm/white
23 μm/black
n_W = 0.71, n_B = 0.22
χ_W = 0.03, χ_B = 0.01
23 μm/white
22 μm/black
n_W = 0.64, n_B = 0.17
χ_W = 0.02, χ_B = 0.02
14 μm/white
14 μm/black
n_W = 0.64, n_B = 0.14
χ_W = 0.02, χ_B = 0.02
Wavelength (nm)
[G02]
Chromium Oxide Green
Anhydrous Chromium Sesquioxide (PG 17)
16% PVC; images (11A,11B)
(chromium oxide green)
[G03]
Chromium Green-Black Modified
Ferro Camouflage Green V-12650
5% PVC; size 1.1 μm; images (11C,11D)
(modified chromium oxide green)
[G04]
Cobalt Chromite Blue-Green Spinel (iii)
Shepherd Green 187B (PB 36)
4% PVC; size 1.2 μm; images (11E,11F)
(cobalt chromite green)
[G05]
Cobalt Chromite Green Spinel (i)
Ferro Camouflage Green V-12600 (PG 26)
5% PVC; size 1.8 μm; images (11G,11H)
(cobalt chromite green)

Fig. 1. (xi/xxii)

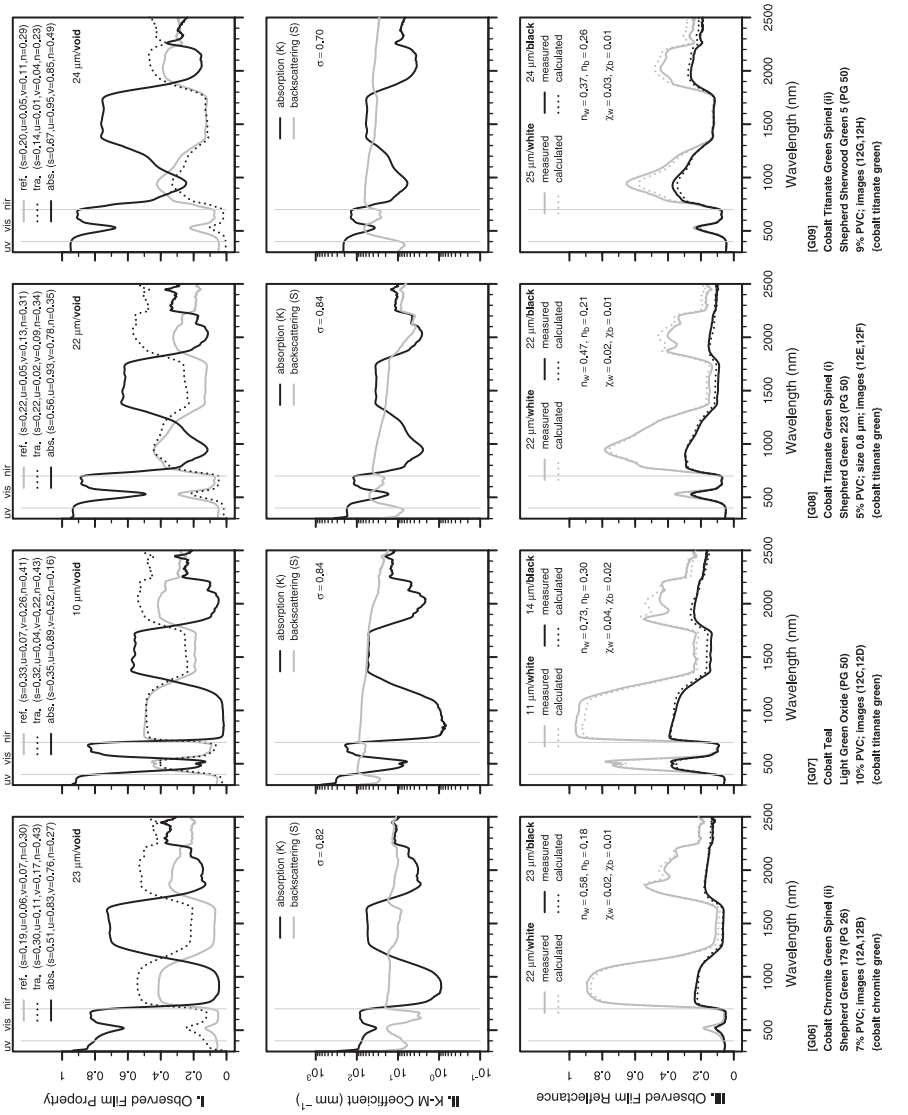

Fig. 1. (xii/xxii)

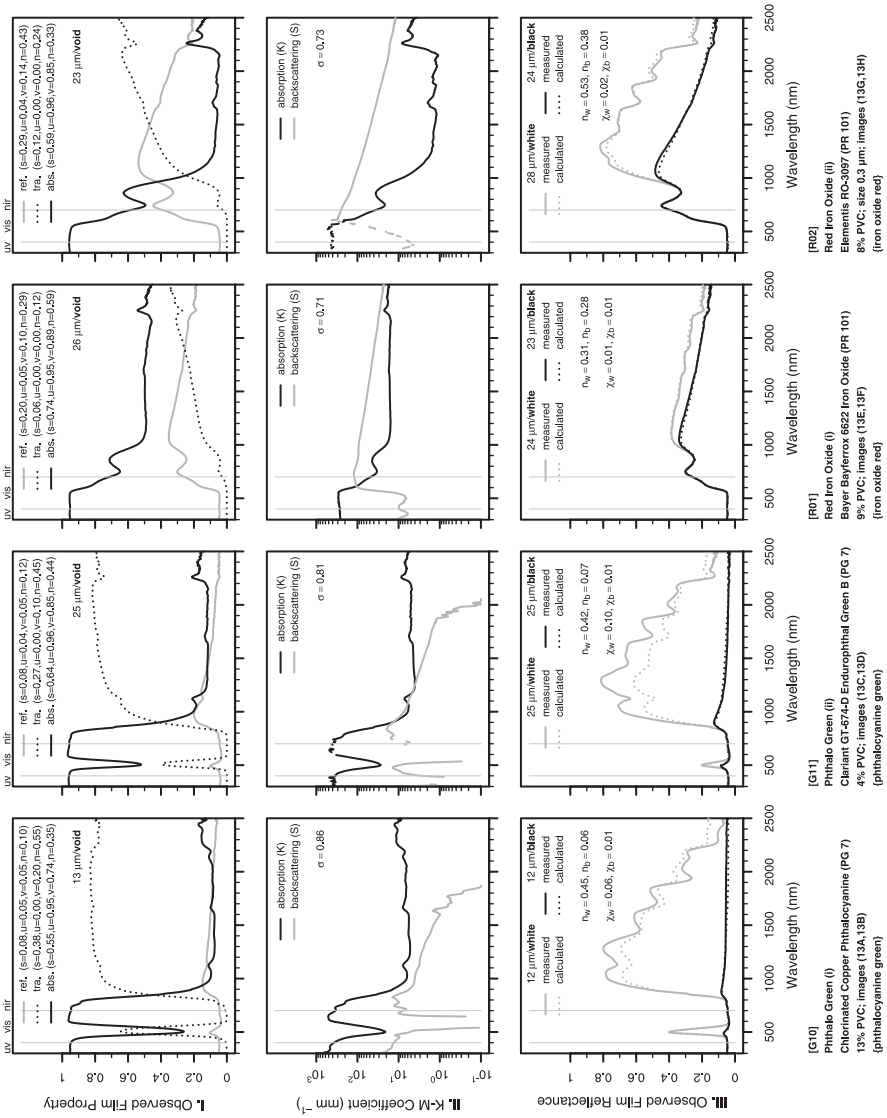

Fig. 1. (xiii/xxii)

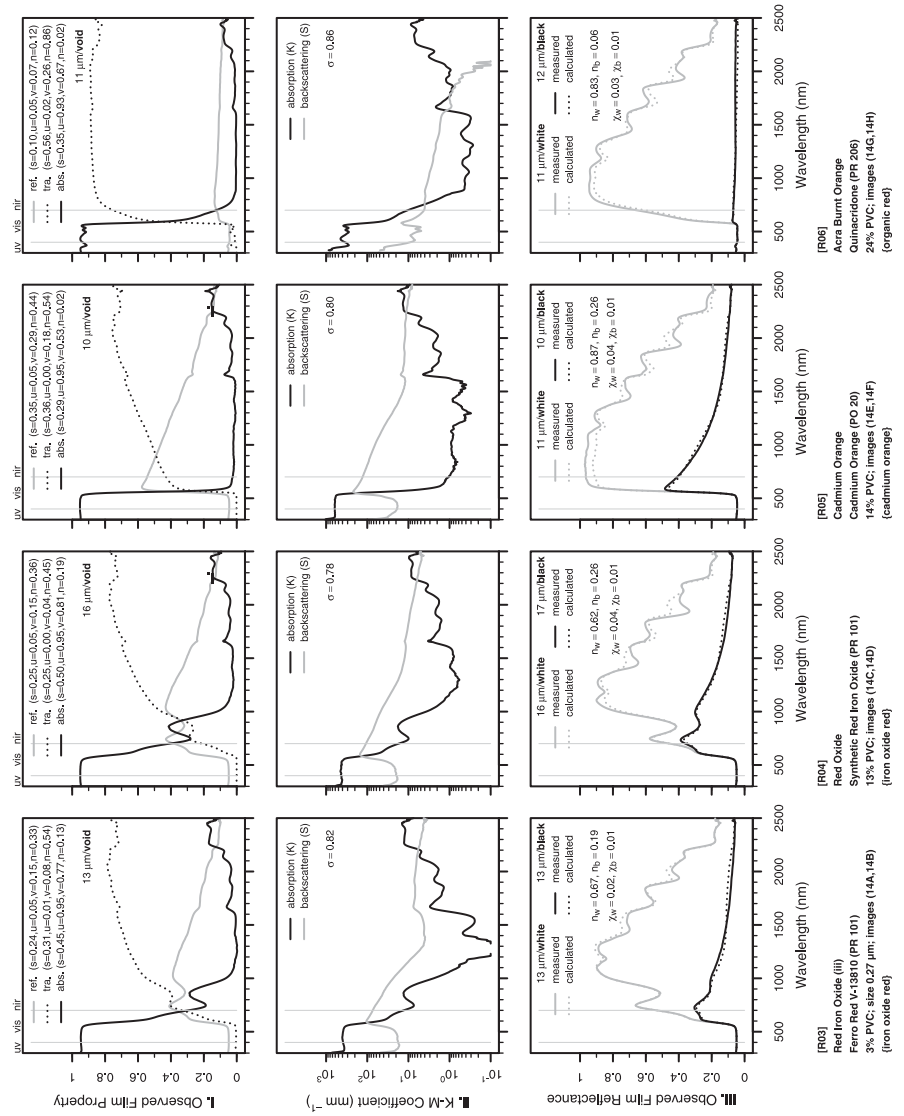

[R03]
Red Iron Oxide (iii)
Ferro Red V-13810 (PR 101)
3% PVC; size 0.27 µm; images (14A,14B)
(iron oxide red)

[R04]
Red Oxide
Synthetic Red Iron Oxide (PR 101)
13% PVC; images (14C;14D)
(iron oxide red)

[R05]
Cadmium Orange
Cadmium Orange (PO 20)
14% PVC; images (14E;14F)
(cadmium orange)

[R06]
Acra Burnt Orange
Quinacridone (PR 206)
24% PVC; images (14G;14H)
(organic red)

Fig. 1. (xiv/xxii)

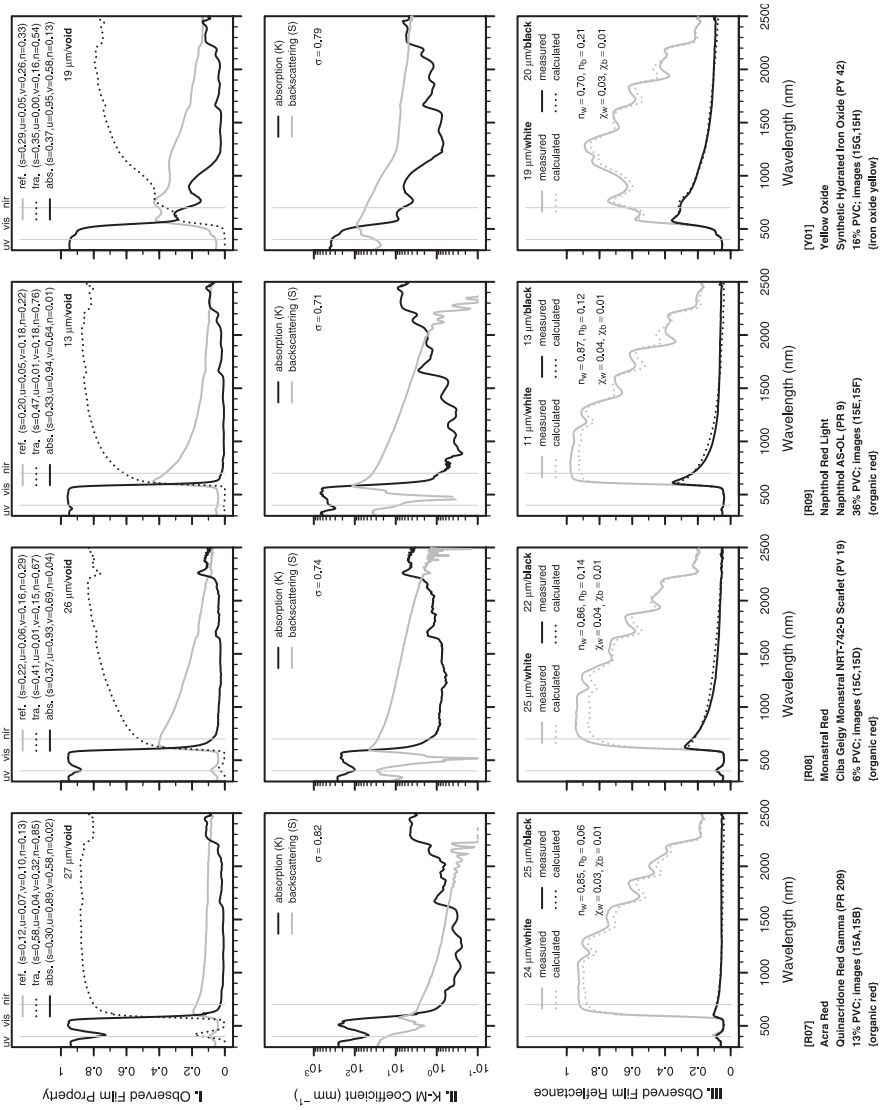
I. Observed Film Property
II. K-M Coefficient (mm⁻¹)
III. Observed Film Reflectance
uv vis nir
Wavelength (nm)
[R07]
Acra Red
Quinacridone Red Gamma (PR 209)
13% PVC; images (15A.15B)
(organic red)
[R08]
Monastral Red
Ciba Geigy Monastral NRT-742-D Scarlet (PV 19)
6% PVC; images (15C.15D)
(organic red)
[R09]
Naphthol Red Light
Naphthol AS-OL (PR 9)
36% PVC; images (15E.15F)
(organic red)
[Y01]
Yellow Oxide
Synthetic Hydrated Iron Oxide (PY 42)
16% PVC; images (15G.15H)
(iron oxide yellow)

Fig. 1. (xv/xxii)

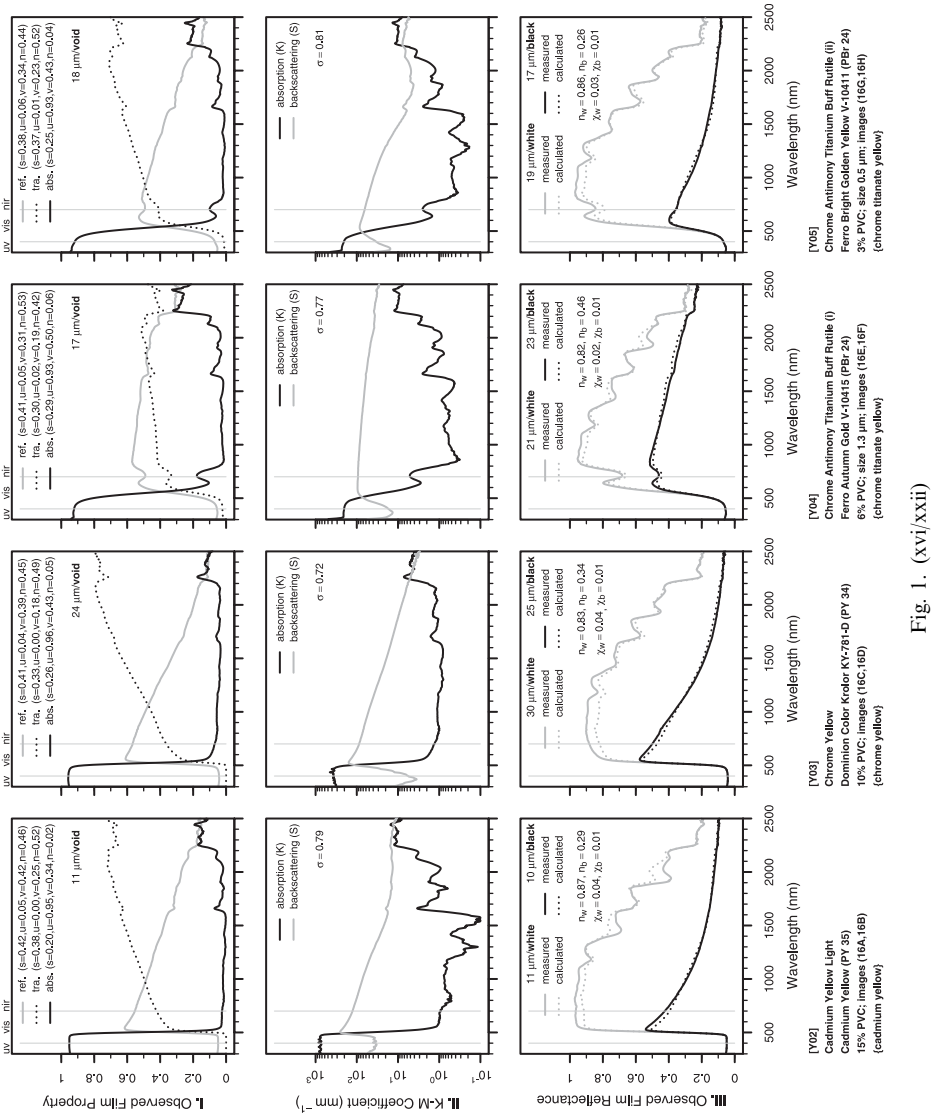

[Y02] **Cadmium Yellow Light**
Cadmium Yellow (PY 35)
15% PVC; images (16A,16B)
(cadmium yellow)

[Y03] **Chrome Yellow**
Dominion Color Krolor KY-781-D (PY 34)
10% PVC; images (16C,16D)
(chrome yellow)

[Y04] **Chrome Antimony Titanium Buff Rutile (I)**
Ferro Autumn Gold V-10415 (PBr 24)
6% PVC; size 1.3 μm; images (16E,16F)
(chrome titanate yellow)

[Y05] **Chrome Antimony Titanium Buff Rutile (II)**
Ferro Bright Golden Yellow V-10411 (PBr 24)
3% PVC; size 0.5 μm; images (16G,16H)
(chrome titanate yellow)

Fig. 1. (xvi/xxii)

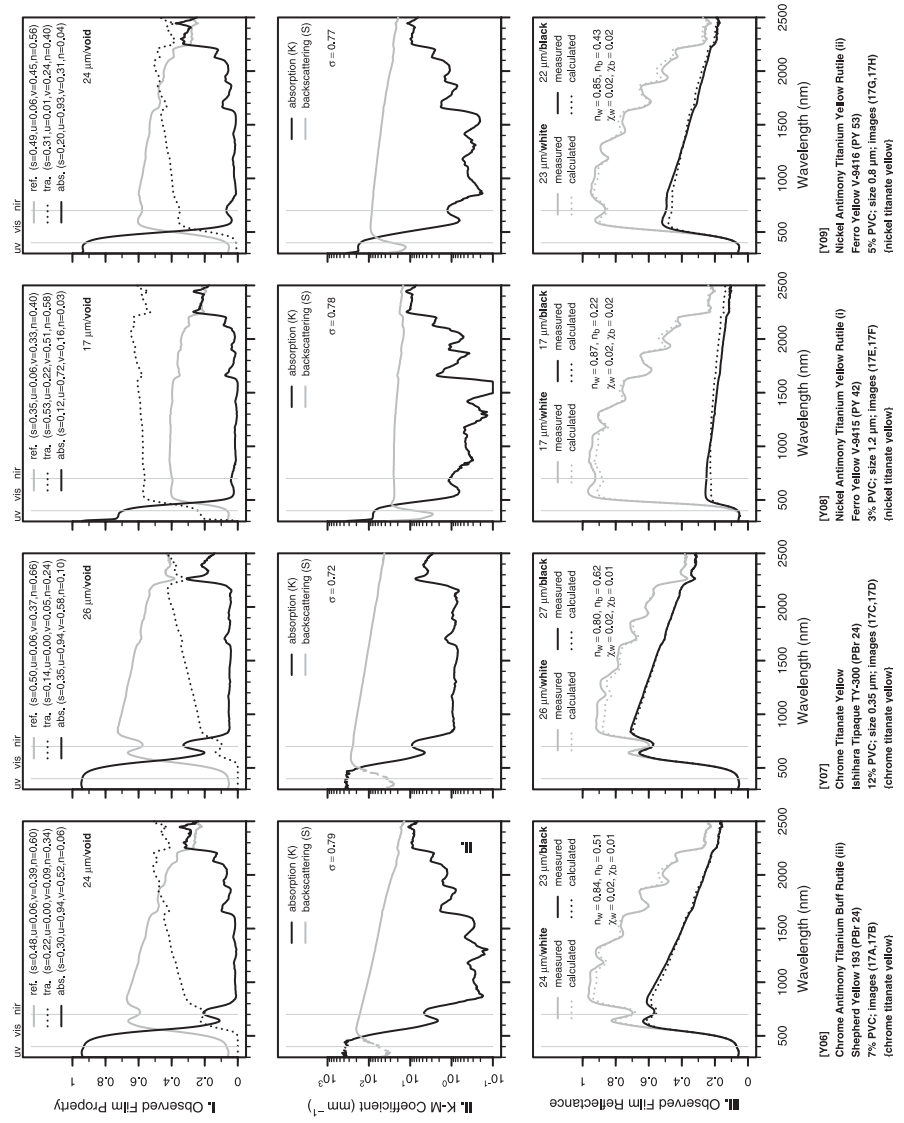

Fig. 1. (xvii/xxii)

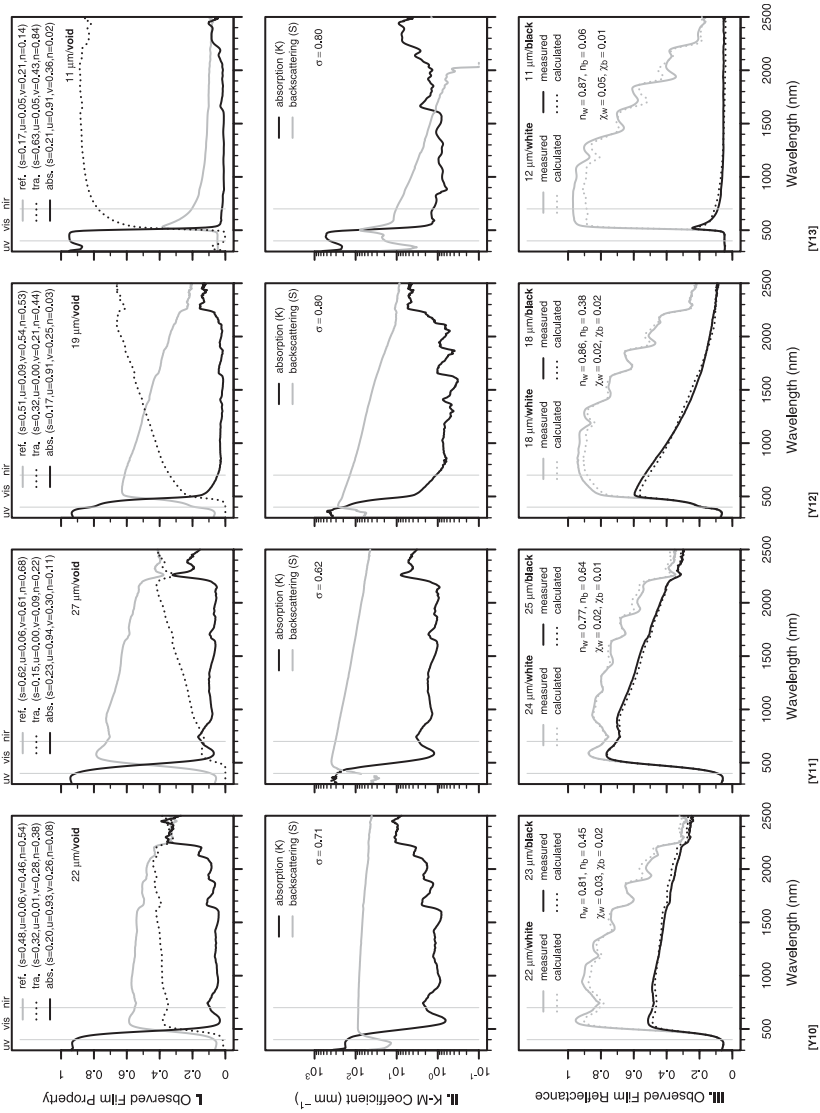

[Y10]
Nickel Antimony Titanium Yellow Rutile (iii)
Shepherd Yellow 195 (PY 53)
7% PVC; size 1.2 μm; images (18A,18B)
(nickel titanate yellow)

[Y11]
Nickel Titanate Yellow
Ishihara Tipaque TY-50 (PY 53)
15% PVC; size 0.4 μm; images (18C,18D)
(nickel titanate yellow)

[Y12]
Primer
Strontium Chromate Yellow + Titanium Dioxide
23% PVC; images (18E,18F)
(strontium chromate yellow + titanium dioxide)

[Y13]
Yellow Medium Azo
Arylide Yellow 5GX (PY 74 LF)
23% PVC; images (18G,18H)
(Hansa yellow)

Fig. 1. (xviii/xxii)

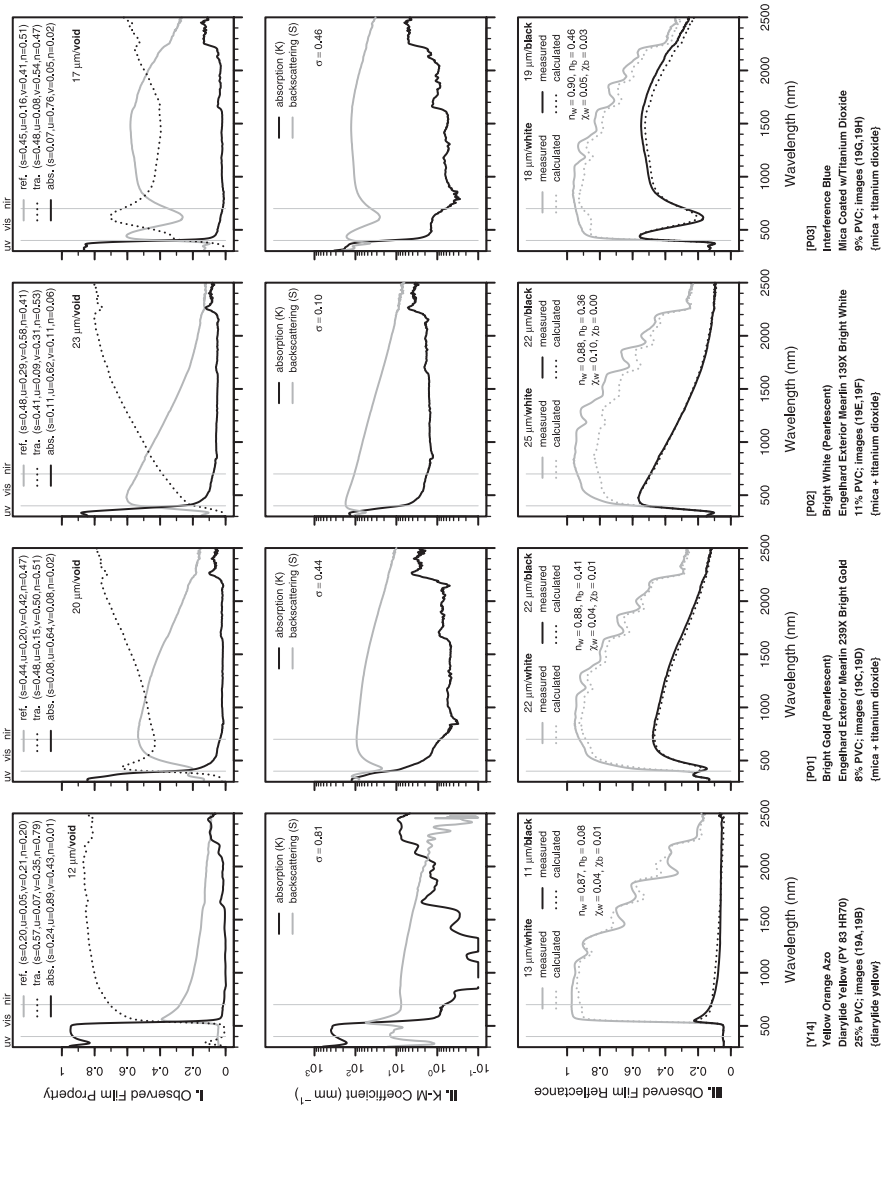

Fig. 1. (xix/xxii)

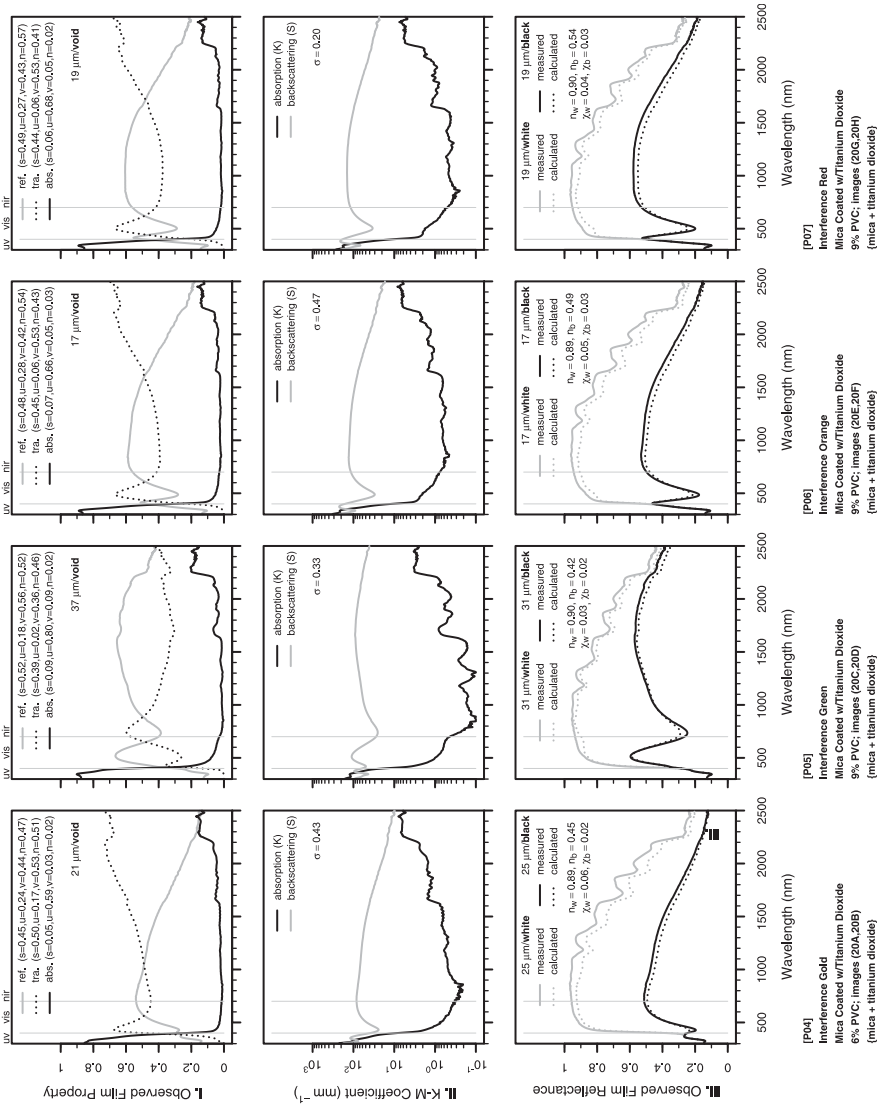
I. Observed Film Property
II. K-M Coefficient (mm⁻¹)
III. Observed Film Reflectance
uv vis nir
ref. (s=0.45,u=0.24,v=0.44,n=0.47)
trn. (s=0.50,u=0.17,v=0.53,n=0.51)
abs. (s=0.05,u=0.59,v=0.03,n=0.02)
21 µm/void
ref. (s=0.52,u=0.18,v=0.56,n=0.52)
trn. (s=0.39,u=0.02,v=0.36,n=0.46)
abs. (s=0.09,u=0.80,v=0.09,n=0.02)
37 µm/void
ref. (s=0.48,u=0.28,v=0.42,n=0.54)
trn. (s=0.45,u=0.06,v=0.53,n=0.40)
abs. (s=0.07,u=0.66,v=0.05,n=0.03)
17 µm/void
ref. (s=0.49,u=0.27,v=0.43,n=0.57)
trn. (s=0.44,u=0.06,v=0.53,n=0.41)
abs. (s=0.06,u=0.68,v=0.05,n=0.02)
19 µm/void
absorption (K)
backscattering (S)
σ = 0.43
σ = 0.33
σ = 0.47
σ = 0.20
25 µm/white
measured
calculated
25 µm/black
nW = 0.89, nb = 0.45
χW = 0.06, χb = 0.02
31 µm/white
31 µm/black
nW = 0.90, nb = 0.42
χW = 0.03, χb = 0.02
17 µm/white
17 µm/black
nW = 0.89, nb = 0.49
χW = 0.05, χb = 0.03
19 µm/white
19 µm/black
nW = 0.90, nb = 0.54
χW = 0.04, χb = 0.03
Wavelength (nm)
[P04]
Interference Gold
Mica Coated w/Titanium Dioxide
6% PVC; images (20A,20B)
(mica + titanium dioxide)
[P05]
Interference Green
Mica Coated w/Titanium Dioxide
9% PVC; images (20C,20D)
(mica + titanium dioxide)
[P06]
Interference Orange
Mica Coated w/Titanium Dioxide
9% PVC; images (20E,20F)
(mica + titanium dioxide)
[P07]
Interference Red
Mica Coated w/Titanium Dioxide
9% PVC; images (20G,20H)
(mica + titanium dioxide)

Fig. 1. (xx/xxii)

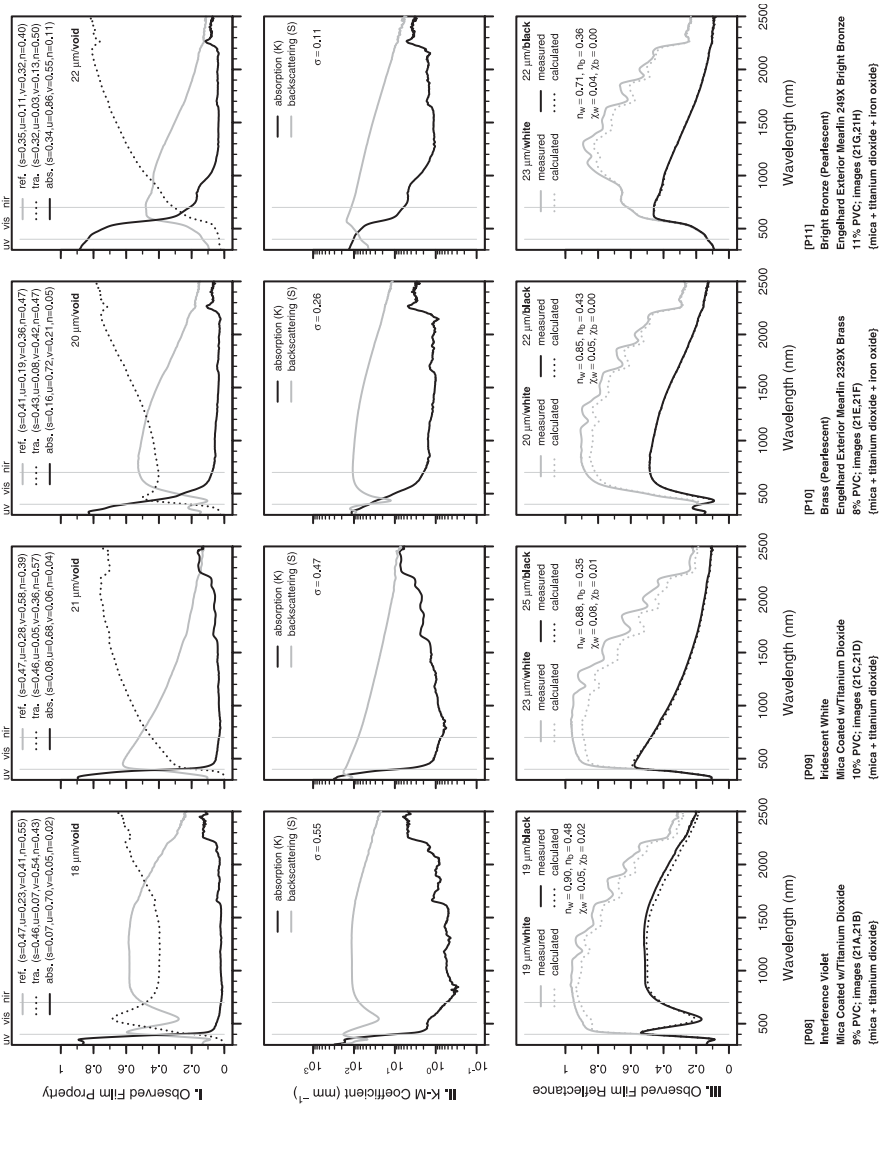

Fig. 1. (xxi/xxii)

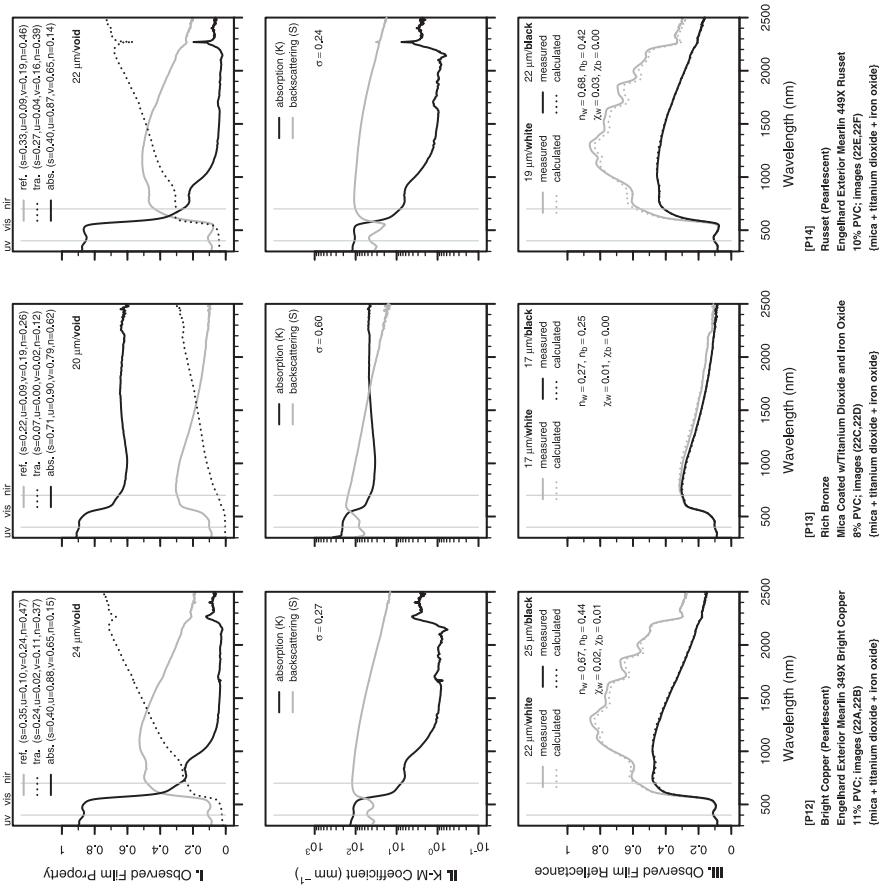

Fig. 1. (xxii/xxii)

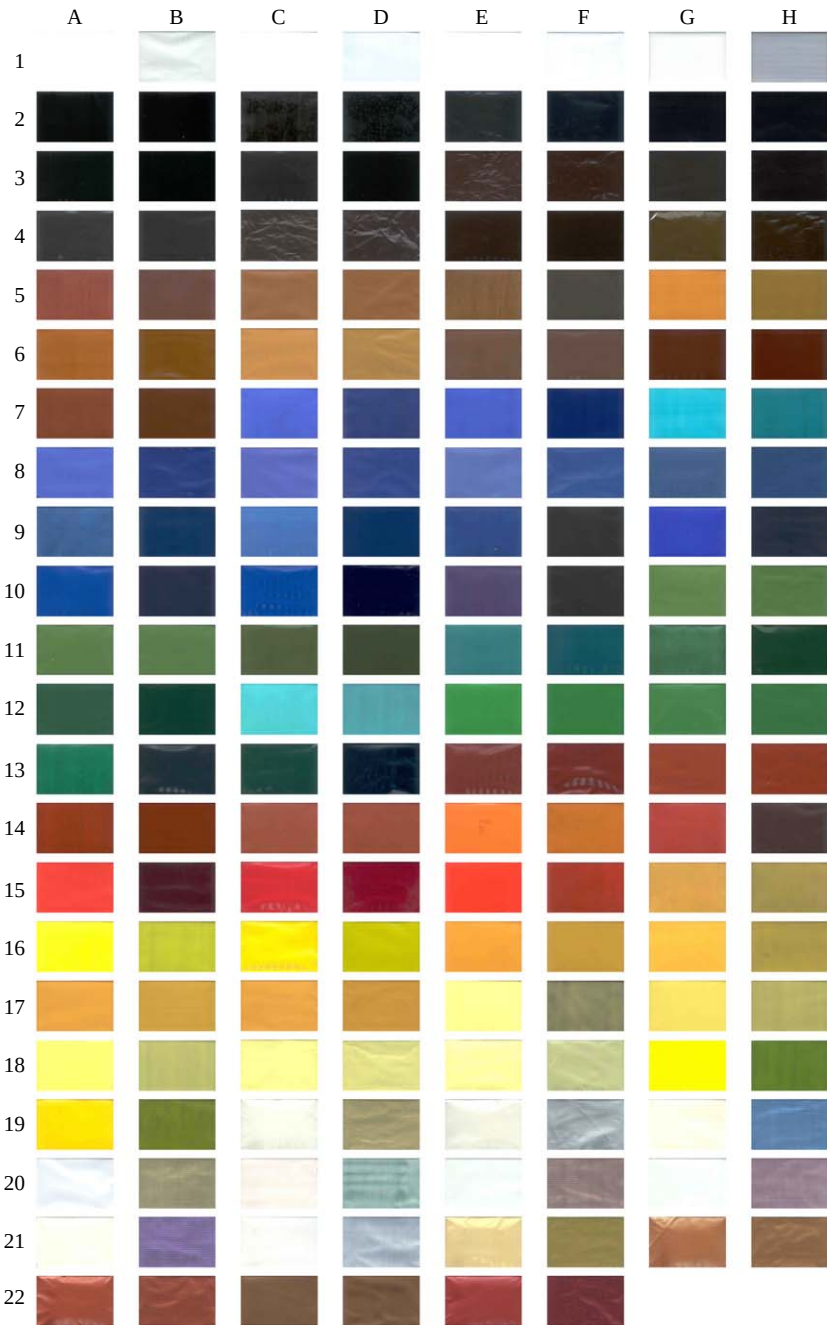

Fig. 2. Color images of paint films cited in Fig. 1. Shown for each paint film is its appearance over a white background, followed by its appearance over a black background.

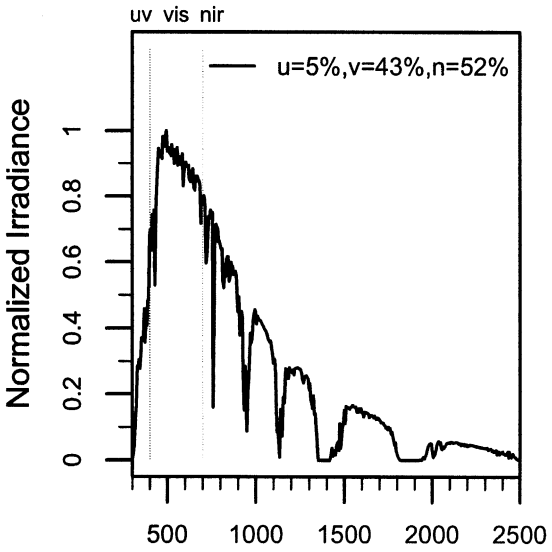

Fig. 3. Air mass 1.5 hemispherical solar spectral irradiance typical of North American insolation (5% ultraviolet, 43% visible, 52% NIR) [27].

3.1. White

All four whites were titanium dioxide (TiO_2) rutile. Other white pigments (not characterized in this study) include zinc oxide, zinc sulfide, antimony oxide, zirconium oxide, zirconium silicate (zircon), and the anatase phase of TiO_2.

TiO_2 rutile is a strongly scattering, weakly absorbing, stable, inert, nontoxic, inexpensive, and hence extremely popular white pigment [2]. TiO_2 whites W01–W04 exhibit similar curves of strong backscattering and weak absorption in the visible and NIR, except for drops in backscattering around 1500–2000 nm seen for W03 and W04. These last two samples are undiluted and 12:1 diluted versions of the same artist color.

Of the available white pigments, the rutile phase of TiO_2 has the highest refractive index in the visible (about 2.7) and therefore has the strongest visible light scattering power at the optimum particle size of about 0.2 μm. Its angle-weighted scattering coefficient s is estimated from the Mie scattering theory to be about 12 μm^{-1} for the center of the visible spectrum at 550 nm, assuming 0.22 μm diameter particles suspended in a clear binder with refractive index 1.5 [8,9]. Based on the same method as [8], one of us [10, Fig. 1 and Eq. (1)] has obtained angle-weighted scattering coefficient $s \approx 10.4\,\mu m^{-1}$ at 550 nm, using slightly different values for the refractive index of TiO_2. Thus there is good general agreement among different authors on this basic result from the Mie theory.

The question arises, what is the relation between the Mie theory result for s and the Kubelka–Munk backscattering coefficient S? Palmer et al. [8] give an equation

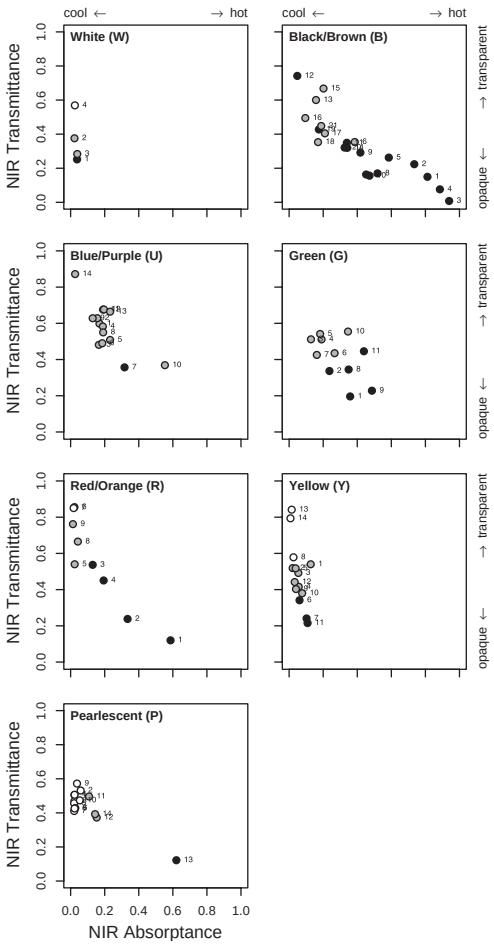

Fig. 4. NIR absorptances and transmittances of 87 pigmented films. A pigment with low NIR-absorptance is cool, but a cool pigment with high NIR transmittance requires an NIR-reflecting background. The color of each circle's interior indicates visible transmittance: black, less than 0.1; gray, between 0.1 and 0.3; white, over 0.3.

for the film reflectance of a non-absorbing layer as $R = (sf\delta)/(2 + sf\delta)$, where f is the pigment volume concentration and δ is the film thickness. The corresponding Kubelka–Munk equation is $R = S\delta/(1 + S\delta)$, which suggests that S should be identified with $\frac{1}{2}fs$. For clarification, we consider the special case of isotropic scattering, and examine the limit of weak scattering. Then s is just the total scattering cross section. In this limit the result of Palmer et al. is then exact if the incident radiation is a normally incident collimated beam; half the scattering is into the forward hemisphere, and half into the backward hemisphere. However, we are more interested in the reflectance for completely diffuse radiation, which is twice as large in this limit. Thus we identify S with fs. Superimposed on the backscattering curves

for samples W01–W04 are additional Mie-theory estimates for backscattering coefficient S as a function of wavelength, based on Ref. [10, Fig. 1 and Eq. (1)]. The measurements and theoretical estimates are in reasonable, but not precise, agreement. (If we had assumed $S = (1/2)fs$, agreement would be better in the visible region.)

At the longer infrared wavelengths, the measured backscattering declines more slowly than the theoretical values. (The theoretical values are approaching a Rayleigh regime in which S is proportional to the inverse fourth power of wavelength.) A plausible reason is the clumping of pigment particles. It is known that such clumping can raise the NIR reflectance [11].

Physically, the light scattering is due to the difference between the refractive index of the rutile particles (2.7) and that of the surrounding transparent medium (1.5). At high pigment volume concentrations, the presence of numerous nearby rutile particles raises the effective refractive index of the surrounding medium, and thereby reduces the efficiency of scattering. This fall in scattering efficiency is termed pigment crowding [12].

Rutile is a direct bandgap semiconductor and therefore has a very abrupt transition from low absorption to high absorption that occurs at 400 nm, the boundary between the visible and ultraviolet regions. For wavelengths below 400 nm (photon energies above 3.1 eV), the absorption is so strong that our data saturate, except in the case of the highly dilute (2% PVC) sample W04. At wavelengths above 400 nm, absorption is weak; most of the spectral features may be attributed to the binders used. One of the four white pigments (W01) does have a slightly less abrupt transition at 400 nm—there is an absorption "tail" near the band edge. This type of behavior is likely due to impurities in the TiO_2.

The sharp rise in absorptance near 300 nm shown for some films such as W04 is an artifact due to the use of a polyester substrate.

3.2. Black/brown

3.2.1. Carbon black, other non-selective black

Carbon black, bone black (10% carbon black + 84% calcium phosphate), copper chromite black ($CuCr_2O_4$), and synthetic iron oxide black (Fe_3O_4 magnetite) (B01–B04) are weakly scattering pigments with strong absorption across the entire solar spectrum. Carbon black B01 is the most strongly absorbing, but all four are "hot" pigments.

Most non-selective blacks are metallic in nature, with free electrons permitting many different allowed electronic transitions and therefore broad absorption spectra. Carbon black is a semi-metal that has many free electrons, but not as many as present in highly conductive metals. Both the iron oxide (magnetite) and copper chromite blacks are (electrically conducting) metals.

3.2.2. Chromium iron oxide selective black

Chromium iron oxide selective blacks (B05–B11) are mixed metal oxides (chromium green–black hematite, chromium green–black hematite modified,

chromium iron oxide, or chromium iron nickel black spinel) formulated to have NIR reflectance significantly higher than carbon and other non-selective blacks. Some, such as chromium green–black hematite B06, appear more brown than black. While these pigments have good scattering in the NIR, with a backscattering coefficient at 1000 nm about half that of TiO_2 white, they are also quite absorbing ($K \approx 50\,mm^{-1}$) in the short NIR. These pigments are visibly hiding (opaque to visible radiation) and NIR transmitting, so use of a white background improves their NIR reflectances without significantly changing their appearances.

Pure chromium oxide green (Cr_2O_3; color index designation pigment green 17), has the hematite crystal structure and will be discussed further together with other green pigments. When some of the chromium atoms are replaced by iron, a dark brownish black with the same crystal structure is obtained—i.e., a traditional cool black pigment (e.g., B06–B11; B05 differs because it contains nickel and has a spinel structure). It is sometimes designated as Cr-Fe hematite [13] or chromium green–black hematite [14], and has been used to formulate infrared-reflective vinyl siding since about 1984 [15]. A number of modern recipes for modified versions of this basic cool black incorporate minor amounts of a variety of other metal oxides. One example is the use of a mixture of 93.5 g of chromium oxide, 0.94 g of iron oxide, 2.38 g of aluminum oxide, and 1.88 g of titanium oxide [16]. The mixture is calcined at about 1100 °C to form hematite-structure crystallites of the resulting mixed metal oxide.

3.2.3. *Organic selective black*

Perylene black (B12) is a weakly scattering, dyelike organic pigment that absorbs strongly in the visible and very weakly in the NIR. Its sharp absorption decrease at 700 nm gives this pigment a jet black appearance and an exceptionally high NIR reflectance (0.85) when applied over white. Perylene pigments exhibit excellent lightfastness and weatherfastness, but their basic compound (dianhydride of tetracarboxylic acid) may or may not be fast to alkali; Refs. [4] and [2] disagree on the latter point.

3.2.4. *Iron oxide brown*

Iron oxide browns (B13–B15) such as burnt sienna, raw sienna, and raw umber exhibit strong absorption in part of the visible spectrum and low absorption in the NIR. These can provide effective cool brown coatings if given a white background, though this will make some (e.g., burnt sienna B13) appear reddish. These browns are "natural" and can be expected to contain various impurities.

3.2.5. *Other brown*

Other browns characterized (B16–B21) include iron titanium (Fe–Ti) brown spinel, manganese antimony titanium buff rutile, and zinc iron chromite brown spinel. These mixed-metal oxides have strong absorption in most or all of the visible spectrum, plus weak absorption and modest scattering in the NIR. A white undercoating improves the NIR reflectance of all browns, but brings out red tones in Fe–Ti brown spinels B16 and B17.

The cool Fe–Ti browns (B16–B18) have spinel crystal structure and basic formula Fe_2TiO_4 [14,17]. Despite the presence of Fe^{2+} ions, the infrared absorption of this material is weak. (In many materials, the Fe^{2+} ion is associated with infrared absorption [18,19]; see also our data for Fe_3O_4. The current data demonstrate that the absorption spectra also depend on the environment of the Fe^{2+} ion.) We also note that while B17 and B18 are nominally the same material, the details of the absorption are different.

We have not yet characterized a synthetic iron oxide hydrate brown (e.g., FeOOH).

3.3. Blue/purple

3.3.1. Cobalt aluminate blue, cobalt chromite blue

Cobalt aluminate blue (nominally $CoAl_2O_4$, but usually deficient in Co [3]; U01–U05) and cobalt chromite blue ($Co[Al,Cr]_2O_4$; U06–U09) derive their appearances from modest scattering ($S \approx 30\,mm^{-1}$) in the blue (400–500 nm) and strong absorption ($K \approx 150\,mm^{-1}$) in the rest of the visible spectrum. They have very low absorption in the short NIR, but exhibit an undesirable absorption band in the 1200–1600 nm range, which contains 17% of the NIR energy. A white background dramatically increases NIR reflectance but makes some (e.g., cobalt aluminum blue spinel U02) much lighter in color.

3.3.2. Iron blue

Iron (a.k.a. Prussian or Milori) blue (U10) is a weakly scattering pigment with strong absorption in the visible and short NIR, and weak absorption at longer wavelengths. It appears black and has little NIR reflectance over a black background, but looks blue and has a modest NIR reflectance (0.25) over a white background. Iron blue is not ideal for cool coating formulation.

3.3.3. Ultramarine blue

Ultramarine blue (U11), a complex silicate of sodium and aluminum with sulfur, is a weakly scattering pigment with some absorption in the short NIR. If sparingly used, it can impart absorption in the yellow spectral region without introducing a great deal of NIR absorption. This is a durable inorganic pigment with some sensitivity to acid [2].

While most colored inorganic pigments contain a transition metal such as Fe, Cr, Ni, Mn, or Co, ultramarine blue is unusual. It is a mixed oxide of Na, Si, and Al, with a small amount of sulfur ($Na_{7.5}Si_6Al_6O_{24}S_{4.5}$). The metal oxide skeleton forms an open clathrate sodalite structure that stabilizes S_3^- ions in cages to form the chromophores [3, Section 3.5] [20]. Thus isolated S_3 molecules with an attached unpaired electron cause the light absorption in the 500–700 nm range, producing the blue color. The refractive index of ultramarine blue is not very different from the typical matrix value of 1.5 [3, Section 3.5], so the pigment causes little scattering.

3.3.4. Phthalocyanine blue

Copper phthalocyanine blue (U12–U13) is a weakly scattering, dyelike pigment with strong absorption in the 500–800 nm range and weak absorption in the rest of the visible and NIR. Phthalo blue appears black and has minimal NIR reflectance over a black background, but looks blue and achieves a high NIR reflectance (0.63) over a white background (U12). It is durable and lightfast, but as an organic pigment it is less chemically stable than (high temperature) calcined mixed metal oxides such as the cobalt aluminates and chromites. General information on the structure and properties of phthalocyanines is available in Ref. [21]. The refractive index varies with wavelength, and exceeds 2 in the short wavelength part of the infrared spectrum [22]. Therefore the weak scattering we observe in our samples indicates that the particle size is quite small. The pigment handbook indicates a typical particle diameter of 120 nm [2], which is consistent with our data.

3.3.5. Dioxazine purple

Dioxazine purple (U14) is an organic optically similar to phthalo blue, but even more absorbing in the visible and less absorbing in the NIR. It is nearly ideal for formulation of dark NIR-transparent layers, but is subject to the chemical stability considerations noted above for phthalo blue.

3.4. Green

3.4.1. Chromium oxide green, modified chromium oxide green

Chromium oxide green Cr_2O_3 (G01–G02) exhibits strong scattering alternating with strong absorption across the visible spectrum, and strong scattering and mild absorption in the NIR. Since the pigment is almost opaque in the visible, a thin layer of chromium oxide green over a white background yields a medium-green coating with good NIR reflectance (0.57 for 13-μm thick film G02). The modified chromium oxide green (G03) is mostly chromium oxide, with small amounts of iron oxide, titanium dioxide, and aluminum oxide [16]. A layer of the modified chromium oxide green over a white background produces a medium green with excellent NIR reflectance (0.71).

Cr_2O_3 green is often mentioned as an infrared-reflective pigment that is useful for simulating the high infrared reflectance of plant leaves. Indeed, a high NIR reflectance is observed. However, our data for sample films G01 and G02 do show that there is a broadband absorption of about $10\,mm^{-1}$ in the near-infrared. While our measurements of absorptance coefficient are not precise for low absorptances, this value is clearly distinct from zero. Pure Cr_2O_3, fired in air, tends to become slightly rich in oxygen, which results in p-type semiconducting behavior [23,24]. Thus it is possible that the broadband IR absorption of Cr_2O_3 is due to free carrier absorption by mobile holes. Ref. [23] also reports that doping with Al can reduce the p-type conductivity in Cr_2O_3, so it seems likely that doping with Al and/or certain other metals can also reduce the IR absorption.

The modified chromium oxide green G03 is similar to G01 and G02 Cr_2O_3. However its green reflectance peak at 550 nm is somewhat smaller and its infrared absorption is clearly much smaller than those of samples G01 and G02.

3.4.2. Cobalt chromite green

Cobalt chromite green (G04–G06) is similar to cobalt chromite blue, and is commonly used for military camouflage.

3.4.3. Cobalt titanate green

Cobalt titanate green (G07–G09) is similar to cobalt chromite green, but scatters more strongly across the entire solar spectrum and has a pronounced absorption trough around 500 nm. A white background makes cobalt teal G07 very NIR reflective (0.73) but also appear light blue (hence, the name teal). The other two cobalt titanate greens (G08, G09) have respectable NIR reflectances (0.47, 0.37) over white and appear medium green.

3.4.4. Phthalocyanine green

Phthalocyanine green (G10–G11) is similar to phthalocyanine blue, but absorbs more strongly in the short NIR. Hence, the NIR reflectance of a thin phthalo green film over white, while good, is only 70% of that achieved by a thin layer of phthalo blue over white (0.45 for G10 vs. 0.63 for U12). Note also that the error in predicted reflectance over white for G11 is large, as discussed in the companion article [1].

3.5. Red/orange

3.5.1. Iron oxide red

Iron oxide red (R01–R04) derives its appearance from weak scattering and very strong absorption in the 400–600 nm band. One of the iron oxide reds (R01) exhibits moderate absorption across the NIR that may be due to doping of the Fe_2O_3 hematite crystals with impurities or result from broadband absorbing impurity phases such as Fe_3O_4; it is not a cool pigment. However, the remaining three iron oxide reds weakly absorb in the NIR and present both a dark red appearance and good NIR reflectance (0.53–0.67) over a white background. R02 also has a respectable NIR reflectance (0.38) over a black background, and has backscattering S comparable with TiO_2 white in the NIR.

3.5.2. Cadmium orange

Cadmium orange (R05) has weak scattering and very strong absorption in the 400–600 nm band, followed by strong scattering and virtually no absorption at longer wavelengths. Applied over a white background, it appears bright orange and has very high NIR reflectance (0.87)—essentially the same as that of the white background. Cadmium orange (and cadmium yellow, below) are Cd(S,Se) direct bandgap semiconductors. They exhibit sharp transitions between absorbing and non-absorbing regions, and have high refractive indices (e.g., 2.5 for CdS) that lead to large scattering coefficients. However, sensitivity to acid and the toxicity of cadmium limit their applications.

3.5.3. Organic red

Organic red pigments (R06–R09) such as acra burnt orange, acra red, monastral red, and naphthol red light have weak scattering and strong (sometimes very strong) absorption up to 600 nm, followed by very weak absorption and moderate-to-weak scattering at longer wavelengths. As a result they yield a medium-red color and a very high NIR reflectance (0.83–0.87) when applied over a white background. Masstones of acra burnt orange, acra red, and naphthol red light are all lightfast; their tints are slightly less so [2].

3.6. Yellow

3.6.1. Iron oxide yellow

Iron oxide yellow FeOOH (Y01) is a brownish yellow similar to iron oxide red. It appears tan and has a high NIR reflectance (0.70) when applied over a white background.

3.6.2. Cadmium yellow

Cadmium yellow (Y02) is similar to cadmium orange. It appears bright yellow and has very high NIR reflectance (0.87) over white.

3.6.3. Chrome yellow

Chrome yellow $PbCrO_4$ (Y03) is optically similar to cadmium yellow but exhibits a more gradual reduction in absorptance. It appears bright yellow and achieves a high NIR reflectance (0.83) over white. In some applications, the presence of lead and/or the Cr(VI) ion impose limitations.

3.6.4. Chrome titanate yellow

Chrome titanate yellow (Y04–Y07) is similar to chrome yellow, but scatters more strongly in the NIR. Its scattering coefficient can exceed 100 mm^{-1} in the short NIR, suggesting that this pigment might be used in place of titanium dioxide white to provide a background of high NIR reflectance. Over a black background, chrome titanate yellow appears brown to green and has moderate to high NIR reflectance (0.26–0.62). Over white, it appears orange to yellow and has very high NIR reflectance (0.80–0.86). Y07 over black produces a medium brown with NIR reflectance 0.62.

The curves for Y04 and Y05 illustrate how the backscattering coefficient S varies with particle size (manufacturer data). For smaller particles, the decrease in S with increasing wavelength is more dramatic.

3.6.5. Nickel titanate yellow

Nickel titanate yellow (Y08–Y11) is similar to chrome titanate yellow. Note that these compounds usually also contain antimony in their formulation. Over white, it appears a muted yellow and yields very high NIR reflectance (0.77–0.87); over black, it appears yellowish green and achieves moderate to high NIR reflectance (0.22–0.64). Y11 is a particularly good candidate to use over black.

3.6.6. Strontium chromate yellow + titanium dioxide

Strontium chromate yellow (solids mass fraction 11%) mixed with titanium dioxide (solids mass fraction 9%) in a paint primer (Y12) appears greenish brown over a black background, and pale yellow over a white background. It has very low absorption (order $1\,mm^{-1}$) and strong scattering (order $100\,mm^{-1}$) at 1000 nm, giving it a good NIR reflectance over black (0.38) and a very high NIR reflectance over white (0.86).

3.6.7. Hansa yellow, diarylide yellow

Hansa yellow (Y13) and diarylide yellow (Y14) are weakly scattering, dyelike organic pigments with high absorption below 500 nm and very weak absorption elsewhere. Over white, they typically (though not always) appear bright yellow and orange–yellow, respectively, and yield very high NIR reflectance (0.87).

3.7. Pearlescents

3.7.1. Mica + titanium dioxide

Mica flakes coated with titanium dioxide (P01–P09) exhibit strong scattering and weak absorption, producing their colors (e.g., gold, blue, green, orange, red, violet, or bright white) via thin-film interference. Some have scattering coefficients exceeding $100\,mm^{-1}$ in the near infrared. Over white, they appear white and have very high NIR reflectance (0.88–0.90); over black, they typically (though not always) achieve their named colors and have high NIR reflectance (0.35–0.54). The NIR reflectance of a pearlescent film over an opaque white background can exceed that of the background.

3.7.2. Mica + titanium dioxide + iron oxide

Mica flakes coated with titanium dioxide and iron oxide (P10–P14) are in most cases similar to mica flakes coated with only titanium dioxide, but are more absorbing, less scattering, darker, and somewhat less reflecting in the NIR. The exception is rich bronze P13, which has very high absorption and would not make a suitable cool pigment.

3.8. Aluminum + iron oxide + silicon oxide

While not characterized in the current study, the solar spectral reflectances of single-layer (iron oxide Fe_2O_3) or double layer (Fe_2O_3 on silicon dioxide SiO_2) interference coatings on aluminum flakes are presented in Refs. [25,26].

3.9. Cool and hot pigments

A simple way to evaluate the utility of a pigmented coating for "cool" applications is to consider its NIR absorptance and NIR transmittance. If the NIR absorptance is low, the pigment is cool. However, a cool pigment that has high NIR transmittance will require an NIR-reflective background (typically white or metallic) to produce an

NIR-reflecting coating. Charts of the NIR absorptance and transmittance of the members of each color family are shown in Fig. 4. An ideal cool pigment would appear near the lower left corner of the chart, indicating that it is weakly absorbing, weakly transmitting, and thus strongly reflecting in the NIR. Pigments appearing higher on the left side of the chart will form a cool coating if given an NIR-reflective background. Use of pigments appearing toward the right side of the chart (i.e., those with strong NIR absorption) should be avoided in cool applications. It should be noted that these charts do not provide perfect comparisons of "cool" performance because they show the NIR properties of films of varying thickness (10–37 μm) and visible hiding (visible transmittance 0–0.43 for non-pearlescents, and 0.02–0.54 for the pearlescents). Black-filled circles indicate visible transmittance less than 0.1; gray-filled circles, between 0.1 and 0.3; and white-filled circles, above 0.3.

There are cool films in the white, yellow, brown/black, red/orange, blue/purple, and pearlescent families with NIR absorptance less than 0.1. These films have moderate to high NIR transmittances (0.25–0.85), indicating than they would require an NIR-reflective background to perform well. There are also other slightly less cool black/brown, blue/purple, green, red/orange, yellow and pearlescent films with NIR absorptance less than 0.2. These have somewhat lower NIR transmittances (0.20–0.70), but are still far from NIR-opaque. A handful of pearlescent, blue/purple and red/orange films, along with half a dozen brown/black films, have NIR absorptances exceeding 0.5 and may be considered warm. A few nonselective blacks with NIR absorptance approaching unity may be considered hot.

Other useful metrics for "coolness" are NIR reflectances over white and black backgrounds (Table 1). Over a white background, the coolest pigments—i.e., those with NIR reflectances of at least 0.7—include members of the pearlescent, white, yellow, black/brown, red/orange, and blue/purple color families: mica coated w/ titanium dioxide (0.88–0.90), titanium dioxide white (0.87–0.88), cadmium yellow (0.87), cadmium orange (0.87), Hansa yellow (0.87), diarylide yellow (0.87), organic selective black (0.85), organic red (0.83–0.87), dioxazine purple (0.82), chrome titanate yellow (0.80–0.86), nickel titanate yellow (0.77–0.87), modified chromium oxide green (0.71), and iron oxide yellow (0.70). Other pigments with NIR reflectances of at least 0.5 include members of the blue/purple, black/brown, and green color families: cobalt aluminum blue (0.62–0.70), cobalt chromite blue (0.55–0.70), phthalo blue (0.55–0.63), cobalt chromite green (0.58–0.64), ultramarine blue (0.52), chromium oxide green (0.50–0.57), and other brown (0.50–0.74). Over a black background, the coolest pigments—in this case, those with NIR reflectances of at least 0.3—include members of the white, yellow, black/brown, red/orange, pearlescent, and green color families: titanium dioxide white (0.24–0.65), nickel titanate yellow (0.22–0.64), chrome titanate yellow (0.26–0.62), mica coated w/ titanium dioxide (0.35–0.54), mica + titanium dioxide + iron oxide (0.25–0.44), chromium oxide green (0.33–0.40), other brown (0.22–0.40), strontium chromate yellow + titanium dioxide (0.38), iron oxide red (0.19–0.38), chromium iron oxide selective black (0.11–0.35), and cobalt titanate green (0.21–0.30).

4. Conclusions

Our characterizations of the solar spectral optical properties of 87 predominately single-pigment paint films with thicknesses ranging from 10 to 37 μm have identified cool pigments in the white, yellow, brown/black, red/orange, blue/purple, and pearlescent color groupings with NIR absorptances less than 0.1, as well as other pigments in the black/brown, blue/purple, green, red/orange, yellow and pearlescent groupings with NIR absorptances less than 0.2. Most are NIR transmitting and require an NIR-reflecting background to form a cool coating. Over an opaque white background, some pigments in the pearlescent, white, yellow, black/brown, red/orange, green, and blue/purple families offer NIR reflectances of at least 0.7, while other pigments in the blue/purple, black/brown, and green color families have NIR reflectances of at least 0.5. A few members of the white, yellow, black/brown, red/orange, pearlescent, and green color families have NIR scattering sufficiently strong to yield NIR reflectances of at least 0.3 (and up to 0.64) over a black background.

Use of pigments with NIR absorptances approaching unity (e.g., nonselective blacks) should be minimized in cool coatings, as might be the use of certain pearlescent, blue/purple, red/orange, and brown/black pigments with NIR absorptances exceeding 0.5.

Acknowledgements

This work was supported by the California Energy Commission (CEC) through its Public Interest Energy Research Program (PIER), by the Laboratory Directed Research and Development (LDRD) program at Lawrence Berkeley National Laboratory (LBNL), and by the Assistant Secretary for Renewable Energy under Contract No. DE-AC03-76SF00098. The authors wish to thank CEC Commissioner Arthur Rosenfeld and PIER program managers Nancy Jenkins and Chris Scruton for their support and advice. Special thanks go also to Mark Levine, director of the Environmental Energy Technologies Division at LBNL, and Stephen Wiel, head of the Energy Analysis Department at LBNL, for their encouragement and support in the initiation of this project. We also wish to thank the following people for their assistance: Kevin Stone and Melvin Pomerantz, LBNL; Michelle Vondran, John Buchko, and Robert Scichili, BASF Corporation; Richard Abrams, Robert Blonski, Ivan Joyce, Ken Loye, and Ray Wing, Ferro Corporation; Tom Steger and Jeffrey Nixon, Shepherd Color Company; and Robert Anderson, Liquitex Artist Materials.

References

[1] R. Levinson, P. Berdahl, H. Akbari, Solar spectral optical properties of pigments – Part I: model for deriving scattering and absorption coefficients from transmittance and reflectance measurements, Sol. Energy Mater. Sol. Cells 89 (4) (2005) 319–349, this issue; doi:10.1016/j.solmat.2004.11.012.

[2] P.A. Lewis, Pigment Handbook, vol. I, Wiley, New York, 1988.

[3] G. Buxbaum, Industrial Inorganic Pigments, second ed., Wiley-VCH, 1998.

[4] W. Herbst, K. Hunger, Industrial Organic Pigments, VCH, 1993.
[5] Y.S. Touloukian, D.P. DeWitt, R.S. Hernicz, Thermal Radiative Properties: Coatings, Thermophysical Properties of Matter, vol. 9, IFI/Plenum, New York, 1972.
[6] R. Mayer, The Artist's Handbook of Materials and Techniques, fifth ed., Viking Penguin, 1991.
[7] Society of Dyers and Colourists and American Association of Textile Chemists and Colorists, Colour index international: fourth online edition, http://www.colour-index.org.
[8] B.R. Palmer, P. Stamatakis, C.G. Bohren, G.C. Salzman, A multiple-scattering model for opacifying particles in polymer films, J. Coat. Technol. 61 (779) (1989) 41–47.
[9] E.S. Thiele, R.H. French, Computation of light scattering by anisotropic spheres of rutile titania, Adv. Mater. 10 (15) (1998) 1271–1276.
[10] P. Berdahl, Pigments to reflect the infrared radiation from fire, J. Heat Transfer 117 (1995) 355–358.
[11] D.J. Rutherford, L.A. Simpson, Use of a flocculation gradient monitor for quantifying titanium dioxide pigment dispersion in dry and wet paint films, J. Coat. Technol. 57 (724) (1985) 75–84.
[12] R.R. Blakey, J.E. Hall, Pigment Handbook, Titanium Dioxide, vol. I, Wiley, New York, 1988, pp. 1–42 (Chapter A).
[13] D.R. Swiler, Manganese vanadium oxide pigments, US Patent 6,485,557 B1, November 26, 2002.
[14] Dry Color Manufacturer's Association (DCMA), Classification and chemical description of the complex inorganic color pigments, Dry Color Manufacturer's Association, Alexandria, VA 22320, 1991.
[15] E.B. Rabinovitch, J.W. Summers, Infrared reflecting vinyl polymer compositions, US Patent 4,424,292, 1984.
[16] T.R. Sliwinski, R.A. Pipoly, R.P. Blonski, Infrared reflective color pigment, US Patent 6,174,360 B1, January 16, 2001.
[17] V.A.M. Brabers, The electrical conduction of titanomagnetites, Physica B 205 (1995) 143–152.
[18] L.B. Glebov, E.N. Boulos, Absorption of iron and water in the Na_2O–CaO–MgO–SiO_2 glasses, II. Selection of intrinsic, ferric, and ferrous spectra in the visible and UV regions, J. Non-Cryst. Solids 242 (1998) 49–62.
[19] R.N. Clark, Manual of Remote Sensing, Remote Sensing for the Earth Sciences, Spectroscopy of Rocks and Minerals, and Principles of Spectroscopy, vol. 3, Wiley, New York, 1999, pp. 3–58 (Chapter 1), http://speclab.cr.usgs.gov, Fig. 5.
[20] R.J.H. Clark, D.G. Cobbold, Characterization of sulfur radical anions in solutions of alkali polysulfides in dimethylformamide and hexamethylphosphoramide and in the solid state in ultramarine blue, green, and red, Inorg. Chem. 17 (1978) 3169–3174.
[21] N.B. Mckeown, Phthalocyanine Materials: Synthesis, Structure and Function, Cambridge University Press, Cambridge, UK, 1998.
[22] S. Wilbrandt, O. Stenzel, A. Stendal, U. Beckers, C. von Borczyskowski, The linear optical constants of thin phthalocyanine and fullerite films from the near infrared to the UV spectral regions: estimation of electronic oscillator strength values, J. Phys. B 29 (1996) 2589–2595.
[23] D. de Cogan, G.A. Lonergan, Electrical conduction in Fe_2O_3 and Cr_2O_3, Solid State Commun. 15 (1974) 1517–1519.
[24] H. Goodenough, Landolt–Bornstein Numerical Data and Functional Relationships in Science and Technology, New Series, Group III: Crystal and Solid-State Physics, vol. 17g (Semiconductors: Physics of Non-Tetrahedrally Bonded Binary Compounds III), Oxides of Chromium, Springer, Berlin, 1984, pp. 242–247, 548–551 (Chapter 9.15.2.5.1).
[25] G.B. Smith, A. Gentle, P. Swift, A. Earp, N. Mronga, Coloured paints based on coated flakes of metal as the pigment, for enhanced solar reflectance and cooler interiors: description and theory, Sol. Energy Mater. Sol. Cells 79 (2) (2003) 163–177.
[26] G.B. Smith, A. Gentle, P. Swift, A. Earp, N. Mronga, Coloured paints based on iron oxide and silicon oxide coated flakes of aluminium as the pigment, for energy efficient paint: optical and thermal experiments, Sol. Energy Mater. Sol. Cells 79 (2) (2003) 179–197.
[27] ASTM, ASTM G 173-03: standard tables for reference solar spectral irradiance at air mass 1.5: direct normal and hemispherical on 37° tilted surface, Technical Report, American Society for Testing and Materials, 2003.